Aalto University
School of electrical engineering

Feasibility of SU-8 photoresist derived pyrolytic carbon for neurotransmitter measurement in biosensing applications

Katariina Sovanto

Thesis submitted for examination for the degree of Master of Science in Technology
Espoo 03.08.2016

Thesis supervisor:
Prof. Tomi Laurila

Thesis advisor:
D.Sc. (Tech.) Emilia Peltola

AALTO YLIOPISTO
SÄHKÖTEKNIIKAN KORKEAKOULU

Diplomityön tiivistelmä

Tekijä: Katariina Sovanto

Työn nimi: SU-8 johdetun pyrolyyttisen hiilen soveltuvuus hermovälittäjäaineiden mittaamiseen biosensorisovelluksissa

Päivämäärä: 31.07.2016 Kieli: Englanti Sivumäärä: [8 + 86]

Sähkötekniikan ja automaation laitos
Professuuri: Mikrosysteemitekniikka Koodi: S-113

Valvoja: Prof. Tomi Laurila
Ohjaaja: TkT Emilia Peltola

Dopamiinin sähkökemiallisen havaitsemisen suurimpia haasteita ovat biologisten liuosten monimutkaisuus, sekä dopamiinin alhainen pitoisuus ja nopea poistuminen näistä liuoksista. Biologisissa liuoksissa on lukuisia dopamiinin sähkökemiallista havaitsemista haittaavia molekyylejä, joista haitallisin on askorbiinihappo. Askorbiinihapon konsentraatiot ovat in vivo huomattavasti dopamiinia korkeampia, ja niiden hapettumispiikit osuvat hiilimateriaaleilla tyypillisesti hyvin lähelle toisiaan. Materiaalin täytyy siis olla sekä selektiivinen että herkkä dopamiinia kohtaan.

Pyrolyyttiset hiilet ovat pyrolyysissä valmistettuja nanografiittisia hiilimateriaaleja. Tässä työssä arvioitiin fotoresisti SU-8:sta johdetun pyrolyyttisen hiilen soveltuvuutta dopamiinin mittaamiseen in vivo. Materiaalin havaittiin muodostavan hyvin tasaisia, nanokiteisiä, grafiittisia pintoja, joilla on hyvä sähkönjohtavuus. SU-8 -resististä johdetulla pyrolyyttisellä hiilellä havaittiin nopeat ja reversiibelit sähkökemialliset ulkokehäreaktiot, kun resisti on pyrolysoitu 800 – 900 °C:ssa. Materiaalilla pystyy havaitsemaan dopamiinia alhaisimmillaan ainakin 500 nM liuoksesta. Askorbiinihapon ja dopamiinin hapettumispiikkejä ei materiaalilla ainakaan vielä pystytty testatuilla konsentraatioilla erottelemaan, mutta anodisointi ja happiplasmakäsittely molemmat paransivat niiden erotettavuutta. Dopamiinin havaitseminen onnistuu happiplasmaamattomalla elektrodilla myös soluviljelymediasta. Happiplasmakäsittely saa kuitenkin materiaalin reagoimaan mediassa olevien elektroaktiivisten molekyylien kanssa, vaikeuttaen dopamiinin mittaamista.

Bioyhteensopivuudesta puhutaan yleensä kudoskohtaisesti, ja neurologisen implantin tulee olla yhteensopiva nimenomaan hermokudoksen kanssa. Anturisovellus vaatii erityisen hyvää bioyhteensopivuutta, sillä elektrodin pinta ei saa kapseloitua tai likaantua, ja siten eristyä aktiivisesta aivokudoksesta. Kaiken kaikkiaan elektrodimateriaalin pitäisi pystyä tukemaan hermosolujen kasvua, selviytymistä ja erilaistumista dopaminergisiksi neuroneiksi. SU-8:sta johdetulla pyrolyyttisellä hiilellä ei havaittu sytotoksista vaikutusta hermokantasolujen kasvuun. Mitattu viabiliteetti vastasi suunnilleen viabiliteettia tetraedrisellä amorfisella hiilellä. Happiplasmakäsitellyillä näytteillä viabiliteetti saadaan yli kaksinkertaistettua. Hiiren hermokantasolujen erilaistaminen neuroneiksi ei onnistunut materiaalin pinnalla happikäsittelyn, poly-L-lysiinipinnoituksen, bFGF-kasvutekijän tai TSA erilaistamistekijän avulla.

Avainsanat: Pyrolyyttinen hiili, sähkökemiallinen karakterisointi, bioyhteensopivuus, dopamiini, syklinen voltammetria, viabiliteetti, erilaistuminen

AALTO UNIVERSITY
SCHOOL OF ELECTRICAL ENGINEERING

Abstract of the master's thesis

Author: Katariina Sovanto

Title: Feasibility of SU-8 photoresist derived pyrolytic carbon for neurotransmitter measurement in biosensing applications

Date: 31.07.2016 Language: English Number of Pages: [8 + 86]

Department of Electrical Engineering and Automation
Professorship: Microsystems technology Code: S-113

Supervisor: Prof. Tomi Laurila
Advisor: D.Sc. (Tech.) Emilia Peltola

The biggest challenges in electrochemical detection of dopamine are the complexity of biological liquids, as well as the low and brief concentrations of dopamine in vivo. Within biological liquids there are multiple molecules which might interfere with dopamine detection. One of the major ones is ascorbic acid, which exists in the human brain in much higher concentrations than dopamine does. The oxidation peaks for the two materials tend to overlap on carbon materials. All in all, the electrode material needs to be both selective and sensitive towards dopamine.

The purpose of this work is to evaluate the feasibility of SU-8 photoresist derived pyrolytic carbon for detecting dopamine in vivo. The fabrication process was found to result in extremely smooth, nanographitic surfaces with excellent conductivity. The material was characterized electrochemically using cyclic voltammetry. Rapid outer sphere reactions were measured in a FcMeOH solution indicated fast electron transfer and near reversible reactions for films fabricated at 800 – 900 °C. 500 nM DA concentration was the lowest in which dopamine was clearly detected. Separation for the oxidation peaks of dopamine and ascorbic acid could not be achieved in realistic concentrations, but some improvement in the peak shapes was achieved both after anodization and after oxygen plasma treatment of the electrodes. Dopamine was also detected successfully in cell culture media with an electrode, which was not treated with oxygen plasma. Oxygen plasma treatment made the electrode surface sensitive towards electroactive reagents within the cell culture media.

Biocompatibility is considered separately for each tissue type. For neural sensing applications, extremely good biocompatibility with neural tissue is required. The electrode surface can not be allowed to be encapsulated or fouled, as that might lead to electrochemical insulation from the target tissue. The material should be able to support growth, proliferation and neuronal differentiation cells. No cytotoxic effects were discovered on the SU-8 derived pyrolytic carbon, when mouse neural stem cells were seeded. The viability detected was about equal to the cellular viability on tetrahedral amorphous carbon. Oxygen plasma treatment of the pyrolytic carbon surface significantly increased cell viability. Cellular differentiation to neurons could not be induced despite treatment with poly-L-lysine, oxygen plasma, growth factor and differentiation factor.

Keywords: Pyrolytic carbon, electrochemical characterization, biocompatibility, dopamine, cyclic voltammetry, viability, differentiation

Preface

I would like to thank my supervisor, professor Tomi Laurila and my advisor Emilia Peltola for granting me the opportunity to do my thesis on an extremely interesting topic and for providing me with invaluable insight during this thesis work. I would also like to thank Emilia for introducing me to the practical work with cells, for providing me with the AFM measurements of the material, as well as for her aid and excellent feedback at all steps of the way.

A special thanks goes to Joonas Heikkinen and Ville Jokinen for providing me with the samples used in this work and to Joonas for also doing the Raman spectroscopy measurements and fitting for the Raman curves.

I started this work knowing next to nothing about the practical work and it has certainly been a learning curve. Thanks are due to all the people who taught me all I needed to know to do the experimental work. Tommi Palomäki and Noora Isoaho taught me how to do cyclic voltammetry measurements and electrode fabrication and introduced me to the appropriate lab protocols. They also provided valuable insight on interpreting the voltammetric results, along with Niklas Wester, who also deserves to be mentioned here. Elsi Mynttinen helped me with many of the biochemical protocols and provided me with much appreciated peer support.

I could not have managed my day to day life without my amazing husband, who aided me with Matlab so I could get all my results in a presentable form, and suffered through my company when I was so engrossed in my work I could only communicate in one word sentences. I would also like to thank my family for helping me get here in the first place, always cheering me up and being there for me when I have most needed it, and Lumi for being the most amazing niece a girl could ask for.

Finally I want to thank my friends for all their love, support and distractions. Special gratitudes go to Mikael who always makes sure I have my feet on the ground and my head in the clouds, to Miikka who is a constant reminder of my love for all things science, and to Johanna, Riina, Marika, Elina, Ilkka and Lilli who all worked with their respective theses and studies, yet still took the time to occasionally take me on grand adventures all over the galaxy. To infinity and beyond!

Oulu, August 30th 2016

Katariina Sovanto

Table of Contents

Symbols and abbreviations

Symbols

ΔE_p	peak-to-peak potential difference
λ_l	laser wavelength
C_{dl}	electric double layer capacitance
E_l	laser energy
I_{bc}	background current
I_D	Raman D peak intensity
I_G	Raman G peak intensity
I_{po}	oxidation peak intensity
I_{pr}	reduction peak intensity
L_a	lateral crystallite size

Abbreviations

AA	ascorbic acid
AFM	atomic force microscopy
bFGF	fibroblast growth factor, basic
cAMP	cyclic adenosine monophosphate
CNT	carbon nanotube
CV	cyclic voltammetry
CVD	chemical vapour deposition
DA	dopamine
DAC	dopaminechrome
DAQ	dopaminequinone
DF	differentiation factor
DOS	density of states
DPV	differential pulse voltammetry
EELS	electron energy loss spectroscopy
EGF	epithelial growth factor

FGF	fibroblast growth factor
GC	glassy carbon
GF	growth factor
hNSC	human neural stem cells
LDAC	leucodopaminechrome
LSV	linear sweep voltammetry
MTT	thiazolyl blue tetrazolium
N2a	mouse neuroblastoma cell line
NeuroE	mouse neural stem cell line NE-GFP-4C
NF	neurotrophic factor
NGF	nerve growth factor
NSC	neural stem cell
PAH	polyaromatic hydrocarbon
PC12	rat adrenal gland pheochromocytoma cell line
PCR	polymerase chain reaction
PLL	poly-L-lysine
PyC	pyrolytic carbon
SEM	scanning electron microscopy
ta-C	tetrahedral amorphous carbon
TH	tyrosine hydroxylase
TSA	trichostatin-A
UA	uric acid
XPS	X-ray photoelectron spectroscopy
XRD	X-ray diffraction

1 Introduction

Since the early 90s, nanocarbon thin film materials have gained increasing attention due to their favourable electrochemical and biocompatibility properties for bioadaptive sensing applications. Electrochemically they possess large potential windows, high electrochemical stability and sensitivity to many organic molecules. Biologically they are as carbon-based materials considered to be ideal for implantation. Nanocarbon materials form a wide range of different material configurations and many of them have been studied for biosensing purposes. Pyrolytic Carbons (PyCs) have been considered especially interesting due to their known biocompatibility, and their electrochemical properties have been characterized in more detail during the past decade or so. [1-12]

Especially electrochemical in vivo sensing neurotransmitters such as glutamate, dopamine (DA) and serotonin has been gaining interest. An underlying motivation of these studies is the possibility to measure these compounds in vivo, using neural implants within the human brain. Many neural functions and diseases are linked to specific neurotransmitters and their concentration within the human brain. These include for example Parkinson's disease, in which dopaminergic neurons are dysfunctional or dying, resulting in a lack of DA or abnormally low DA levels within the human brain. Enabling their detection in vivo could aid in studying and treating neural irregularities. [5, 9, 10]

The main challenges of accurately detecting DA in vivo are its low concentrations within the human brain, as well as the large amount of interfering compounds, of which ascorbic acid (AA) is one of the major ones, as it tends to have an oxidation peak around the same potential as DA does. It is also present in the brain in much higher concentrations than DA is. Additionally the method used is required to be sufficiently rapid, as DA can only be detected outside the cells momentarily. [9, 10]

PyCs are a group nanographitic thin film materials, which can be fabricated in high temperatures from various precursors. There is a lot of variation in between different PyC films, as their properties depend strongly on their fabrication history [1, 2, 9, 13-16]. Fabricating PyC films from photoresists has gained interest, as it is extremely easy and photoresists are readily patternable, making them extremely versatile as a fabrication material [9, 11, 12, 17-20]. In Chapter 2, the general properties of these materials are described, some essential characterization methods are presented, and they are compared to other carbon nanomaterials.

General electrochemical properties and neurotransmitter electrochemical sensitivity of novel PyC films have been studied especially in recent years [1-9]. The characterizations made in these studies have been promising, and many methods have been suggested to further improve their behaviour. However, there is much variation between the materials, and the results achieved on one PyC may not carry on to another. Carbon electrochemistry will be discussed in more detail in Chapter 3, and the current status of PyC electrochemistry is evaluated.

PyCs are well known for their good hemocompatibility and thromboresistance. Additionally they exhibit good thermal and electrical conductivity, high durability and good chemical and wear resistance. Because of these qualities, they have for a long time been a common material choice for heart valves and other prostheses [1]. Their compatibility with neural tissue is known to a far less extent. Even though there are a few promising results on the neural compatibility of graphene and PyC [9-12], the number of these studies is still quite small. For sensing purposes, the compatibility needs to be extremely good. The formation of any scar tissue could result in insulation of the sensor from the target tissue, which might prevent the detection altogether. In Chapter 4, central issues with neural implant biocompatibility are defined and methods used to evaluate relevant biocompatibility properties of a material are described. The state of the art research on PyC compatibility with neural tissue is also reviewed.

The aim of this work is to characterize structural, electrochemical and neural compatibility properties of SU-8 photoresist derived PyC films, consider ways to improve these properties and asses the feasibility of this material as an in vivo neurotransmitter sensor. Similar findings done on other PyC materials are also presented to find context and gain perspective to the results obtained in the experimental section. The aim of the experimental section specifically is defined in Chapter 5. Materials and methods are described in Chapter 6. The results of structural, electrochemical and biocompatibility experimental set-ups will be presented and reviewed in Chapter 7, and finally conclusions and future perspectives are discussed in Chapter 8.

2 Pyrolytic carbon

PyCs are disordered nanocrystalline graphitic man made materials that are usually produced from a hydrocarbon precursor at high temperatures up to 2800 °C. In a process called pyrolysis, the hydrocarbon reorganizes into graphitic crystallites. The material belongs to a group of so called amorphous carbons, which is a family of carbon materials consisting of disordered sp^2 and sp^3 hybridized carbon atoms, and hydrogen and oxygen terminations. The hydrocarbon for PyC precursor might be deposited by chemical vapour deposition (CVD) from a gaseous source, or from a liquid source for example by spinning. This Chapter takes a look on the previous studies done on the structural properties, as well as fabrication of PyC materials. [1]

Commercial uses of PyC vary from pebble bed reactors, rocket nozzles and electronic thermal management to reinforcement coating of softer materials, and tissue replacement implants such as heart valves [1]. There has not, to the author's knowledge, ever been commercial in vivo applications, where PyC would have been as an electrochemical sensor, much less a neural implant. The electrochemical sensing properties of PyC have, however, been studied to some degree since 2002 [2-9]. These studies will be further discussed in Chapter 3.

PyC is commonly known as a material with good hemocompatibility. The interactions of of PyC with neural tissue, however, is not as well known. Some previous studies on the behaviour of neural cells on polymer derived PyCs has been made [9, 11, 12]. The specifics of the biocompatibility of PyC are further discussed in Chapter 4.

This chapter focuses on the fabrication and structural properties of PyC materials and comparing them to other carbon-based materials. Various fabrication methods and precursors will be reviewed and methods for characterizing carbon material surface properties will be presented.

2.1 Fabrication

PyC materials can be fabricated with various deposition methods from various precursors on various substrates. Common to all of the materials is the end result, which is the pyrolysed carbon layer. However, the structure and composition of these layers might differ a lot depending on how they have been fabricated.

The substrate is one important factor in PyC fabrication. Various substrates have been used, including flat silicon, structured or patterned silicon and graphite. Appropriate choice of substrate is dependent on the application and deposition method of the PyC. The number of possible substrates for PyC films is greatly limited by the high temperatures required for the pyrolysation process, which will be further discussed in Section 2.1.1.

Two deposition methods have been commonly used for PyC deposition. Firstly CVD deposition of PyC utilizes a gas phase precursor, and it can be used to create a conformal coating of PyC [13]. With this deposition method, porous and patterned substrates may be used and, due to conformal nature of CVD coatings, these features will prevail after coating [6, 14, 15]. The thickness of the PyC layer coated with CVD has a linear dependence on the deposition time [1].

A second way to create PyC layers is to coat the substrate with a liquid hydrocarbon precursor by spinning and subsequently pyrolysing the precursor [2]. This does not result in a conformal coating like CVD deposition does, but it is much faster and cheaper. Some precursors of this type are readily patterned even into complicated 3D structures [16, 17]. Such is the case with using the common photoresist SU-8 as the precursor. The use of SU-8 as a precursor for PyC film has been studied previously [9, 12, 17-19].

2.1.1 **Pyrolysation**

During pyrolysation, the hydrocarbon precursor is introduced to the substrate, usually in a controlled atmosphere. The hydrocarbons react chemically and are nucleated into carbon structures. Various reaction pathways that may lead to the resulting structures, and they are dependent on both the pyrolysation temperature, as well as the precursor. [1]

Typically both amorphous carbon and graphitic carbon, consisting of aromatic structures, are formed. Pyrolysation done at temperatures between 500°C and 1000°C tend to form more amorphous and disordered carbon, where higher temperatures and deposition time yield larger planes of the ordered graphitic structures. The graphitization process is facilitated with polymeric precursors, which already include aromatic structures or sp^2 hybridized electrons to begin with. Some examples of such precursors are SU-8 [20] in Figure 1 and polyacetylene [21] in Figure 2.

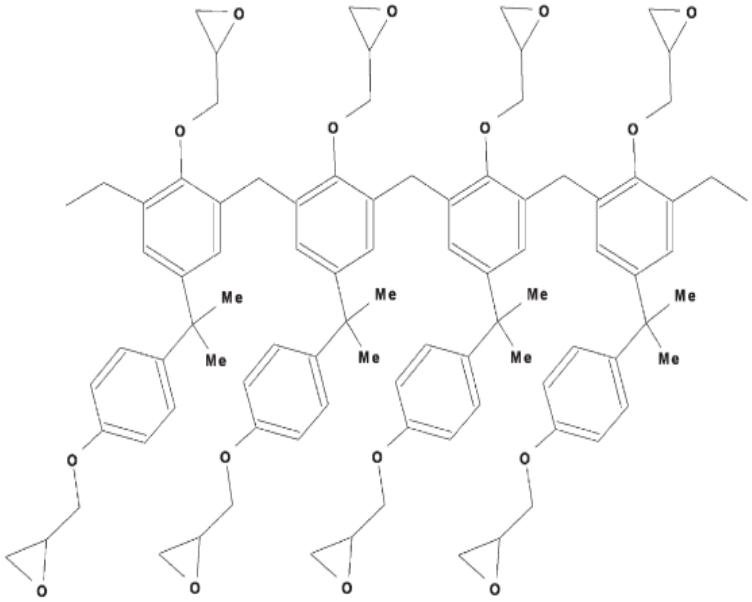

Figure 1. SU-8 photoresist molecular structure. [20]

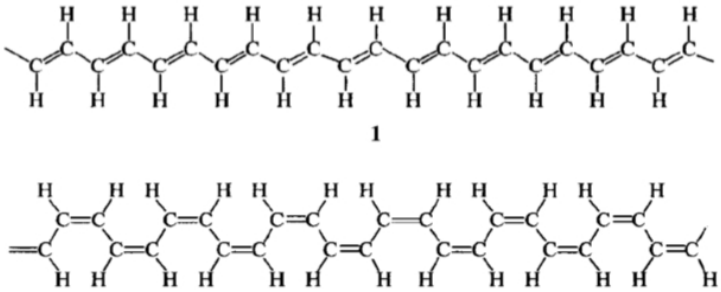

Figure 2. Cis- and trans- polyacetylene molecular structures. [21]

During the pyrolysation process, lighter elements will evaporate in higher amounts with increasing pyrolysation temperatures. For example Goto et al. [19] found that with the pyrolysation of polyacetylene above 800 °C less than 1 wt% of the film was hydrogen. High temperatures also show a decrease in yield. More on the results for different precursors will be discussed later in this chapter. The growth of the PyC film can be divided into the nucleation and growth mechanisms of the aromatic planes. The growth mechanism is based on the addition reactions of reactive gas phase intermediates at active sites, especially at graphene layer edges. The nucleation mechanism is in turn favoured when all active sites are occupied. In nucleation, large polycyclic aromatic hydrocarbons are formed in the gas phase and new graphene layers may be nucleated by the physisorption or condensation of these aromatic hydrocarbons on the surface. [20]

It is not the deposition mechanism, but rather the carbon formation mechanism which defines the structure of the resulting film. This includes both gas phase and surface reactions of the intermediate molecules. Small hydrocarbons will react to small aromatic hydrocarbons at temperatures below 1100 °C. The formation of Benzene is strongly accelerated with higher hydrocarbon partial pressure. After the initial formation of the aromatic groups, so called aromatic growth occurs. During the aromatic growth, smaller aromatic hydrocarbons link into large polyaromatic hydrocarbons (PAH). The PAHs increase in size with prolonged pyrolysation time and higher temperatures. Very large PAHs form π radicals. Nonplanarities in the graphitized PAH structures are typically caused by 5-membered and 7-membered rings that may also be formed during the pyrolysation process, especially in high temperatures. They also get formed in hydrogen lacking atmospheres. At low temperatures, low pressures, short residence times and high surface area/volume ratios, formation of aromatic hydrocarbons is limited and less ordered carbon is to be expected. [22]

The atmosphere during pyrolysation is controlled, as some gases such as oxygen tend to interfere with the reactions. Argon and nitrogen are two gases, typically used as inert gasses during the pyrolysation process. Special care needs to be taken with the temperature ramping rates before and after pyrolysation. This is because the coefficient of thermal expansion (CTE) mismatch between the surface and the PyC layer might result in the delamination of the pyrolysed layer. Too fast pyrolysation might result in a rough and irregular surface. [23]

2.1.2 **Precursors**

PyC precursors are all hydrocarbons and they can be divided roughly in two groups determined by the deposition methods they can be used with. Gaseous precursors such as acetylene, propane, polyimide and methane have all been used as PyC precursor in CVD. Liquid phase hydrocarbons like SU-8 on the other hand, can be deposited for example by spinning. While there is a wide range of precursors that have been used in PyC fabrication, only acetylene, methane, SPR 220.7 and SU-8 are presented here, as they have all been used to fabricate films for electrochemical or biocompatibility studies. The differences between these various precursors are presented in the Table 1, at the end of this Section.

CVD precursors

McEvoy et al. [1] used acetylene as a precursor for PyC deposition. They found the growth rate to be constant at temperatures below 1000 °C. However above 1000 °C, the products of acetylene decomposition would complicate film growth kinetics. Deposition rate was shown to increase linearly with deposition time on Si substrate between 850 °C and 1100 °C. The dependence of deposition rate to temperature was on the other hand exponential. This suggests that the deposition process is thermally activated. The activation energy was calculated to be 2.68 eV ± 0.15 eV which is a little higher than the enthalpy of acetylene formation, and around the same scale as the activation energies for other hydrocarbons of roughly the same size. Acetylene has also been used as a PyC precursor by Zhang et al. [13] who used it to coat alumina particles with fluidized bed CVD. They deposited acetylene/propylene mixture at temperatures between 1250 °C and 1450 °C. They also did additional pyrolysation treatments at 1800 °C and 2000 °C.

Methane (CH_4) has been used by Wu et al. [6] and Hadi et al. [3-5, 8] for PyC CVD in multiple studies. The pyrolysation has been done at temperatures from 900 °C to 1200 °C from about half an hour to a few hours. Wu et al. deposited the PyC on a mesoporous substrate. Due to the conformal nature of CVD, the resulting surface was also porous. The porosity of the resulting surface could be adjusted with deposition time. The advantages of CH_4 as a deposition precursor are its fast deposition rate, low content of pyrolytic intermediates, and the lack of need for solvents catalysts and carrying gases.

Spun precursors

Zhou, Hong et al. [11] studied a PyC film structure on silicon. The film was derived by spinning from a polymeric precursor photoresist SPR 220.7. Pyrolysation and cooling were done in nitrogen atmosphere, from 700 °C to 1000 °C, with 1 h pyrolysation time. The fabrication resulted in a film with a thickness of 10 μm and a smooth, nonporous surface.

SU-8 is a polymer that is commonly used in microfabrication as a negative photoresist. It consists of a mixture of predominantly aliphatic base rubber-like polymer material, and a photosensitive crosslinking agent which will crosslink the polymer when exposed to UV light. According to the X-ray photoelectron spectroscopy (XPS) measurements by De Volder et al. [24] SU-8 pyrolysed at 900 °C forms carbon films and volatile components (including most of the oxygen containing functional groups) will evaporate. Oxygen content drops from 21.8 ± 0.2% to 0.53 ± 0.4% [2, 25]

SPR 220.7 and SU-8 are both readily patternable into complicated 3D structures, either by photolithography or pressing [17]. This makes them ideal materials for textured PyC surface fabrication. These structures might be useful in affecting cell fate on the surface and improving the electrochemical performance of the material [2]. SU-8 especially can be used to produce extremely fine and precise 3D structures, as during pyrolysation it will experience extreme decomposition. The isometric shrinkage of SU-8 scaffold during the pyrolysation process below 1000 °C is above 50% (up to 80%). Most of the weight loss occurs below 500 °C The extreme condensation will cause SU-8 derived films to be particularly sensitive to the heating and cooling processes. [23, 26]

Mitra et al. [12] used SU-8 to produce a microstrip textured carbon substrate and Amato et al. [9] produced a micropillar structure. Singh et al. [2] fabricated PyCs at various temperatures to study the effect on resulting structure. They found that too fast heating and cooling rates, as well as thick SU-8 layers created poorly adherent films. De Volder et al. [24] applied O_2 plasma treatment to fabricate a carbon nanowire surface structures by two step pyrolysation. Typical pyrolysation for SU-8 is done at between 600 °C and 1100 °C.

The differences between various precursors are collected in Table 1. In general the CVD precursors enable fast, thin and conformal coating, while the deposition and fabrication with polymer precursors is much cheaper and they are easier to pattern.

Table 1. Pros and cons of various PyC precursors.

Precursor	Deposition	Properties
Acetylene	CVD	+ Conformal coating + Well-defined growth rate + Facile graphitization due to pre-existing sp^2 hybridized carbons - Relatively expensive and difficult deposition and patterning
Methane	CVD	+ Conformal coating + Fast deposition + Low content of pyrolytic intermediates + No need for solvent catalysts or carrying gasses - Relatively expensive and difficult deposition and patterning
SPR 220.7	Spinning	+ Easy patterning + Cheap and easy deposition - Nonconformal deposition
SU-8	Spinning	+ Easy patterning even for extremely fine or complicated structures + Facile graphitization due to pre-existing aromatic rings + Cheap and easy deposition - Risk of delamination due to extreme condensation - Nonconformal deposition

2.1.3 **Surface treatments**

Various surface treatments can and have been used to enhance mechanical and electrochemical properties, as well as the biocompatibility of the resulting PyC film. Polishing, cleaning, plasma treatment, electrochemical pretreatment and chemical coatings are among the common options. Basic workings and applications of these treatments are explained below. The basis on how the electrochemical improvements work on the structural level will be discussed in Chapter 3 in more detail. The effects of the biocompatibility improvements will be discussed in Chapter 4.

Polishing and cleaning

Surface polishing is used to get a smoother surface, while simultaneously inducing active areas on the surface. Polishing might be useful for rougher and thicker carbon films but polishing PyCs is counterproductive. The films are already so smooth that any attempts at polishing would only roughen the surface. The film adhesion tends to also be so poor that any polishing steps may well delaminate the PyC films altogether.

On the other hand, cleaning can enhance the surface behaviour by removing undesirable impurities from the surface. There are a variety of chemical and electrochemical cleaning procedures, including, but not limited to solvent treatment, activated carbon treatment and potential cycling.

Plasma treatment

Plasma treatment can be applied to the substrate or the PyC film to improve the electrochemical performance of the resulting material. Typically plasma treatment is done in a vacuum chamber, where the plasma is introduced to the surface. O_2 plasma treatment and N_2 plasma treatment have been previously demonstrated to improve the performance of acetylene originated PyC. [1]. Additionally, O_2 plasma treatment has been used to improve neuron adhesion, spread and growth, as well as nerve growth factor (NGF) induced differentiation of PC12 cells [9]. The electrochemical effects of surface plasma treatments will be further discussed in Chapter 3.1 and the previous effects detected on PyC will be presented in Chapter 3.2.

Chemical coating

Cell proliferation and differentiation may be improved by coating the material surface with appropriate polymers or proteins. Some commonly used coatings are poly-D-lysine, poly-L-lysine (PLL), collagen, laminin, fibronectin and Matrigel [27]. While it would be preferable for the cells to proliferate directly on the material surface, sometimes coating is required. Unfortunately, some coatings might have adverse blocking effects on the electrochemical behaviour of the material.

Electrochemical pretreatment

As mentioned before, potential cycling is used to clean the electrode surface. The electrode is cycled for a set amount of time or a set number of cycles within its water window to remove any excess oxidizing substances from the material surface and the analyte, so they will not hinder the actual measurements. This is considered a mild pretreatment, which only causes minor changes in the surface composition. [28]

Potential step anodization, followed by cathodization, (or vice versa) can alter the surface microstructure of a carbon electrode. The specifics on the surface changes will be later discussed in Subchapter 3.1. Anodization includes holding the electrode at a high positive voltage for a period of time and then at a low negative voltage for a shorter while. Three different surface conditions exist on the electrode during this pretreatment; Firstly an inactive state resulting from inadequate surface cleanliness and functional group coverage, secondly an active oxidized surface after anodization, and thirdly an active reduced surface after cathodization. Anodization at too high potentials (>1.5 V) might cause damage and roughening of a carbon surface microstructure. [3, 28]

2.2 **Structure and material properties**

When discussing the structure and specific mechanical properties of a material, one has to account for the fact that these properties are always dependent on the fabrication process. The properties may not be the same when using a different procedure. Therefore findings made with one material should not be assumed to apply to materials with different fabrication histories. More general conclusions (applicable on all PyC materials) should only be drawn if similar properties appear consistently in different studies. The specific structure of each PyC material is highly dependent at least on the precursor used, on the temperature, atmosphere and duration of pyrolysation, on the cooling process and on possible surface treatments.

In general, the surface structure of PyC is that of nanocrystalline graphite. The materials have both sp^2 and sp^3 hybridized atoms, with sp^2 hybridization being clearly dominant. The fabrication temperature is one of the most defining factors in the structure of a PyC surface. A large number of edge planes is typical for the material. Raman spectra, XPS, atomic force microscopy (AFM), X-ray diffraction (XRD), electron energy loss spectroscopy (EELS) and scanning electron microscopy (SEM) are among the many commonly applied tools to quantify these properties. Raman spectrum is especially common in studying and classifying carbon materials and a brief description of the method is given below.

When a photon hits a material surface, mostly elastic scattering called Rayleigh scattering will occur. Simultaneously an inelastic Raman scattering of a much lower probability is also detected. The resulting Raman peaks are the result of this scattering. The scattering occurs when the light quanta interact with the bonds within the material, losing energy before the scattering. The Raman spectrum is a common and facile albeit limited way to distinguish between the bond types present in carbon films and estimate the size of the sp^2 hybridized domains. [29]

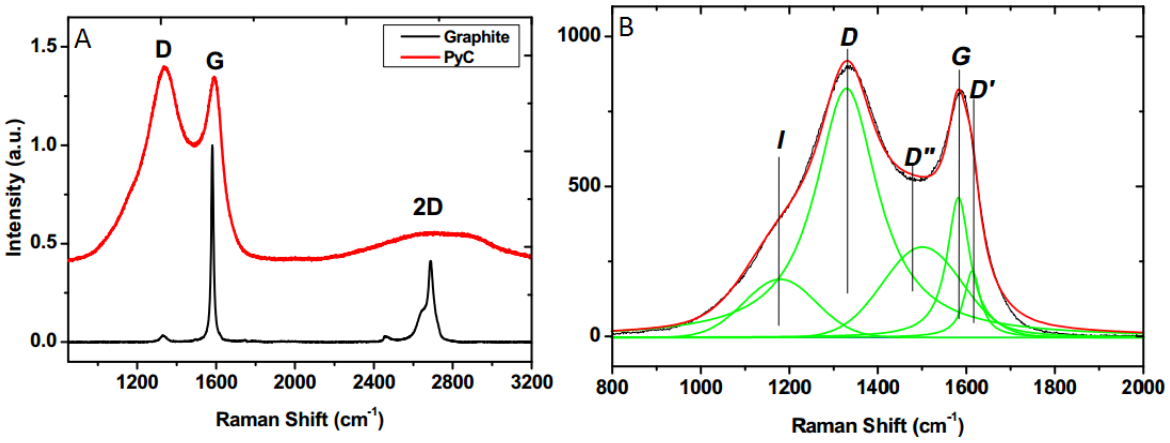

Figure 3. Raman spectra of a CVD PyC film. A) shows the Raman spectrum in comparison to that of graphite. B) Shows the different peaks appearing in the spectrum. [1]

Figure 3A shows typical D and G bands visible in a PyC material, as well as the peaks seen in a pure graphite film. D and G peaks are characteristic for all amorphous carbons and many of the carbon properties can be estimated from the peak shapes. Figure 3B shows various peaks, besides the usual D and G peaks, that can be fitted in PyC Raman spectrum. In Table 2, the properties and implications of each band are described. While typically only the D, G and 2D bands are clearly visible as peaks in the curve, the rest of the bands can be mathematically fitted into the overall shape of the Raman shift curve. [1, 29]

Table 2. Implications of the various peaks visible in a PyC Raman spectrum.

Band	Shift cm^{-1}	Explanation
G	1580	Visible in both graphite and PyC, the G band is observed in all carbon systems containing sp^2 hybridized electrons. The band does not disperse in materials with graphite crystallites. It gets wider for sp^2 atoms with a lot of sp^3 neighbours.
D	1330	Not observed in pure graphene, The D band can be seen in all carbon materials with structural defects such as edges, vacancies and dopants. The in-plane graphitic crystallite size L_a of the material can be calculated from the ratio between D and G band intensities (I_D/I_G). The ratio also aids in estimating the ratio of sp^2 and sp^3 bonds on the surface.
2D	2700	An overtone of the D band, but does not require a defect for activation. Intensity is related to the spatial uniformity in either the graphitic plane or the interlayer spacing.
D'	1620	Occurs in defective graphitic systems and manifests as a shoulder on the G band.
D"	1500	Related to the prescence of tetrahedral amorphous carbon.
I	1180	Linked with disorder in the graphitic lattice, the prescence of polyenes, as well as sp^2-sp^3 bonds.

Ferrari and Robertson [30] have presented a three stage model for interpreting the Raman spectra of carbon materials. It describes the carbon material structure and sp^3 proportion according to the D and G band intensity ratio I_D/I_G and the G peak position.

The three stages are as depicted in Figure 4. Stage 1 includes graphitic materials with different crystallite sizes and 0% sp^3 content. These materials have I_D/I_G from 0 to 2 (or higher) and the G peak position between 1580 cm^{-1} and 1600 cm^{-1}. At the highest I_D/I_G ratio, and with G band peak at 1600 cm^{-1}, the material is nanocrystalline graphite with 0% sp^3 content. At stage 2, the sp^3 content grows from 0% to around 20%, as the G band peak shifts to around 1510 cm^{-1} and I_D/I_G ratio drops to around 0.25. These materials are amorphous carbon materials. At stage 3 are tetrahedral carbon materials, which have an sp^3 content above 20%. Here the G peak position shifts back upwards, while the I_D/I_G ratio keeps decreasing. Both I_D/I_G and G band position are easily seen in the Raman spectrum and can be used to determine the sp^3 content and graphitic crystallite size of the carbon material, using the graphs in Figure 4.

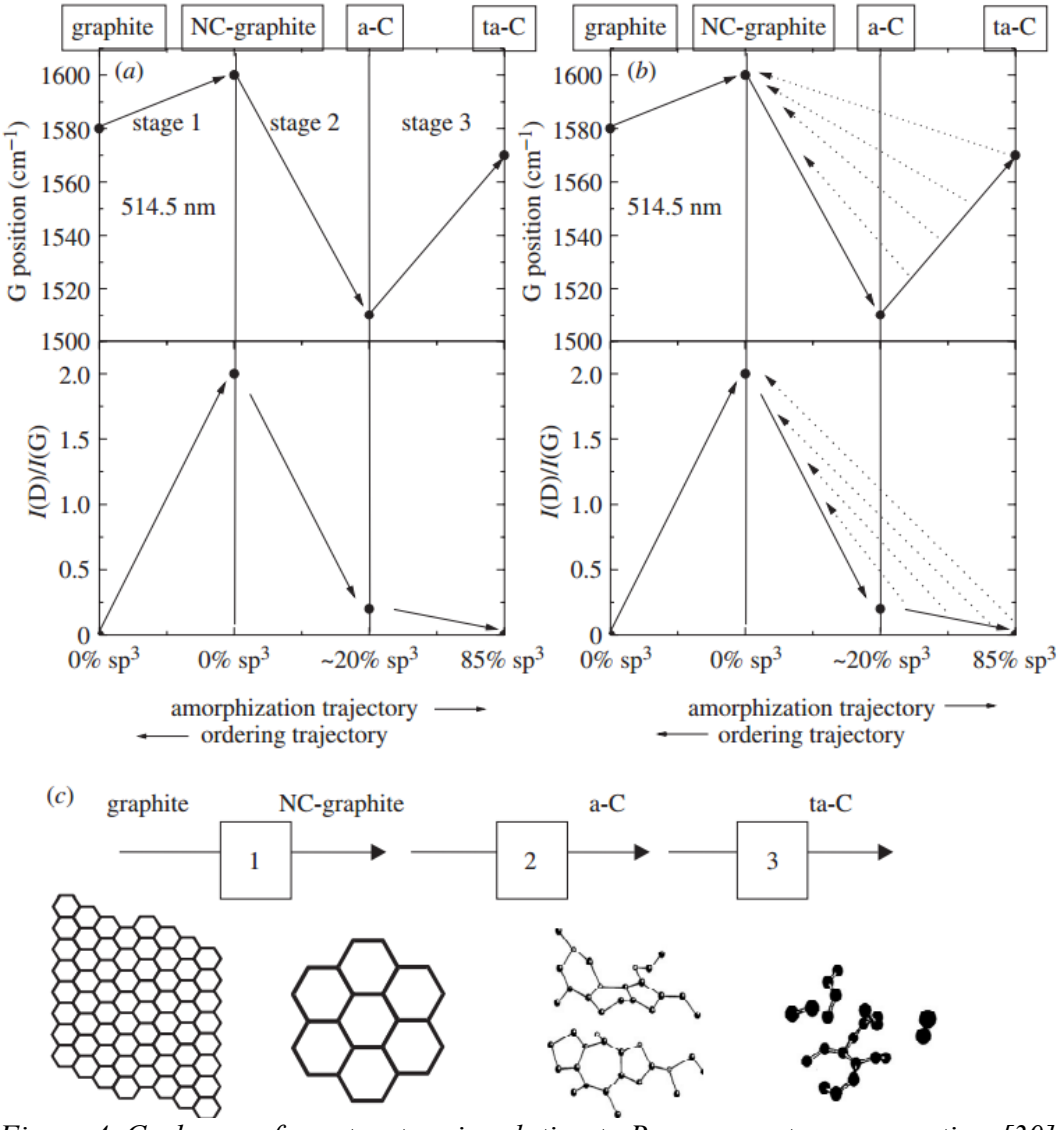

Figure 4. Carbon surface structure in relation to Raman spectrum properties. [30]

However, the model fails somewhat with materials annealed or fabricated in high temperatures. With these materials the D peak intensity increases and the sp^3 ratio can not be determined from the two variables any longer. [31]

PyCs have been previously divided into low, medium and high textured materials. The division is based on the ratio of graphitized carbon to amorphous carbon, or in other words, the difference between G and D peak intensities, with higher G peak indicating a more ordered structure. They can also be divided according to their in-plane crystallite size L_a, which can be also estimated for nanographitic materials from the Raman I_D/I_G ratio. Equations 1 and 2 are used to approximate L_a from the initial laser energy E_l and wavelength λ_l (in nm) respectively. [15, 22, 32]

$$L_a(nm) = \frac{560}{E_l^4}\left(\frac{I_D}{I_G}\right)^{-1} \quad (1)$$

$$L_a(nm) = \left(2.4\times10^{-10}\right)\lambda_l^4\left(\frac{I_D}{I_G}\right)^{-1} \quad (2)$$

Due to the way the carbon is formed during pyrolysation, and due to the minimization of the sp^2 bonding energies, the expected structure of the resulting film consists of small planes of sp^2 hybridized aromatic carbon and amorphous carbon structures in between the planes. Depending on the fabrication, some 5-membered and 7-membered rings are expected to be present, especially at the edges of the graphitic areas. [22]

The general properties of various PyC films, created with different precursors, are described next. Comparison of these materials is then done in Table 3 at the end of this Subchapter.

Acetylene-based CVD PyC

AFM of the material by McEvoy et al. [1] showed the root mean square (RMS) surface roughness to be below 1 nm. This means their PyC films were extremely smooth. For example carbon nanotube (CNT) composite films typically have a roughness above 10 nm. The group also discovered that the roughness did not increase with increasing film thickness. However, at temperatures higher than 1050 °C, crystallites larger than 50 nm in diameter began to form and the surface roughness was increased.

Laminar deposition and domains of about 2 nm in diameter were observed with SEM. Fast Fourier transform (FFT) also implied a highly textured PyC. The small domains mean the film has a large amount of active edge sites, which is often considered important for the electrochemical behaviour of a carbon material. [1]

Nanocrystalline nature, a lack of spatial uniformity and the presence of both graphitic and tetrahedral carbon were all indicated by Raman spectroscopy (Figure 3B) of the samples by McEvoy et al. Varying growth conditions did not appear to have much effect on the disorder level nor the crystallite size, so an analogous growth mechanism for the temperature range between 950 °C and 1050 °C was assumed. [1]

Zhang et al. [13] discovered that PyC coatings of different densities resulted in different types of disorder. Additionally, thermal treatment at 1800 °C or 2000 °C reduced the degree of disorder more in high density coatings. The effect of thermal treatment increases the domain size, as well as the degree of graphitization in these films. This is because the amount of in-plane defects drops at temperatures between 900 °C and 1200 °C due to reorientation and removal of interstitial defects. The additional treatment at 1800 °C and 2000 °C further decreases the degree of disorder, as some defects only reorganize and heal in higher temperatures. The low density coatings exhibited 5-membered carbon rings that would hinder the movement of defects.

Zhang et al. [13] also observed a linear relationship between Young's modulus, hardness and film density up to densities of 1.9 g/cm^3. Higher densities would not further increase the Young's modulus and hardness. Hysteresis was observed in the material behaviour when loading/unloading curves were studied. The degree of hysteresis appeared to be controlled by PyC density and thermal treatments.

McEvoy et al. [1] measured a sheet resistance of about 2.02×10^{-5} Ωm, using a four-point probe. The resistivity was found to increase in thinner films, deposited for less than 10 minutes. However, sufficiently thick (>50 nm) PyC films show a good electrical and thermal conductivity and they can carry high current densities without suffering from size effects. XPS done on the film showed small traces of O, N and F on the film surface. At least C-OH, C-CF, C-N, CF-C and COOH/COOR were found to be present. The main peak also indicated the presence of polyaromatic or graphitic structures with sp^2 hybridization, as well as delocalization of p shell electrons. A SiO_2 indicative peak was observed. The oxide is probably formed in the high temperatures when the film dissolves into the substrate.

Methane-based CVD PyC

SEM images of the PyC material by Hadi et al. [3] showed rounded features of 5 – 10 μm in diameter and the film thickness was observed to be around 45 μm. The Raman spectrum (Figure 5) of the material indicates a crystallite size of about 3 nm. The G peak shifting below 1600 cm^{-1} indicates the prescence of amorphous carbon. The intensity of the G peak is relatively higher and sharper than the one observed by McEvoy et al. [1] with their acetylene-based PyC. This suggests a large number of sp^2 hybridized sites with possibly some sp^3 sites in between. The density of active edge/defect sites can also be considered relatively high due to the high disorder level. This can be considered a favourable feature when using PyC as an electrode material, because the electron transfer process is often fast on these sites.

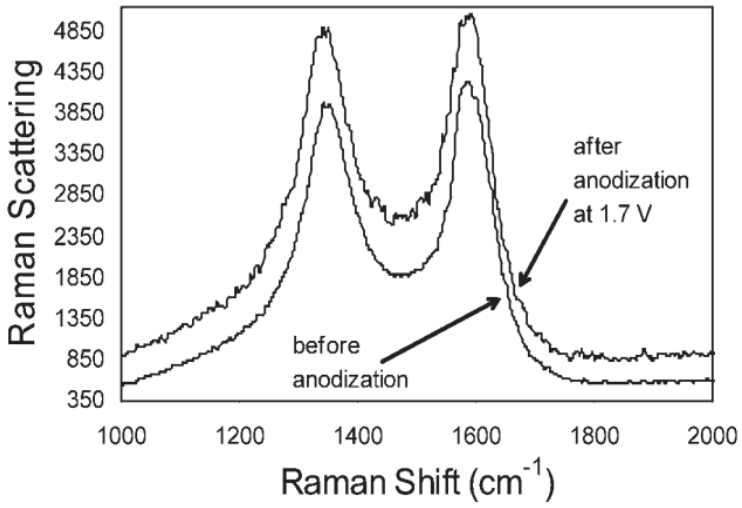

Figure 5. A Raman spectrum of a methane derived PyC film. [3]

SU-8-based PyC

The carbon structure fabricated by Singh et al. [2] was extremely smooth even at nanoscale. Electron diffraction pattern showed a distinct lack of crystallinity at fabrication temperatures up to 1100 °C. This is because the process of complete graphitization of carbon will not reach completion until at 2700 °C. Conductivity increases with increasing graphitization, however the increase in conductivity slows down after 850 °C.

The Raman spectrum in Figure 6, is from a PyC created by Steach et al. [18]. The spectrum shows bands similar to the bands in Figure 3. This indicates again a high number sp^2 hybridized structures. However, the D peak appears to be more prominent than the G peak, which would suggest a higher disorder level and lower sp^3 content, making the material a nanocrystalline graphitic carbon. A large amount of edges and otherwise similar behaviour might still be expected from the material.

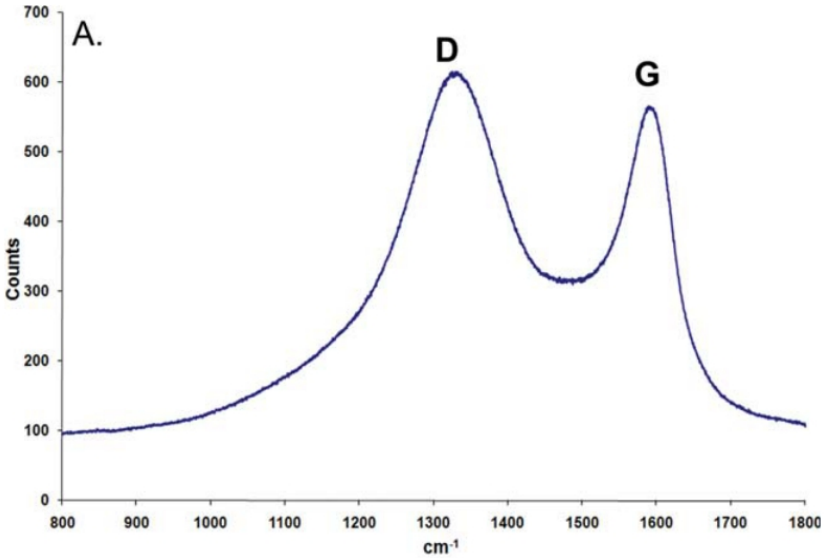

Figure 6. A Raman spectrum from SU-8 derived PyC. [18]

A very specific effect of O_2 plasma treatment on SU-8 pillars was suggested by De Volder et al [24]. They fabricated SU-8 micropillars and subjected them to a harsh O_2 plasma before pyrolysation at 900 °C. They suggested that antimony contained within SU-8 is accumulated on the surface during the plasma etching. This was confirmed by XPS, where the post-etch surface was found to consist of up to 19% antimony. It was found to cause a wire-like structuring of the SU-8 surface, which was then pyrolysed. The wire diameter was about 100 nm before pyrolysation and as small as 15 nm post-pyrolysation. The effect was suggested to be enhanced by different etch rates of the aromatic and linear parts of the SU-8 polymer chain. These effects are largely different to post-pyrolysation plasma treatment effects and should not be confused with them.

De Volder et al. [24] performed XPS characterization on a SU-8 film (Figure 7A), the pre-pyrolysation O_2 plasma treated SU-8 film (Figure 7B) and the pyrolysed film (Figure 7C). They also performed Raman spectroscopy on the nanostructured and nonstructured SU-8 PyC. The XPS curves show that practically all of the oxygen from the resist is evaporated during the pyrolysation process, the C-O + C=O peak being the only prominent peak to begin with. No traces of antimony were found either. According to the Raman spectrum, the nanowired PyC seems to be more amorphous than its regular thin film counterpart.

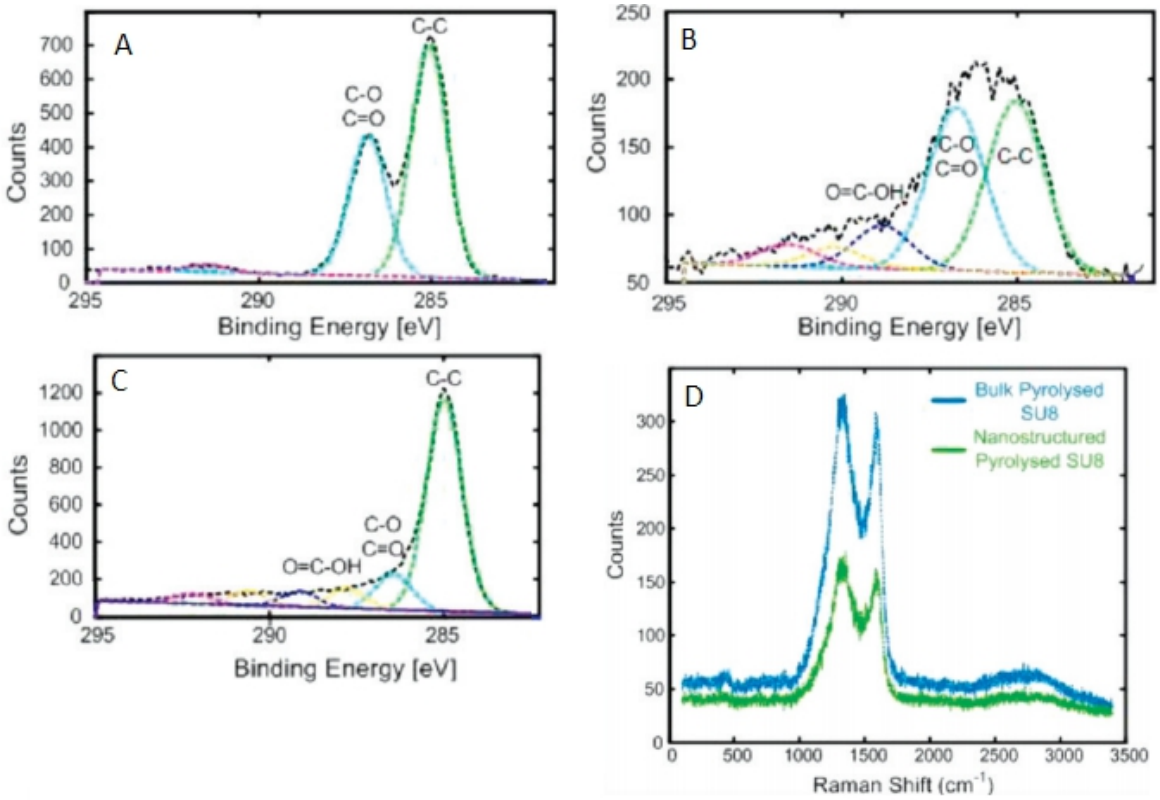

Figure 7. XPS curves from A) SU-8, B) O_2 plasma treated SU-8, and C) Pyrolysed SU-8. D) Raman spectra from bulk pyrolysed SU-8 (blue line) and nanofiber SU-8 (green line). [24]

Amato et al. [9] found O_2 plasma treatment to drastically decrease the contact angle of SU-8 derived carbon to values below 20°, thus resulting in a hydrophilic surface. They attributed the change to carbon oxidation, rather than increasing surface roughness, which was supported by AFM results. An extremely small 2.4 Å surface RMS roughness was calculated. A resistivity of about $1.6 \pm 0.3 \times 10^{-4}$ Ω m^2 was measured for the film.

Lee et al. [26] studied general properties of various SU-8 PyCs, pyrolysed at temperatures between 600 °C and 1000 °C. They found the average surface roughness to be below 0.8 nm for all fabrication temperatures, with 900 °C PyC having the smoothest surface (roughness ~ 0.7 nm). The highest hardness was also measured from the 900 °C PyC (~6 GPa), with the hardness dropping with both decreasing and increasing pyrolysation temperatures. Similarly for the elastic modulus, the maximum values (~55 GPa) were seen with 800 °C and 900 °C PyC films. Resistivity was found to drop with increasing temperature, but the drop in resistivity slowed down rapidly after 800 °C. The films fabricated in temperatures above that, all showed resistivity of about 10^{-2} Ωcm.

Some generalizations of PyCs can be made. PyCs are nanocrystalline in nature and show a relatively high degree of disorder. In the Raman spectrum, the D and G bands are roughly equal in intensity and rather well separated. They all exhibit a high density of edges, promising to show a high electron transfer rate. The ratio of sp^2 hybridized atoms seems to be quite high in relation to sp^3 hybridized atoms, making pyrolysed carbons largely graphitic in nature. Different PyC materials are compared to each other in Table 3. Methane-based PyC seems to have the largest crystallite size (in the μm scale), as well as the most defined G band, while the crystallite size with Acetylene and SU-8-based PyCs are in the nm scale. Methane-based PyC also differs from the other two in its high surface roughness of μm scale.

Table 3. Comparison of the structural properties of Acetylene, Methane and SU-8 derived PyC materials.

	Acetylene	Methane	SU-8
Raman	D band more pronounced than G band.	G band more pronounced than D band. Sharper peaks.	D band more pronounced than G band.
Domain size	Nanocrystalline nature, sp^2 hybridized domains of about 2 nm.	Larger sp^2 hybridized domains, of about 5 -10 μm in size.	A distinct lack of crystallinity, or extremely small sp^2 hybridized domains.
Edge density	High	High	High
Surface roughness	Extremely smooth films, roughness below 1 nm.	High surface roughness on the micrometre scale.	Extremely smooth films, roughness below 1 nm.

2.3 **Other carbon-based materials**

To properly understand the structure and properties of PyC films, they need to be inspected in relation to other carbon-based materials. Due to the unique ability of a carbon atom to exist in three different hybridizations; sp^3, sp^2 and sp^1, there is a large variety of possible carbon structures with different crystallites and levels of disorder. Adding to the complexity, the amount of hydrogen and oxygen terminations also plays an important role in carbon film properties. Carbon films consist mainly of sp^3, sp^2 hybridized atoms, as sp^1 hybridization only exists as a chain-like linear structure. The different configurations can bee seen in Figure 8.

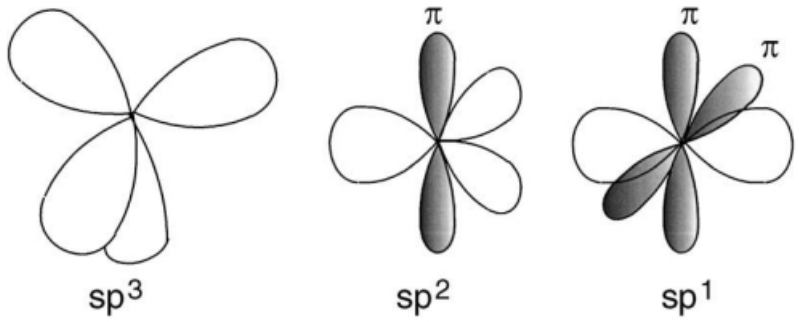

Figure 8. Three types of carbon hybridization. [33]

In the sp^3 configuration, the four valence electrons of a carbon atom are all directed tetrahedrally on sp^3 orbitals. These electrons are called σ electrons and they form strong σ bonds to the adjacent atoms. Bulk diamond consists of a sp^3 hybridized carbon network and the properties arising from this are further discussed in 2.3.2. [33]

The sp^2 configuration has three triangularly directed sp^2 orbitals in a plane. They form three strong σ bonds with the adjacent atoms. The last valence electron is directed normal to the σ bonds on sp^2 hybridized orbital. Electrons on these orbitals are called π electrons and they form a weaker π bond with one or more adjacent atoms. While the σ bond only exists between two neighbouring atoms, the π electron might be delocalized and shared with all of the three neighbours. Sp^2 hybridized carbon atoms form planar carbon structures. Graphite, graphene and CNTs consist mostly of sp^2 hybridized atoms. Various properties of these materials are further discussed in 2.3.1. [33]

Disordered carbon films consisting of σ and π bonds are called amorphous carbons. They exhibit properties that arise from both of the hybridization types. Amorphous carbons are a large and versatile family of materials and PyC films are a type of amorphous carbons. Various other amorphous carbons, such as tetrahedral amorphous carbon (ta-C) and glassy carbon (GC) are described in 2.3.3.

2.3.1 **Graphite, graphene and carbon nanotubes**

When minimizing bonding energy, the sp^2 hybridized atoms tend to form planar planes of typically 6-membered benzene-like carbon rings, in which the π electrons are all bonded with all three adjacent carbon atoms. These layers are typically stacked by van der Waals bonds and form a multilayer graphite structure. A single-layer structure of this kind is called graphene and it exhibits very specific properties. CNTs on the other hand are fullerene terminated rolled graphene sheets.

Graphite sheets are held together by the weak van der Waals bonds that move around easily. This makes the bulk graphite one of the softer carbon materials. Graphene is a thermal and electrical conductor along the basal plane, but an insulator perpendicular to the basal plane. This is because the delocalized π electrons of the basal planes are free to move around. However, direct electronic bonding between the stacked planes is rare. [34]

The basal planes are not susceptible to the chemisorption of oxides, but the edge sites are. This is because in the basal plane, all the electrons are bonded to the neighbouring carbons, so no chemical bonding with oxygen can occur. At the edges and at defect sites, there are hydrogen terminated σ bonds or free radicals, on which chemisorption of molecular oxygen will occur more easily. This is especially true for the zigzag and armchair patterns of a graphitic edge, which are so called active sites on a graphitic material. [35]

Defect-free single-crystal graphite barely reacts with oxygen at all, but usually some edge sites exist, as large single-crystal materials require extremely high annealing temperatures. Often some sp^3 hybridization is present in the structure and it is concentrated on the edge sites of the basal areas. As the size of sp^2 crystallites decrease and the ratio of sp^3 hybridization increases, the material will no longer be graphite. Instead, it will start having amorphous nature. [35]

Figure 9A shows a Raman spectrum of a single-crystal graphite and Figure 9B shows a spectrum of a commercial graphite. As evident from the Figure, only the G peak is evident in the single-crystal graphite, while a relatively small D peak can also be seen in the commercial graphite Raman shift. The disorder level of the material in commercial graphite is therefore greater than that of single-crystal graphite and it has a larger number of edge sites. [29]

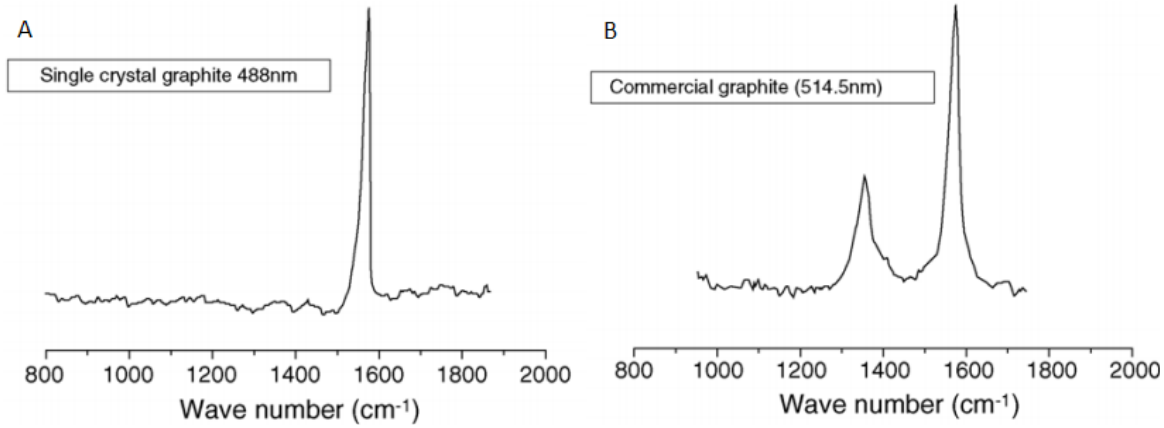

Figure 9. Raman spectra of: A) single-crystal graphite, and B) commercial graphite. [29]

Single-layer graphitic film, graphene, is an atomically thin structure. While it derives many of its properties from its graphitic structure, it also exhibits some very unique properties that differ from graphite. For one graphene shows increased conductivity both on the basal plane, as well as through the material. It is no longer considered an insulator, as no crossing over the van der Waals bonded gaps between the sheets is required.

Graphene is considered a zero band gap semimetal. It exhibits an anomalous quantum Hall effect and graphene electrons behave like massless Dirac fermions. As with graphite, large single-crystal graphene is also rare. Most commonly graphene exists as structures with varying sizes of sp^2 crystallites. From the viewpoint of utilizing graphitic materials in electrochemical sensing, this is typically considered to be a good thing, as the existence of the edge states facilitates carbon bonding with organic molecules. Electrochemically nanocrystalline graphene has been shown to exhibit fast electron transfer kinetics and wide potential windows. It has also been used to detect multiple different analytes, such as DA and serotonin. [36, 37]

Graphite and Graphene are the basic form of graphitic carbon structures and in that sense very similar to the nanographitic PyC materials. The main difference between them is the crystallite size, which is extremely small in PyC. Unlike Graphite and Graphene, PyC is full of edge sites, which are usually considered to be more electrochemically active than the graphitic basal plane. Usually PyC does not exhibit any long range order either and is instead more amorphous.

Similarly to graphene, CNTs also form a very specific structure with many characteristic properties. From the point of view of the electrochemical and electric behaviour of the CNTs, the curved form of the graphitic surface is among its most important features. The reason for this is that while the sp^2 orbitals of graphene tend to be unable to induce chemisorption of oxygen functional groups, the sp^2 orbitals of CNTs are distorted due to the curved surface. This causes them to be shaped more like sp^3 orbitals instead. This has been suggested to make CNT surfaces more electrochemically active, as well as electrically and thermally more conductive; an effect that increases with decreasing CNT diameter. CNTs differ greatly from other graphitic materials as they do not form planar films. [38]

2.3.2 **Diamond**

Diamond structure consists solely of tetrahedrally located, σ bonded, sp^3 hybridized carbon atoms. The diamond structure is known for its extreme hardness, which it exhibits due to the rigidly oriented and strong σ bonds holding it together. [28]

The dangling σ bonds on a diamond surface are typically terminated hydrogen. Oxygen termination is also possible and the surface is susceptible to chemisorption of molecular oxygen. Compared to graphitic structure, diamond shows uniform conductivity, which is better through the bulk, but worse along the surface. [29, 39] Figure 10 shows the Raman shift of single-crystal diamond. As all the bonds in the structure are equal, only one sharp D peak is visible.

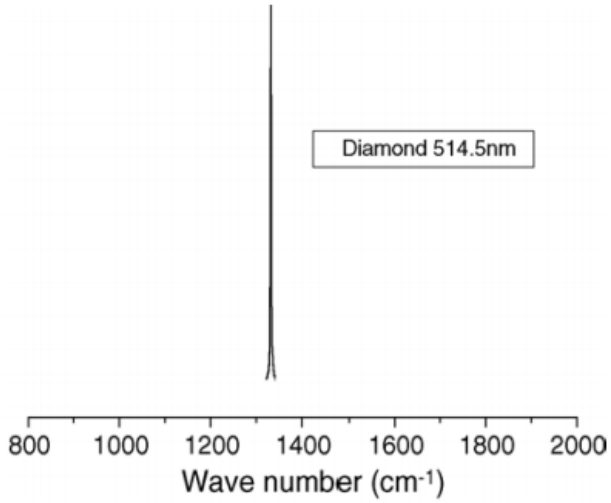

Figure 10. Raman spectrum of diamond single-crystal. [29]

Compared to PyC and other graphitic materials, diamond shows poor conductivity due to the lack of conducting π electrons. It is also a much harder material because of the tetrahedral orientation of the bonds.

2.3.3 **Amorphous and nanocrystalline carbon films**

The existence of both sp^2 and sp^3 hybridized atoms is typical for amorphous carbon films. Amorphous carbon films do not show the long distance order characteristics typical for diamond and graphite, but the bonds do intermix and extend order on a nano scale. In a usual configuration that minimizes bonding energies, the sp^2 hybridized atoms tend to cluster into aromatic graphitic planes, while the sp^3 hybridized atoms and randomly oriented sp^2 atoms are located in between those planes. For large enough clusters, nanocrystalline graphite and nanocrystalline diamond structures can be observed. [29]

The exact distinction between a nanocrystalline and an amorphous carbon is somewhat unclear. Nanocrystalline materials with small crystallite size can be seen as a kind of a border case of an amorphous carbon. With the model of Ferrari and Robertson (as presented previously in Figure 4), amorphous carbons range from stage 2 to stage 3. Nanocrystalline diamond exists at the end of stage 3 and nanocrystalline graphite in the beginning of stage 2.

Amorphous carbon properties vary hugely in respect to their sp^2/sp^3 ratio, as well as the amount of hydrogen bonded in the material. The two hybridization types provide amorphous carbon materials with both diamond-like and graphite-like properties. The presence of hydrogen makes for softer, more polymer-like carbon films. In general amorphous carbons might be classified into polymer-like, diamond-like and graphite-like carbons, based on the main binding framework and surface terminations. Figure 11 visualizes this division. [28, 32]

Discerning between σ and π bonds with visible light is not possible. This is because π bonds have a much lower energy and they are more dominating in visible light Raman, as the energy of the light is enough to excite the π electrons. UV light Raman, however, has sufficient energy to excite the σ electrons and allows the sp^3 sites to be directly observed. Figure 12 shows the UV-Raman spectra of amorphous carbon films with various sp^3 proportions. There are many other ways to determine the ratio and they are complementary to Raman. X-ray spectroscopy is among the most potent ones. It has high sensitivity to chemical shifts and is very useful in characterizing doped amorphous carbon films. [29, 33]

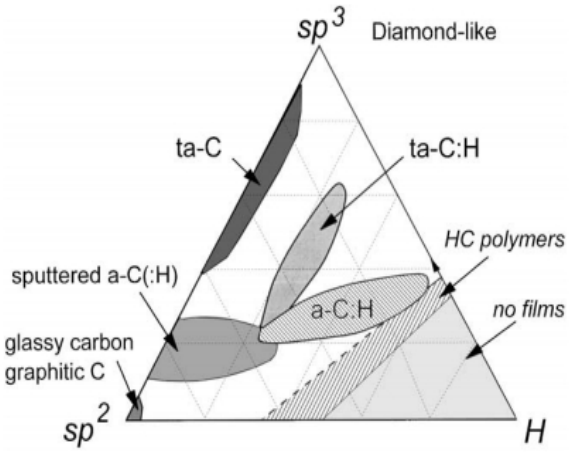

Figure 11. Sp^2, sp^3 and hydrogen proportions of various carbon materials. [32]

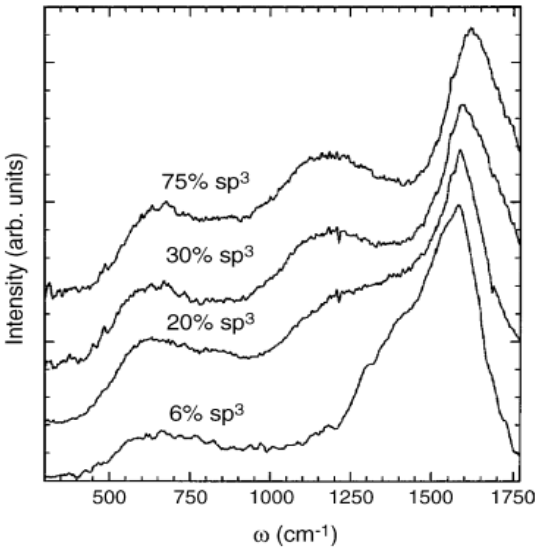

Figure 12. UV-Raman of amorphous carbon films with different sp^3 *contents. [29]*

Figure 13 shows the Raman spectra for six different kinds of amorphous carbon films. A large sp^3 concentration is characteristic for ta-C (Figure 13F) and nanocrystalline diamond (Figure 13A) films. They show many diamond-like properties, such as hardness, electrical and electrochemical inertness and a wide band gap. [29, 33]

Nanographite (Figure 13B) is an example of a graphitic amorphous carbon, with a high content of sp^2 sites. These films typically show comparatively high intensity and sharpness of the G peak. There are many resemblances of this Raman shift to those of PyC seen previously, which suggests a relatively high sp^2 content and similar domain size in them as well. [29] GC Raman (Figure 13C) shows a very distinct peak separation and sharp D and G peaks. It is a highly disordered carbon that microscopically consists of a mixture of graphite-like ribbons or microfibrils.

Amorphous carbons with more even proportions of the two bond types and high disorder levels (Figure 13E), and carbons with high hydrogen content (Figure 13D), show a much poorer peak separation. They are softer materials, usually formed at lower temperatures. The presence of hydrogen seems to increase the Raman intensity at the side of the G peak. [29]

PyC materials are a group of nanocrystalline graphitic materials, so they have properties of both amorphous carbon materials and graphitic materials. They do not exhibit much of a long distance order and they consist of small graphitic planes. PyCs fabricated in lower temperatures are more amorphous in nature and have a higher sp^3 concentration. Those fabricated in high temperatures are more graphitic, with little to no sp^3 hybridization present.

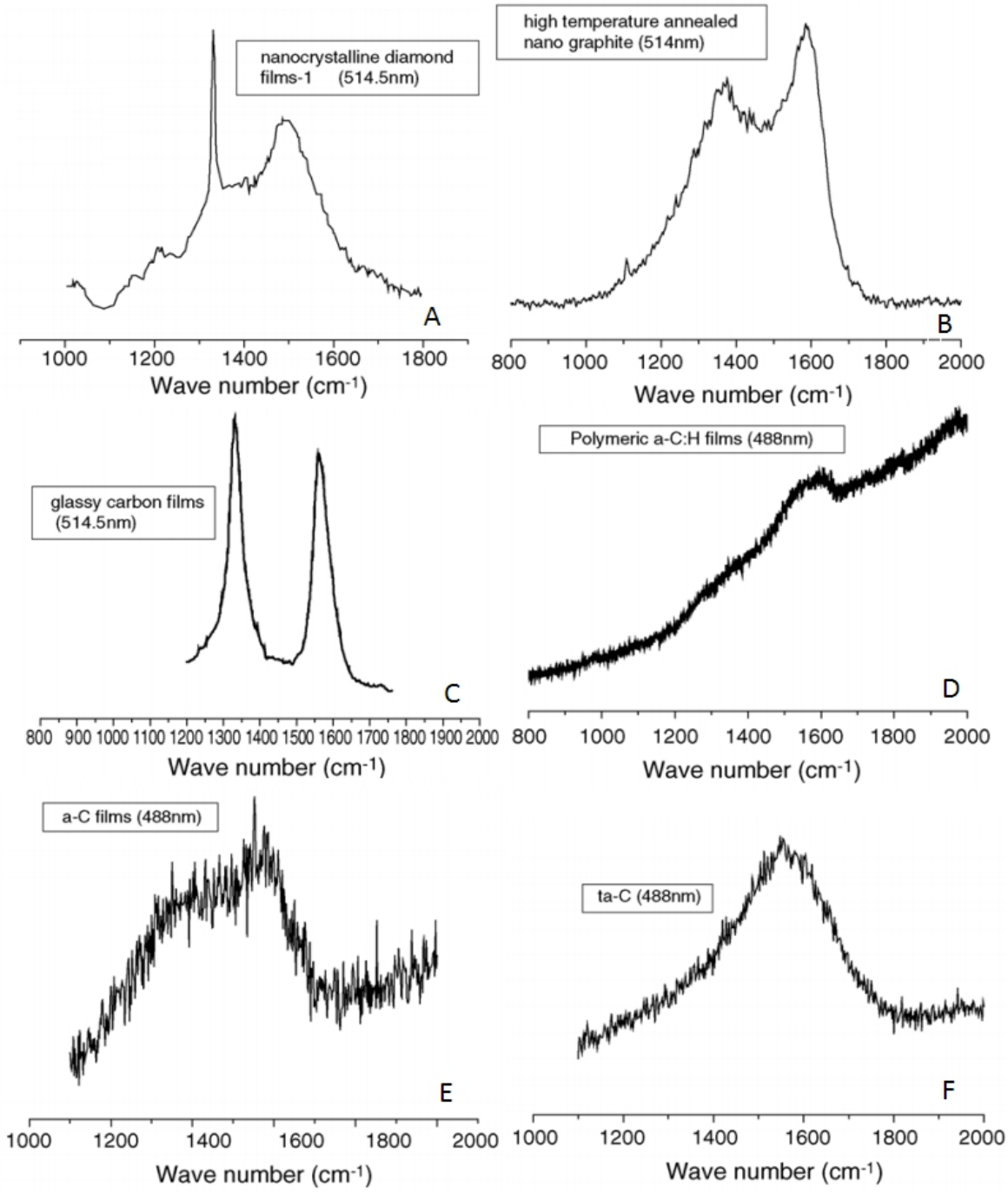

Figure 13. Raman spectra of: A) Nanocrystalline diamond. B) Nano graphite. C) GC. D) Polymeric amorphous carbon. E) Amorphous carbon. F) ta-C. [29]

3 Electrochemical properties of PyC

Electrochemical measurements are done in an electrochemical cell. The behaviour of the working electrode is measured in a liquid analyte, against a known reference electrode. There are various electrochemical characterization methods available, including but not limited to voltammetric methods such as linear sweep voltammetry (LSV), cyclic voltammetry (CV) and differential pulse voltammetry (DPV). These methods can used to study both the analyte and an electrode material.

CV is one of the most relevant of these methods. It is widely utilized in the characterization of carbon materials and it is a well developed tool which provides comparable results of both oxidation and reduction behaviour of the electrochemical cell. It loses in sensitivity to DPV, but it has a superior scanning speed and temporal resolution. In CV, the electric potential in the cell is cycled between two desired values for one or more cycles. If the electrolyte contains any electrochemically active molecules that are oxidized or reduced within the potential cycling range, they will be shown as peaks in the current/voltage curve. The current is measured on the working electrode. [28, 40]

Inner sphere redox systems (such as DA) form strong (covalent, ionic or metallic) bonds with the working electrode surface. The electrochemical response of a given carbon material towards inner sphere redox systems tends to be extremely sensitive towards the surface properties of the electrode material. Even small changes in the chemistry, charge or structure of the surface easily affect the response of the material. These changes are often specific to each analyte. Thus the specific surface properties and their characterization is detrimental to understanding the oxidation and reduction behaviour of these systems. Outer sphere redox systems, in contrast, are surface insensitive. Their response can be seen more as a result of the electrical properties of the surface region. Various redox systems will be further reviewed in Section 3.1.3 [40, 41].

The use of CV and the analysis of its results in studying carbon materials are briefly described in the beginning of Subchapter 3.1. Both physical and chemical phenomena affecting carbon electrochemistry are discussed. Some relevant surface treatment methods for improving the performance of electrodes are then presented in 3.1.4. Subchapter 3.2 attempts to summarize the previous work done on characterizing the electrochemical properties of PyC materials. Various properties, significant from the electrochemical sensing point of view, are described and discussed.

3.1 Carbon electrochemistry

As discussed previously in Chapter 2, carbon materials include a large number of various materials with diverse properties. This is attributed to the complex structure of these materials. The complexity arises from both the structural polymorphism and the diverse surface chemistry of carbon materials. [40]

It naturally follows that the electrochemistry of carbon is a similarly complex phenomenon, factored to structural and chemical properties of the carbon, as well as the properties of the redox system in question. For example, the fabrication process and the surface treatments of the materials, as well as the cycling speed, measurement temperature and pH all have a hand in the resulting current/voltage curve.

3.1.1 **Electron transfer and reversibility**

Electron transfer rate can be used to describe the speed in which the redox reactions occur on the working electrode. It is the rate at which electrons can move from the donor to the acceptor. From a CV curve, it can be defined from the separation of oxidation and reduction peak voltages, with a lower peak separation correlating with faster electron transfer. The electron transfer rate can differ with the same material from one redox system to another. [41]

With optimally fast electrode kinetics, the electron transfer is solely limited by mass transfer and the electrode surface is in electrochemical equilibrium. This kind of system is called a Nernstian system. A reversible oxidation-reduction behaviour is an intrinsic characteristic of Nernstian systems. This means that all of the oxidized analyte will be reduced back into the original form during potential cycling. A theoretical value for CV curve peak separation (ΔEp) for this kind of a system is about 59 mV at 25 °C for a single electron transfer (and half of this for the transfer of two electrodes, et cetera). Additionally the intensity ratio of oxidation and reduction peaks I_{po}/I_{pr} equals to 1 for reversible reactions. In reality, no redox system behaves completely reversibly, but near reversible behaviour can be detected. [42]

Figure 14 shows three different electron transfer behaviours. The dotted curve shows a fast electron transfer rate reaction with oxidation and reduction peaks at about 0.45 V and 0.55 V against the reference electrode. The resulting ΔEp is around 0.55 – 0.45 V ~ 100 mV. The oxidation peak for the dotted line I_{po} is around 0.1 mA and the reduction peak I_{pr} is also around 0.1 mA, so the peak current ratio I_{po}/I_{pr} is quite close to 1. While the resolution in the Figure is not good enough to specify the exact values, the behaviour of the dotted line can be described near reversible.

The solid line, in contrast, shows a significantly slower electron transfer rate. The curve shows a peak separation ΔEp of about 900 mV. The oxidation peak I_{po} equals to about 0.04 mA and, while the size of the reduction peak is not too much lower (around 0.03 mA), the behaviour is clearly irreversible according to the peak separation alone.

An almost reversible reaction is called “quasi-reversible”. Most “reversible” reactions are in reality quasi-reversible. The electrode kinetics of these reactions tends to slow down with higher cycling speeds. A reaction might be quasi-reversible because of slow electron transfer rate, but it might also be quasi-reversible if not all of the oxidation product is reduced back to the original form. This might be for example if the oxidation product further reacts into another form. The dashed line in Figure 14 is an example of a quasi-reversible reaction. [41, 42]

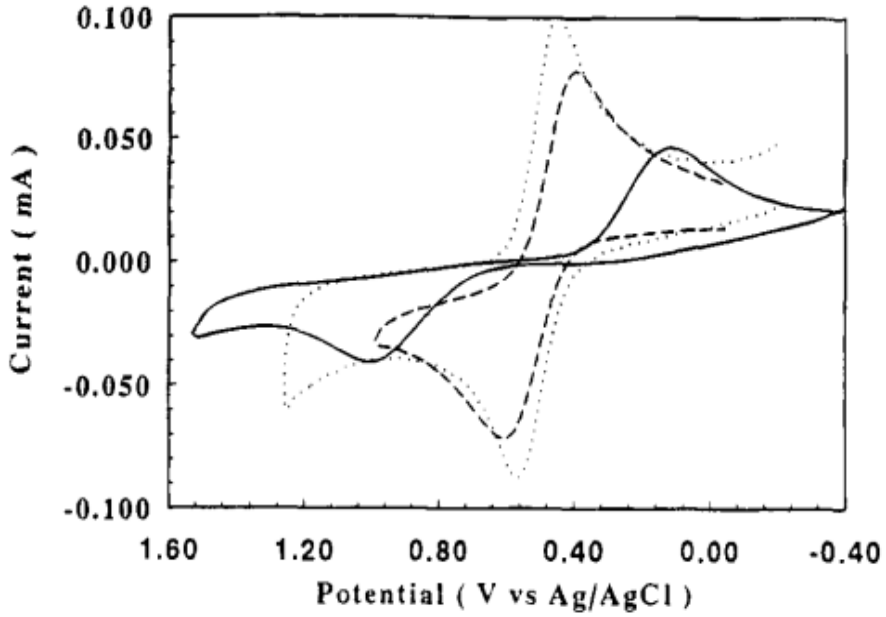

Figure 14. Voltammograms with different peak separations. The dotted line shows a voltammogram of a reversible reaction. The reaction presented with the dashed line is quasi-reversible, and the reaction drawn in solid line is irreversible. [41]

According to McCreery et al [40], the electron transfer rate is highly dependent on the density of electrically active states (DOS) around Fermi-level. In the case of carbon materials, those states are mostly composed of edge planes and impurities. When it comes to graphitic carbons, the armchair and zigzag areas of basal plane edges serve as the active states. Oxygen containing functional groups and any surfactants may also affect the electron transfer rate, although these effects are highly dependent on the redox system in question. Additionally, surface polarization can also have an effect on the adsorption of certain ionic redox agents on the surface. The electron transfer rate of carbon materials might be additionally limited by the carbon film thickness and perhaps even properties of the substrate material. [28, 40]

From a viewpoint of a uniform basal graphitic or graphene sheet, the filled valence band overlaps with the conduction band. This results in a low DOS near the Fermi-level, which is why the basal planes of graphitic materials are often thought to be less electrochemically active than the edges. The introduction of the edge planes and other defects creates defect states which have energies in between the two bands. These energies fill the DOS near the Fermi-level, making the material more electrochemically active [40, 41]. The amount of the edge planes (and as such the size of sp^2 hybridized basal planes in graphitic carbons) is consequently linked to the electrochemical reactivity of the material.

More recent findings by Lai et al. [43] reveal that the issue is far more complicated. The results will not always correspond to the model presented on the previous page. Instead, they show that freshly cleaved basal graphitic planes show near reversible behaviour for common outer sphere redox systems. It is suggested that the basal plane electroactivity decreases after cleaving due to surface fouling and resulting blocking effect.

Another significant factor in the electrochemical behaviour of a graphitic carbon is the surface termination, which affects the behaviour of inner sphere probes [37, 38]. While all the electrons on the basal plane are bonded to adjacent carbon atoms, the dangling bonds at the edge sites are often terminated with hydrogen or an oxygen containing functional groups, such as carboxylates and quinones. Oxygen containing functional groups tend to affect the electrochemical behaviour of the surface towards specific inner sphere redox systems, typically by lowering their electron transfer rate. Depending on the application, the effect may be either hindering or beneficial. While PyC tends to have a low oxygen content on the surface, there are ways to control the amount of oxygen post-fabrication. Those methods are briefly discussed in 3.1.4. [28]

3.1.2 **Potential window**

The potential window can be defined as the potentials during which the current remains relatively unchanged within a certain solution, during potential ramping or cycling. Within this potential window, the background current from the solution will not extensively hinder the measurement of oxidation and reduction peaks of analytes. Potential windows are defined separately for different solutions. [28]

There is not one specific guideline on how to choose the exact points where potential window starts and ends, as the current ranges change drastically between materials. However, the current change at the edges of the potential window is so rapid that the variation between different potential window evaluations is not usually significant. For more sloped potential windows, such as can be seen in Figure 15A, the distinction is less obvious. In general, a wider potential window is always preferable. This is attributed to the fact that a wider potential window can show a larger variety of oxidation and reduction peaks, as the voltage is stable on a larger range of potentials.

Besides the width of the potential window, the scale of the background current within the window is also a notable feature of the behaviour of a carbon electrode. A current flowing in the electrochemical cell consists of so called faradaic and nonfaradaic currents, which can both be seen in a CV voltammogram. Faradaic current consists of all currents created by reduction and oxidation of chemical species on the electrodes, or in other words, all currents involving electron or proton transfer. All other current is nonfaradaic, composed mostly of charging (capacitive) current, caused by the electric double layer on the working electrode. The nonfaradaic and faradaic currents are dependent on the electrode area, with a larger area corresponding to a larger background current. [28, 42]

Electrodes exhibiting lower background currents have potential to be more sensitive in detecting low analyte concentrations. This is because smaller changes in the current will be visible during potential cycling. However, comparing background currents between different materials should only be considered an approximation, as the background current changes as a function of electrolyte composition, pH, and cycling speed. [28, 40]

Figure 15 shows three different kinds of potential windows. The potential windows in 15 A range from 0 V to 0.5 V against the reference electrode, resulting in window width of 0.5 V. It is notable that the current increases quite a lot even within the potential window, making the curves sloped. The background current is quite high in relation to the narrow window width.

The curve in Figure 15B shows a high background current of about 80 µA and another potential window of 0.5 V. The background current is more stable within this window (less sloped curve shape) than those in Figure 15A. Lastly Figure 15C shows an ideal potential window with an extremely low background current and a window width of almost 3 V. It should be noted that while both 15B and 15C show a potential window of a GC electrode, the two windows are clearly different. This demonstrates the effects that arise from different electrolytes, electrode properties and scanning speeds.

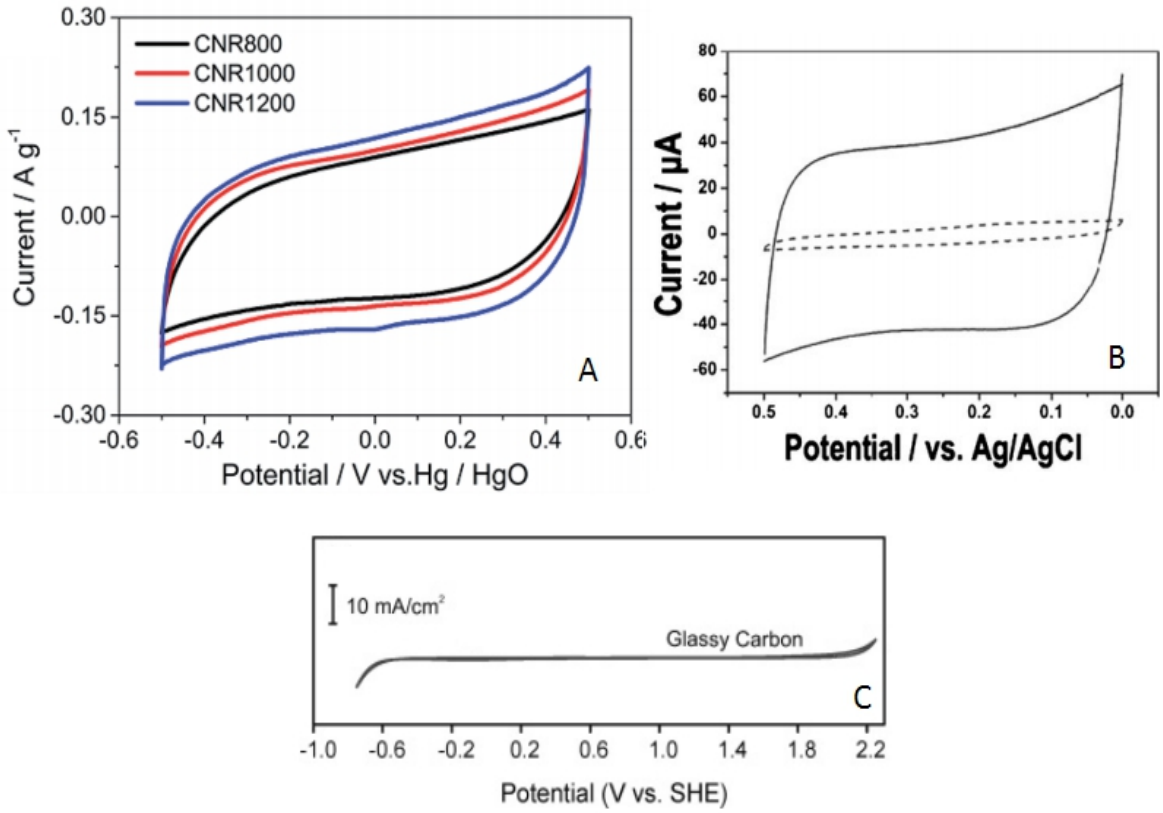

Figure 15. A) Sloped potential windows for carbon nanorods in 1 M NaCl (1 mV/s). B) A potential window of low background current for GC (dashed), and a high potential window from graphene-modified GC (solid) in 1M KCl. (100 mV/s) C) A wide potential window with a low background current from another GC electrode in 0.5 M H_2SO_4. [42-46]

For a material to be usable in electrochemical neurotransmitter measurement, the oxidation-reduction reactions will need to occur on the material surface, within the potential window of the material. If the oxidation-reduction peaks of an analyte appear outside the potential window of the material, they will be distorted or not at all visible in the high current. It is essential for the oxidation and reduction peaks to be located within the potential window in detecting the neurotransmitters.

3.1.3 **Redox systems, selectivity and sensitivity**

Besides the material being able to detect the desired analyte at all, the selectivity and sensitivity of the material to specific analytes is important. Biological fluids are complex and contain a large variety of organic molecules at all times. For a sensor to be able to detect concentrations of a specific analyte, the peak of that analyte must not overlap too much with other analytes. Instead, a sufficient peak separation is required. If the peaks of other analytes do not interfere with the peak of a specific analyte, the material is said to be selective towards that analyte. In biological environments, many of the chemical species also appear at very low concentrations. The sensitivity of a material to a certain species depends on the lowest concentration the oxidation appears in. The lower the detectable concentration is, the more sensitive the material is to the species. The size of the background current the material exhibits is important in regard to its sensitivity in general, as high background currents tend to raise the detection limits and distort appearing peaks.

To characterize and compare the electrochemical behaviour of various carbon materials, a number of known redox probes with known behaviours may be used. So called outer sphere redox probe are surface insensitive, in a sense that they are mostly insensitive to surface defects, impurities, chemistry, et cetera. As such they are used to compare the intrinsic electron transfer properties of carbon materials, defined by the surface structure of the material. In contrast, inner sphere redox reactions are extremely sensitive on the surface functional groups and exhibit strong bonding to the surface. [40, 42]

$Ru(NH3)_6^{3+/2+}$ is a nearly ideal outer sphere redox probe with no known chemical interactions with a surface. As such, it acts as a completely null case for electrocatalysis. FcMeOH (ferrocenemethanol) is another surface insensitive outer sphere redox probe that has been used in abundance to study carbon materials [47, 48]. In contrast $Fe(CN)_6^{3-/4-}$ is often mistakenly used as an outer sphere system. However, it is somewhat dependent on both surface chemistry and interactions with cations in the solution [39].

As mentioned in Chapter 1, being able to detect DA and measure its concentrations in vivo is one of the primary objectives when developing carbon materials to function as neural sensors. Unlike the outer sphere redox systems, the cationic DA is sensitive both to surface oxides and surface polarization. ECE, ECC, and ECECEE mechanisms have all been suggested for DA electrochemistry (E stands for electrochemical reaction and C stands for chemical reaction). [10]

The first electrochemical step in all of the mechanisms is between DA and dopaminequinone (DAQ), and can be seen in Figure 16. This corresponds to the primary DA oxidation peak observed during CV. This electrochemical reaction is reversible as DAQ can be reduced back to DA. However, DAQ can further react chemically into leucodopaminechrome (LDAC). This reaction is irreversible and causes the DA oxidation-reduction reaction to be irreversible also. During DA electrochemistry, a second oxidation-reduction pair can often be seen at lower voltages. According to the ECE mechanism (as shown in Figure 16) this would correspond to the reversible electrochemical reaction between LDAC and dopaminechrome (DAC). [10]

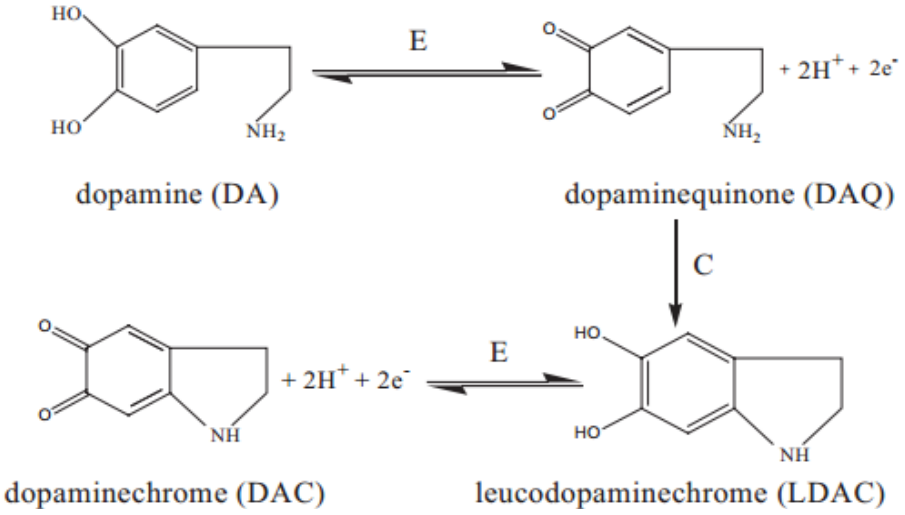

Figure 16. ECE mechanism for dopamine electrochemistry. [49]

In biological environments there are many other redox systems as well. If their peaks overlap with that of DA, they might interfere with or completely prevent its detection. A major interfering system is AA which exists in biological systems in much higher quantities than DA. On carbon materials, the oxidation peaks of the two also tend to be in a close proximity to each other. AA does not show a reduction peak as it has an irreversible oxidation reaction. [50]

Some redox probes have very specific responses to certain surface functional groups. They can be used to pinpoint a functional group to which another redox system is sensitive. Such probes include carbonyl group specific dinitrophenylhydrazine and hydroxyl group specific dinitrobenzoylchloride. [40]

3.1.4 **Modification of electrochemical behaviour**

Aside from changing the fabrication process of the carbon material itself, it is also possible to modify the electrochemical performance of the material with post-fabrication surface treatments as was mentioned in Chapter 2. The effect of surface cleaning on electron transfer is obvious enough, as impurities blocking active sites and slowing down electron transport are removed. Cleaning with Isopropyl alcohol (IPA) has been suggested to be one of the most efficient and nonintrusive way to activate PyC film electrodes. [28]

Besides surface cleaning, other methods to affect the electrode behaviour either disrupt the surface microstructure, increase or decrease the amount of oxygen termination on the surface, or induce electric charge on the surface [28, 40]. The methods which may be used to improve the sensitivity or selectivity of the surface to DA are the ones presented here in more detail. Anodization and oxygen plasma treatment will be specifically discussed in this section.

The process for anodization was described in Chapter 2. Treatment in a potential outside the potential window is used to disrupt the surface via electric tensions. Anodization has been shown to modify the surface microstructure and cause surface roughening in high voltages. Voltages higher than 1.5 V can significantly change surface topography and structures. Anodization also increases the O/C ratio of graphitic films and ionizes the surface. Depending on the redox pair used, anodization has both accelerated and decelerated the electron transfer. [28, 40]

There have been multiple suggestions on the source for the effects seen on graphitic materials after anodization. One possibility is that the changes in surface microstructure induce more active graphitic edges which then oxidise and provide more sites for specific redox pairs. According to other suggestions, the edge sites themselves act as facilitators of proton exchange or as sites for contamination. Ionization might also be an important factor, as cationic surface would attract anionic molecules and vice versa. An effect to the electric double layer has also been suggested. It is difficult to say which of the effects are at work and the result could be any combination of them. However, anodization has undeniably some effect on graphitic surfaces. It has also been previously used to induce DA and AA peak separation on a PyC film electrode [5]. [28]

Oxygen plasma treatment increases surface energy and the amount of oxygen functional group terminations on the surface. Oxygen terminations on carbon surfaces consist mainly of quinones, carboxyl groups and hydroxyl groups. DA has been suggested to be specifically sensitive towards hydroxyl groups so plasma treatment might improve the surface sensitivity towards DA. It might also cause a shift in the DA peak [9, 50]. Improvement of the electrode behaviour occurs also at least partly due to the improved wetting of the surfaces. Wettability improves both the cell adhesion and the reactant adsorption on the surface. Over tenfold increase (from 0.022 ± 0.002 to 0.297 ± 0.001) in O/C ratio has been reported for SU-8 derived PyC during oxygen plasma treatment, albeit the types of these bonds were not characterized [9]. On the other hand, some material properties might be improved by H_2 treatment. It is used to induce hydrogen termination on the surface and subsequently remove oxygen. [40]

3.2 **Previous work on PyC**

In this Subchapter, previous electrochemical characterizations of PyC materials done by various groups are described. The materials are again divided according to the fabrication methods. Special attention is paid to studies which attempt to characterize PyC surface behaviour in DA detection and selectivity between DA and AA. Previous characterizations of films pyrolysed from SU-8 photoresist are especially of interest.

Only a handful of electrochemical characterizations has been previously done on relevant PyC materials. Unfortunately many of the studies utilize insufficiently characterized films, so drawing conclusions from the results of the characterizations is somewhat difficult. The redox probes are also often poorly chosen. Typically only one cycling speed is used in the measurements. When doing DA measurements, mostly high DA concentrations have been used.

3.2.1 **Acetylene-based CVD PyC**

McEvoy et al. [1] studied their PyC material, using Ag/AgCl as the reference electrode material. They utilized $Fe(CN)_6^{3-/4-}$ redox probe in KCl and a scan rate of 100 mV/s. The resulting curve can be seen in the Figure 17 below.

In Figure 17, the black curve shows a large peak separation of about 450 mV. The peak is poorly defined, indicating slow electron transfer. The curves from O_2 and N_2 plasma etched electrodes both show an improved performance. The electron transfer rate and the peak definition have both improved. The results were in accordance with a measured Nyquist plots, indicating a reduced resistance to charge transfer.

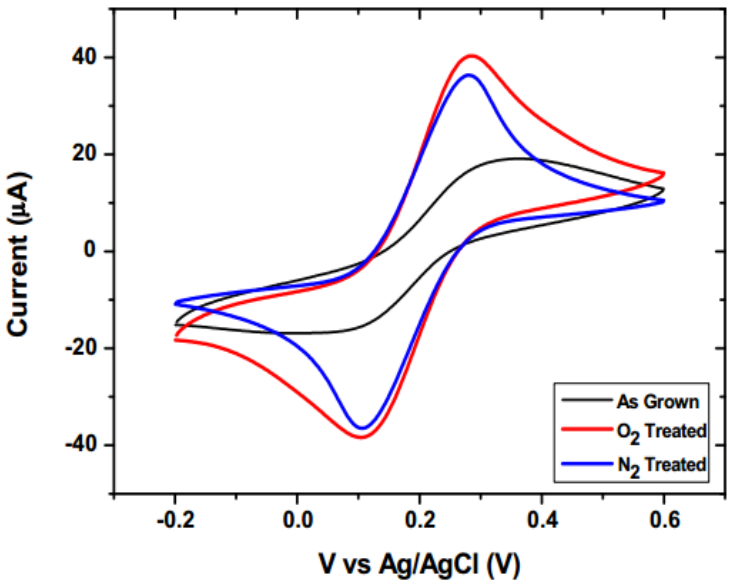

Figure 17. Acetlyene-based CVD PyC CV curve of $Fe(CN)_6^{3-/4-}$ in KCl. Black curve shows the response of the electrode as-grown. Red curve shows the response of an O_2 treated electrode, and Blue curve show shows the response of a N_2 treated electrode. [1]

The surface treatment method was chosen in accordance to a previous study by Keeley et al. [51], which characterized the same material using $Ru(NH_3)_6^{3+/2+}$ (Figure 18A) and $Fe(CN)_6^{3-/4-}$ (Figure 18B) redox probes. Both of the probes show a larger peak current for the O_2 plasma etched electrode, and $Fe(CN)_6^{3-/4-}$ also shows a reduced peak separation. The plasma etching was found to increase the surface roughness and area.

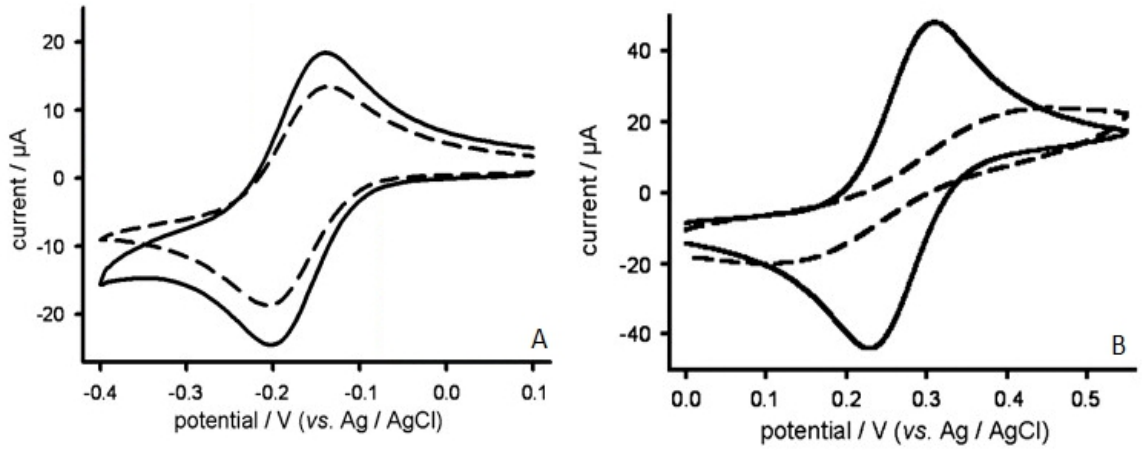

Figure 18. A) Acetylene-based PyC film response with A) $Ru(NH_3)_6^{3+/2+}$ and B) $Fe(CN)_6^{3-/4-}$ redox probes for as deposited (dashed line) and O_2 plasma etched (solid line) electrodes. [51]

Keeley et al. attributed the increase in peak current to the greater electrochemically active area. It seems likely that the change is mostly caused by surface chemistry. The peak shift is only seen with the $Fe(CN)_6^{3-/4-}$ probe, which is known to be sensitive to surface chemistry, while there is only slight change in the surface shape for $Ru(NH_3)_6^{3+/2}$. Post-O_2 treatment XPS analysis revealed a presence of hydroxyl, carbonyl and carboxylic acid functionalities. The presence of these functionalities was confirmed using $Fe^{3+/2+}$ redox probe, which gave no response for as-grown film, but a voltammogram indicative of rapid electron transfer for the treated film.

3.2.2 **Methane-based CVD PyC**

Hadi et al. have studied the electrochemical behaviour of a methane-based PyC electrode with CV in multiple studies [3, 4, 5, 8]. Figure 19 shows CV curves measured with a Methane CVD PyC electrode of a surface area of 0.07 cm^2. A standard Ag/AgCl electrode was used as a reference. Anodization at 1.7 V was applied in attempt to improve the PyC behaviour. Cycling speed of 50 mV/s was used for all of the curves. [3]

The curve in 19A shows a potential window in a 1 M KCl solution for the PyC and a GC electrode. The width of the potential window is wider than 1.6 V. It is wide compared to the potential window of GC (about 1.57 V). On the other hand, it is rather narrow compared to the potential window 2.95 V of boron doped diamond. The background current, measured with a cycling speed of 50 mV/s, is in the scale of tens of nA. It is much smaller than that of GC in the µA scale.

Figure 19B shows the CV curves of PyC and GC of equal surface areas and cycling speeds for 1 mM $Fe(CN)_6^{3-/4-}$ in 1 M KCl. They show a similar reversible electron transfer rates. The ΔEp is about 78 mV for PyC and 67 mV for GC. GC also shows higher oxidation and reduction peaks, making the GC surface more reactive towards $Fe(CN)_6^{3-/4-}$.

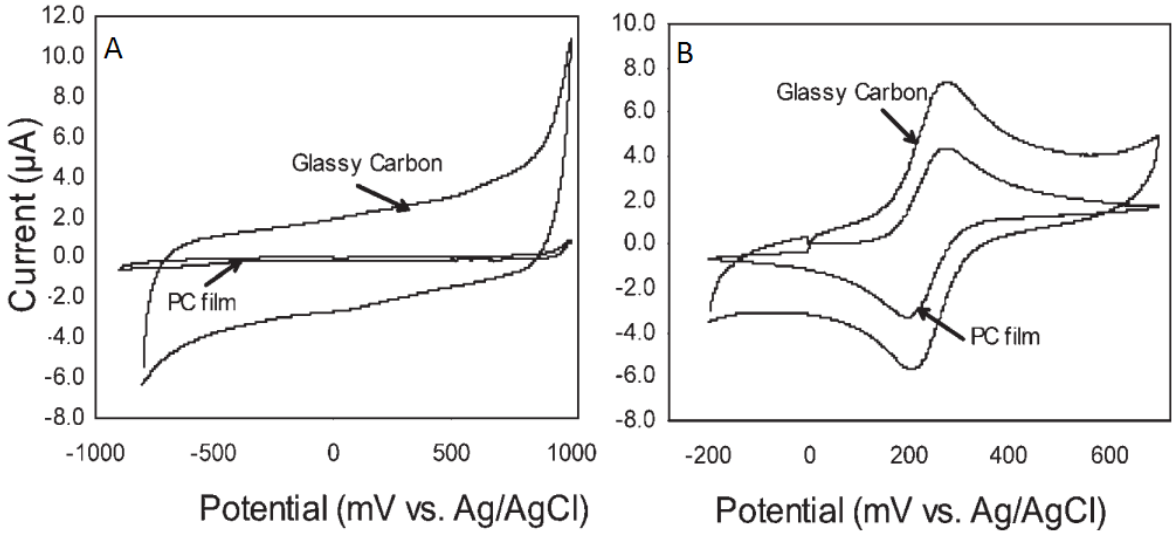

Figure 19. PyC and GC CV curves in A) 1 M KCl. B) 1 mM $Fe(CN)_6^{3-/4-}$ in 1 M KCl. [3]

In Figure 20, curves are shown for 1 mM DA in 0.1 M H_2SO_4. The measurements have been done with a GC electrode, an anodized PyC electrode, and an unanodized PyC electrode. The PyC curve before anodization shows a slow electron transfer and a low peak intensity. Anodization significantly improves the electron transfer rate and the peak separation, making the reaction more reversible than the reaction on GC. However, the initial PyC film shows a slow reaction kinetics.

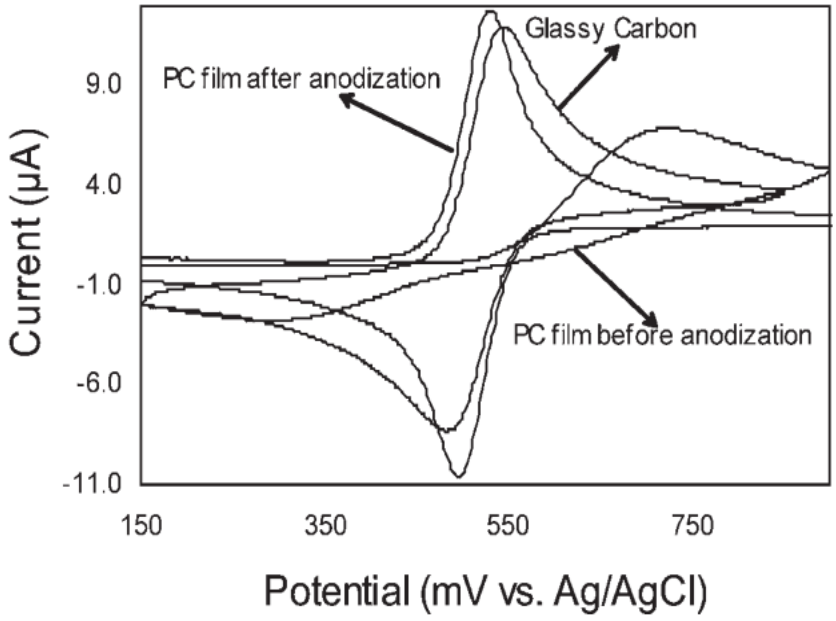

Figure 20. CV curves measured in 1 mM DA + 0.1 M H_2SO_4. The curves are measured with GC electrode, PyC electrode and an anodized PyC electrode. [3]

Hadi et al. [3] attributed the slow DA reaction kinetics to the lack of surface C-O functionalities. Similarly, they attributed the improved behaviour by anodization to the large amount of edge/defect sites on the surface. The sites are thought to be susceptible to the chemisorption of oxides, especially during anodization. This might be why the electron transfer rate on DA improved significantly after anodization, as it is considered to be sensitive to surface oxides.

In another study, Hadi et al. [5] were able to use PyC to separate DA, AA and UA peaks by anodization. LSV and DPV curves from the study can be seen in Figures 21 and 22. A scan rate of 50 mV/s was used for all of the measurements.

Figure 21 shows an LSV curve measured in a 80 µM AA + 9 µM DA + 9 µM UA in 0.1 M phosphate buffer saline (PBS) (pH7) solution. Anodization for 180 seconds was done in 1.3 V (red line), 1.5 V (blue line), 1.7 V (green line) and 1.9 V (brown line). The black line shows an unanodized electrode. With anodization voltages 1.3 V and 1.5 V, the AA peak (left peak in the figure, around 0.15 V) can be seen as a shoulder of the DA peak (middle peak, around 0.3 V). The 1.3 V curve does not differentiate from the unanodized curve at all. At 1.7 V anodization, a decent peak separation, and a better defined DA peak are visible. As for the curve with 1.9 V anodization, the peak separation of AA and DA is reduced and the background current increases drastically.

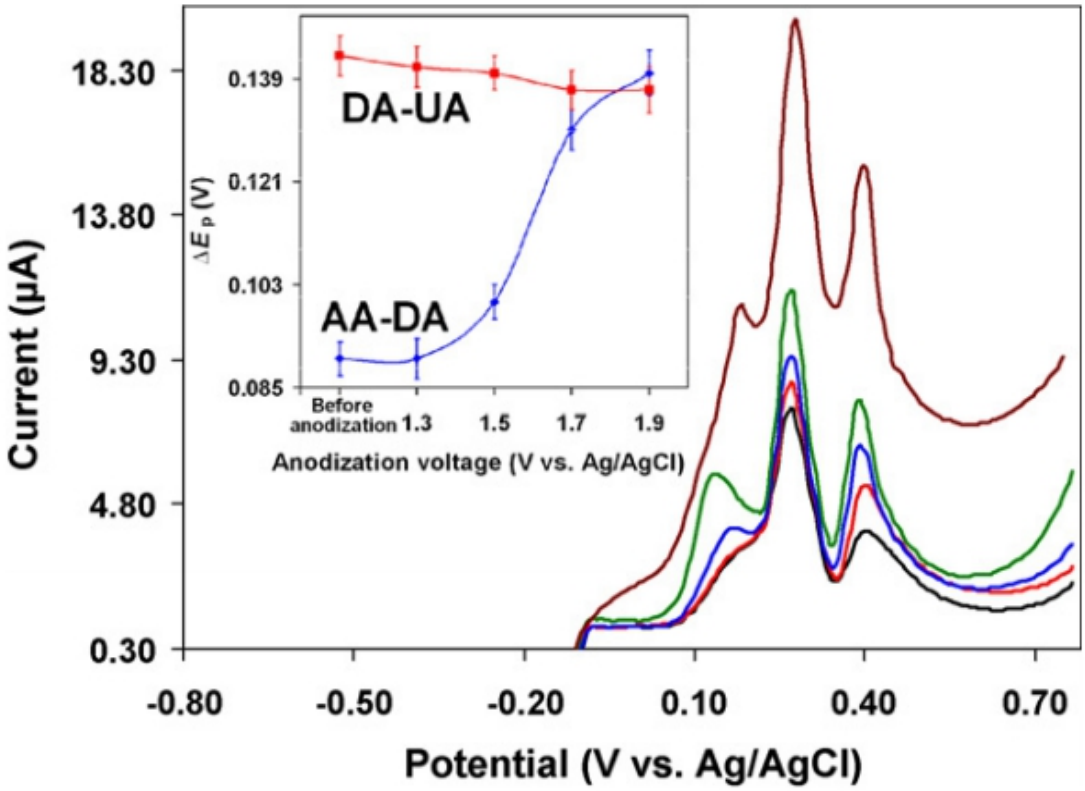

Figure 21. LSV curves showing peak separation with AA, DA and UA. The curves are measured with an unanodized PyC electrode (black), and anodized electrodes with voltages of 1.3 V (red), 1.5 V (blue), 1.7 V (green) and 1.9 V (brown). The curves on the left show the peak separation as a function of the anodization voltage. The red curve shows the DA-UA peak separation, and the blue curve shows the AA-DA peak separation. [5]

UA (right peak, around 0.4 V) and DA peaks are separated well before anodization, as well as at all anodization voltages. UA peak also becomes better defined at with higher anodization voltages, although the peaks slightly approach each other. Hadi et al. attribute this to greater diffusion of UA to the more hydrophilic surface of anodized electrode, enriched by surface oxide groups. These oxide groups are suggested to lead the UA diffusion to the electrode.

Figure 22A shows a DPV curve, measured in a solution with 8 µM DA, 10µM UA, and AA concentrations ranging from 10 µM to 567.1 µM. Figure 22B shows a DPV curve in a solution with 130 µM AA + 5 µM UA + DA concentrations ranging from 0.12 µM to 9.87 µM. The separation can be seen well with all of the concentrations.

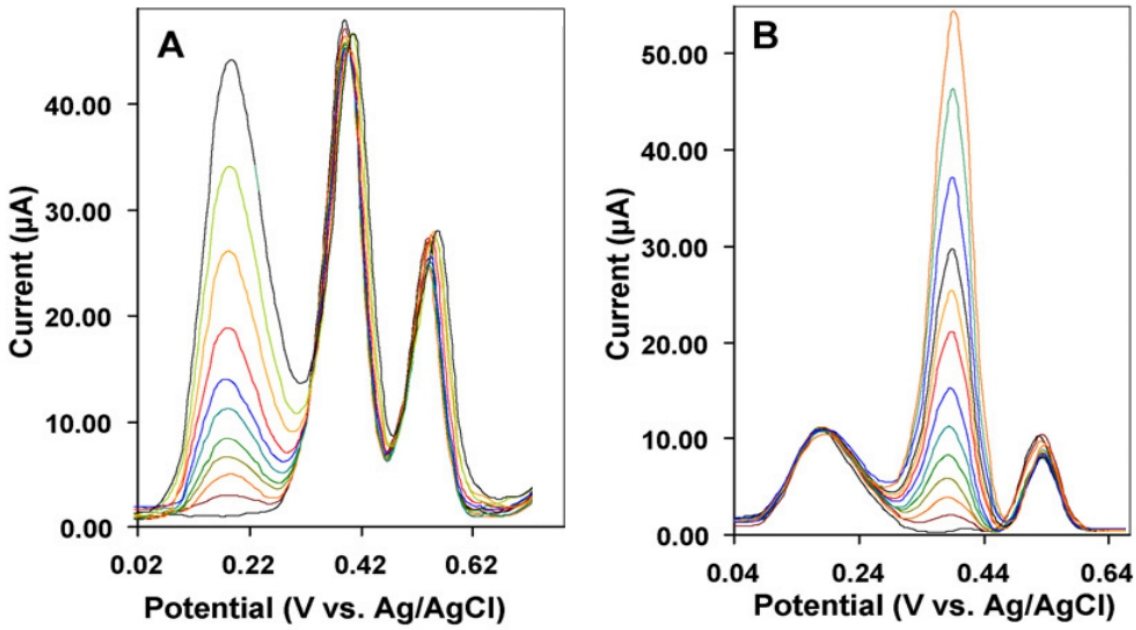

Figure 22. DPV curves, using a PyC electrode, anodized at 1.7V. A) shows a curve in 8 µM DA + 10 µM UA + AA ranging from 10µM to 567.1µM. B) shows a curve in 130 µM AA + 5µM UA + DA concentrations ranging from 0.12µM to 9.87µM. [5]

The DPV curves have better resolution, sensitivity and peak separation than the LSV curves. A peak separation is maintained even when the concentration of AA is about 70 fold compared to DA concentration. LSV also shows peak separation, but it is not as clearly visible and only with only less than 10 fold AA to DA concentration.

Hadi et al. [5] were only able to separate AA and DA peaks, with 70 fold AA concentration in comparison to DA. In an actual in vivo situation within human neural tissue, the concentration of AA is far greater than that still. The concentration of DA in vivo is also hundreds of nM at highest, while here, such concentrations were the lowest ones measured with DPV. It is possible that the peak separation might be lost with realistic concentrations of AA and DA. The CV voltammograms in both of the studies also seemed to show a lot of noise but the articles provided no insight as to why. No measurements for an outer sphere redox probe could be found for the material, nor any specified justification for the use of ferrocyanide in the film characterization.

3.2.3 **SU-8 resist-based PyC**

Amato et al. [9] performed DA CV before and after O_2 plasma treatment of SU-8 derived PyC for both flat and 3D structured carbon films. The CV curves for the 3D structured films in 5 mM DA can be seen in Figure 23 below. Cycling speed of 50 mV/s and a Ag/AgCl pseudo reference electrode were used.

The treatment increased both anodic and cathodic peak currents on both materials, but also seems to have slowed the response. A more optimal orientation of DA electroactive OH-groups was suggested to be the reason for the change. Amato et al. suggest the DA reactions to be mediated by hydrogen bonding capacity of carbonyl and carboxyl functionalities at plasma treated surfaces, which could improve DA sensitivity. However, as was discussed in Section 3.1.4, DA is specifically sensitive towards hydroxyl groups, so that should be more likely. All in all, the results seem inconclusive, as the measurements have been done in an extremely high DA concentration. A lack repetition and poorly described experimental procedure also make it more difficult to properly interpret the results.

The plasma treatment effect was greater with 3D carbon, which was attributed to its substantially larger surface area. With an enhanced wettability, more DA would reach the surface. The redox behaviour of the electrodes seems to be quasi-reversible both before and after the plasma treatment. No specific studies on DA selectivity nor detection limit were presented and the results provided were acquired with an extremely high concentration 5 mM DA solution. Nothing else about the electrochemical behaviour was specified, and the results were presented in an unspecific format (Fig. 23 lacks a y axis).

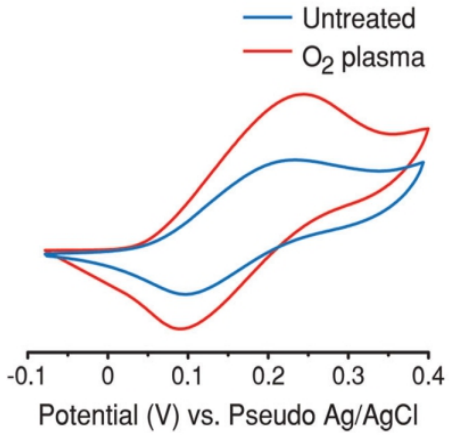

Figure 23. CV of 5 mM DA solution, measured with 3D PyC electrodes. Curves for both untreated (blue) and O_2 plasma treated (red) electrodes are shown. [9]

Singh et al. [2] also characterized their film using $Fe(CN)_6^{3-/4-}$ redox probe (Figure 24). They found that increasing pyrolysation temperature decreases peak current and improves the electrode kinetics. This is indicative of improved film conductivity, which was in agreement with observations made about sheet resistivity.

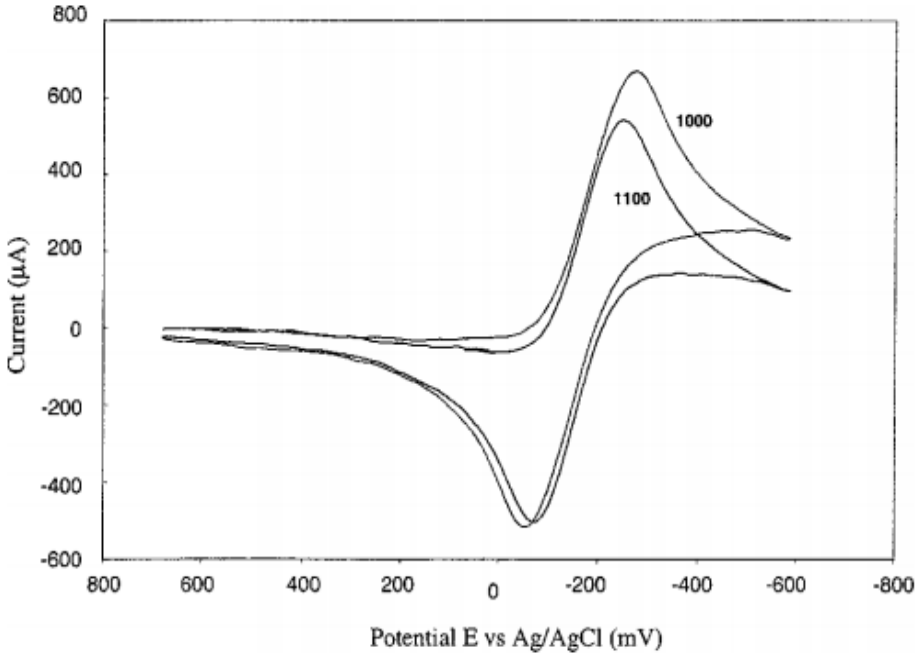

Figure 24. 1000 °C and 1100 °C SU-8 PyC film response to $Fe(CN)_6^{3-/4-}$. [2]

The differences in peak potentials for Fe-based and Ru-based analytes can be found in Table 4. The electrode shows quasi-reversible behaviour for both analytes as an increase in the scan rate shows increase in the peak separation. However, the behaviour is more reversible for the samples fabricated in higher temperatures. In lower pyrolysation temperatures, the difference between the two outer sphere redox systems seems to be less prominent. The rate constants were calculated to be 0.019 cm/s for 1000 °C and 0.026 cm/s for 1100 °C PyC film in $Fe(CN)_6^{3-/4-}$ and 0.017 cm/s and 0.025 cm/s for $Ru(NH_3)_6^{3+/2+}$ respectively. It should be noted that a too narrow scanning window has been used, as the oxidation is still occurring at -600 mV against Ag/AgCl reference. The slope of the peaks is also tilted in a way that indicates a high ohmic drop.

Table 4. ΔEp at various scan rates for Fe and Ru-based probes in SU-8 derived PyC. [2]

Temperature of pyrolysis (°C)	Scan rate		
	200 mV/s	2 V/s	20 V/s
1 mM $Fe(CN)_6^{-3/-4}$ in 1 M KCl			
1000	77	112	212
1100	77	106	183
1 mM $Ru(NH_3)_6^{3+/2+}$ in 1 M KCl			
1000	75	112	208
1100	74	96	166

Table 5 sums up essential electrochemical properties of the PyC materials described in this chapter. While there are some differences between these materials, the information available on especially Acetylene-based CVD PyC is rather scarce and direct comparison is difficult. All in all, PyC materials seem to have µA scale background current and quasi-reversible outer sphere kinetics. At least for methane based PyC, the sensitivity and selectivity towards DA also seem to be quite good (in the scale of hundreds of nM DA at least). There seems to be a strong dependency on surface treatments when it comes to electron transfer rate and DA sensitivity. There is also a lot of variance between the various PyC materials. Unfortunately, $Fe(CN)_6^{3-/4-}$ is typically the only probe used to characterize the material surface. It can not be considered an outer sphere probe nor is it all that informative of the surface electrochemical properties in itself.

While PyCs cannot usually distinguish between the DA and AA oxidation peaks, this has been achieved with relatively low AA concentrations by applying electrochemical treatments. Many other methods have also been applied to improve the electrochemical behaviour of these materials. These include surface plasma treatments and 3D structuring.

Table 5. Electrochemical properties of various PyC films.

	Electrode kinetics ($Fe(CN)_6^{3-/4-}$) as deposited	Sensitivity for DA	AA and DA oxidation peak separation	Improving behaviour	Background current
Acetylene-based CVD PyC	Slow	-	-	O_2 and N_2 plasma treatments	-
Methane-based CVD PyC	Fast	High (at least around 100 nM can be detected)	With anodization, at high DA concentrations	Anodization at 1.7 V	Low
SU-8 photoresist-based PyC	Relatively fast	Not measured in low concentrations	-	O_2 plasma treatment and 3D structuring	Low

4 Biocompatibility of PyC

PyCs are rather well known for their good biocompatibility and they are in frequent use in heart valve implantations among other things [52]. Their compatibility with neural tissue has not been studied nearly as much. This Chapter briefly discusses the methods used to study the neural compatibility of a material, as well as some practical issues involved. Previous studies done on the compatibility of PyC with neural tissue are also presented in 4.3.

4.1 Cell viability

Cellular viability is the ability of cells to survive, proliferate and grow. There are many methods for studying the viability of cells grown in a specific environment. These test can be based for example on the chemical response of the cell culture to specific chemical probes, on the cellular functionality, or on genome sequencing of the cells. In the simplest form, cell viability can be qualitatively estimated by staining and optical microscopy of the cell culture. The viability of cells on a material is perhaps the most important aspect of the biocompatibility of that material.

For quantitative analysis, one the most frequently used assays is based on the tetrazolium salt; 3-(4,5-dimethylthiazol-2-yl)-2,5-diphenyl tetrazolium bromide (MTT). When incubated with cell culture, MTT forms dark purple formazan crystals that are bound to living cells only. The crystals can be dissolved in a translucent solvent, and colorimetric measurement can be used to get a numeric value for the optical density of the solution. Higher optical density of the solvent equals higher viability. A wavelength within the range of 550 – 600 nm should be used because it is specific for the colour of the formazan. [53]

The amount of formazan produced depends heavily on the cell type and there are no general reference values to which the results could be compared. The results are also obviously dependent on the culture area and various other assay variables. This is why known references should be included in the measurements, as the measured values are only directly comparable to the values made in the same measurement. Any comparisons between measurements should be made as percentages to known references. [53]

4.2 Neural and dopaminergic differentiation

The effect a surface has on the growth and differentiation of a cell line is another important aspect of its biological response. To electrochemically measure neurotransmitters within the brain, it would be desirable for the electrode material to be in contact with neurons. The same is especially true for dopaminergic neurons when DA is the neurotransmitter in question. If the implant causes scar tissue forming around it, it might be encapsulated and insulated from the rest of the brain. Seeding the implant surface with neural stem cells (NSC) before implantation could be one way to enable contact between the implant and the brain.

NSCs can go down various differentiation pathways. As demonstrated by Figure 25 below, NSCs first mature into common progenitors and then either towards glial or neuronal lineage. Glial progenitors may differentiate to glial cells, which are astrocytes and oligodendrocytes. Neural progenitors differentiate into different types of neurons, including dopaminergic neurons. [54]

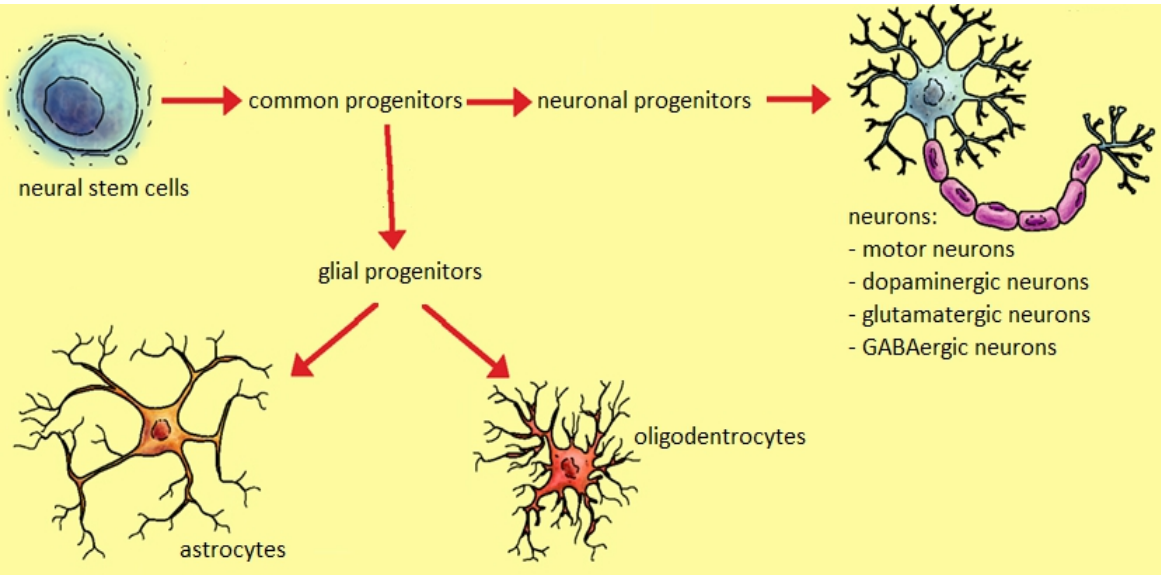

Figure 25. Differentiation pathways for NSCs. [54]

A large number of variables affect the differentiation path of a NSC. First, differentiation can be initiated and directed through chemical agents. Many of the common agents are growth factors (GF), but a variety of other differentiation factors also (DF) exist. Among others, fibroblast growth factors (FGF), NGF and epithelial growth factor (EGF) are commonly used used GFs in NSC differentiation into neuronal lineage [55-57]. There are also a large variety of DFs, which have been used to induce dopaminergic differentiation in NSCs. These include Trichostatin A (TSA), B-cell stimulatory factor 2, neurotrophic factors (NF), and leukaemia inhibitory factors among others [58-61].

Aside from chemical factors, neuronal differentiation has also been induced by surface mechanical and topographical features such as softness, micropillars, microgrooves and honeycomb structures [9, 62-64]. Additionally things such as electrical stimulation, surface coatings, hydrophilic effect, cell seeding density and carbon surface structure have been shown to play a role in the resulting differentiation pathway [9, 65-68].

NSC differentiation is typically studied by polymerase chain reaction (PCR) or immunofluorescence, using antibodies specific for different neural types of neural cells. Electron microscopy may also be used to qualitatively connect cell fate to surface topographic features. However, differentiation might lead to nonfunctional neurons. The only way to truly confirm the existence of firing neurons in the cell culture is to perform direct electrochemical measurement in the culture [9].

4.3 **Prior studies**

To date, differentiation of human NSCs (hNSC) in the presence of a DF has yielded maximally about 17 – 18% of dopaminergic neurons in entire populations of hNSCs, whereas without the application of DF only about 2% of the cells are showing dopaminergic properties. Some 3D microenvironments, such as polymeric microtowers and superhydrophobic micropillars, have been found to promote neuronal network formation. 3D peptide nanowire scaffolds have also boosted dopaminergic rodent stem cell differentiation. [9]

Some previous results on various cell cultures grown on Pyrolysed resist films are presented below. To date, no previous studies done with mouse NSCs could be found. Additionally, no previous studies done on NSC behaviour on an untreated SU-8 derived PyC could be found either. Some interesting results on the effect of surface topographic features on cell growth and differentiation are discussed in this Subchapter. The focus is solely on photoresist derived PyC materials because no studies on the biological response of the CVD PyC materials were available.

The studies made with hNSCs by Amato et al. [9] seem the most promising in regards to using SU-8 derived PyC to induce dopaminergic differentiation in NSCs. For all the results presented in their study, they had applied PLL treatment on their samples before seeding them with the cells. Therefore no results on the direct effect of the PyC surface on NSCs has been reported. More on the results of their study can be found in 4.3.2.

4.3.1 **SPR derived PyC film**

A PyC film was derived from SPR-220.7 photoresist by Zhou et al. [11] Human neuroblastoma (SK-N-MC) cells were found to exhibit good adhesion for plain untreated PyC surface. Within two days of coating, the samples were found to be completely coated with cells, with the initial culture concentration being 3×10^5 cells/ml. This was estimated to be a reasonably good growth rate of these cells on the carbon substrate.

After 1 to 4 days of seeding with rat adrenal gland pheochromocytoma (PC12) cells, Zhou et al. [11] found NGF injection to induce neurite outgrowth within 24 hours. The cellular adhesion to the substrate tended to weaken due to the growing tension in the neurite connecting the cells. However, the cells still remained on the substrate after 4 days, and they extended more than a hundred microns to reach other cells. Neurites that emerged on carbon were significantly lower than the neurite emerging on a coated glass. In conclusion, the surface was found to promote neuronal differentiation of PC12 cells after NGF treatment.

4.3.2 **SU-8 derived PyC film**

Amato et al. [9] found their material to induce spontaneous differentiation of hNSCs to dopaminergic neurons with a previously unseen efficiency in both 2D and 3D structures (Figure 26A). The effect was observed even in only the presence of GFs but without introducing DF. EGF + FGF was used for the GF treatment and glial cell line derived NF + dibutyryl cyclic adenosine monophosphate (cAMP) was used for the GF + DF treatment. The 3D material seemed to be the more efficient one in electrochemical detection and this was attributed to three factors. Firstly the structure provides mechanical support for the hNSC growth and differentiation, as the pillars serve as anchoring points for neurites. Secondly the PyC material itself enhances differentiation of hNSCs to dopaminergic neurons. Thirdly the 3D structure function as a neurotransmitter trap, enabling the detection of a larger fraction of the analyte. Amperometric measurements confirmed these neurons to be mature, as they were able to undergo repetitive depolarization, with each depolarization step leading to dopamine release.

The cultivation of hNSCs was performed on PLL coated and uncoated samples, some of which were O_2 plasma treated. The results indicated that the O_2 treated PyC with PLL coating was the most effective substrate for the cell culture viability, as it resulted in an uniform cell distribution and a well-defined morphology. The PLL adhesion on the PyC substrate appeared to be suboptimal but the oxygen functionalities after plasma treatment was suggested to improve physisorption of PLL.

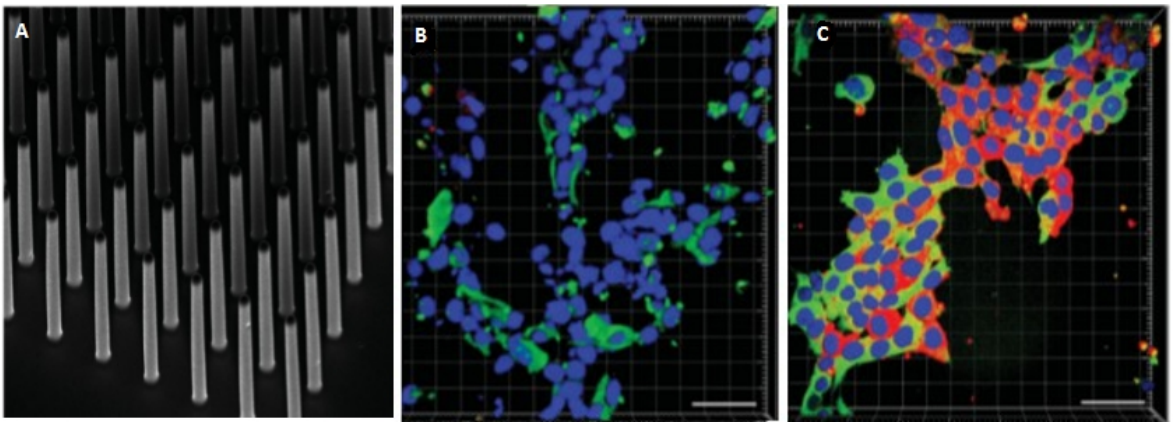

Figure 26. A) PyC micropillar structures. B-C) Fluorescence images on: B) PLL coated flat PyC, and C) O_2 plasma treated PLL coated flat PyC. TH seen as red in B) and C).[9]

Figure 26 B and C below show the immunofluorescence images for PLL coated flat PyC and O_2 plasma treated PLL coated flat PyC 48 h after seeding with the cells. Tyrosine hydroxylase (TH) specific for dopaminergic neurons can be seen as red. It is apparent that no dopaminergic differentiation has occurred on the non O_2 treated PyC.

Amato et al. [9] also performed electrochemical measurements on PyC surfaces with PC12 cells. Higher charges were detected on 3D carbon than on the flat carbon. This is likely because the 3D carbon serves as an efficient DA trap. The charge was also higher with growing rather than differentiating cells. This was attributed to the change in location from cell bodies to the neurite-like structures in the differentiating PC12 cells. 3D carbon was estimated to be suitable for detecting exocytotic events and discriminating biological differences between cell population, as well as providing more efficient detection of DA and possibly other analytes as well.

Another study by Mitra et al. [12] studied the behaviour of cells on a flat and patterned PyC. They found that on a flat substrate, mouse neuroblastoma (N2a) cells extended neurites in all directions quasi-equally, guided solely by chemical cues. In the presence of cAMP, they adapted predominantly polarized neuronal cell morphology and extended neurites along the axis of the underlying carbon film.

On the patterned surface, the cells would best orient along the microstrips of a width in the range of their own. This occurred both in the presence of, and without cAMP. In the presence of cAMP, the cells extended neurites along the pattern edges and their polarity and alignment was influenced by neighbouring cell density and the pattern dimensions. Narrower channel dimensions resulted in longer neurites with better alignment. With increasing strip width, the alignment was disrupted and neurites started to grow perpendicular to the channel direction. These effects are visible in Figure 27 which shows N2a growth on 10 µm and 20 µm microstrips.

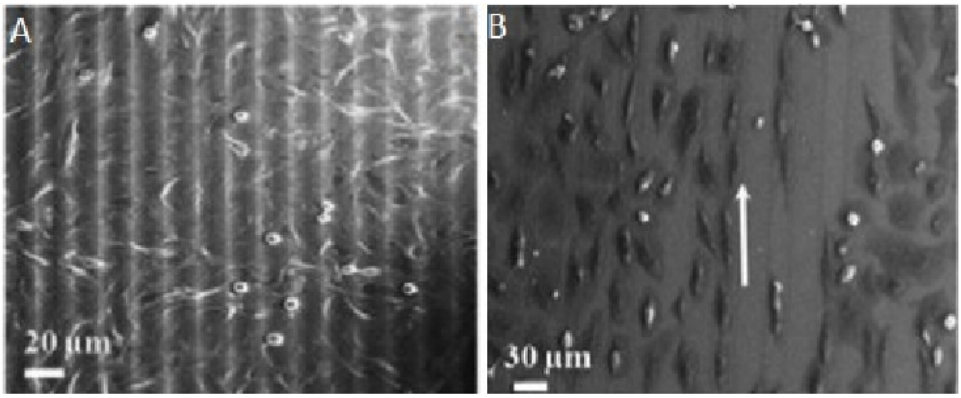

Figure 27. N2a cells cultured on A)10 µm microstrips, 10 µm apart. B) 20 µm microstrips, 30 µm apart. [12]

The viability of the cells was shown to increase with incubation time for all substrates. The viability was better on the control sample up to 4 days after cultivation. After that, a major shoot up in viability could be observed on PyC with both N2a and rat glial Schwann cells. This is an indication that the cultured cells proliferate on the substrates in the same manner as other eukaryotic cells proliferate on other biocompatible substrates.

Mitra et al. [12] also performed an in vitro study of neural cell cytotoxicity on SU-8 micropatterned substrate. Schwann cells were found to be more adaptive towards topographic cues than the undifferentiated N2a cells were. Nevertheless, they both demonstrated oriented growth along microtracks and grooves of 15 – 30 µm in diameter. 15 µm grooves resulted in best orientation. The patterns guided the Schwann cells even up to dimensions of 75 µm. The neurite length and alignment as well as neurites per cells were both dependent on the pattern dimensions.

N2a cells were directed into neuronal lineage in the presence of cAMP. The differentiated N2a cells exhibited distinct neurite alignment along the edges of the micropattern. The neurite outgrowth was also found to be significant along the edges of wide circular and square patterns and in the grooves in between them.

All in all, not much prior studies have been done of the neural biocompatibility of photoresist derived PyC films. Dopaminergic differentiation of of NSC has been confirmed on SU-8-based PyC on a prior occasion and topographic cues have been utilized to direct cell growth. The advantageous and easy topographic fabrication has been utilized to affect the cellular response on these materials. There is no reason to suspect any cytotoxic effect of the surface. Various effects of the surface and chemical treatments, as well as the effects of untreated surfaces are collected in Table 6.

Table 6. The effects of surface modifications and growth on SU-8 pyrolysed carbon on various cell lines.

Cell line	PyC precursor	Treatment	Detected effects
SK-N-MC	SPR-220.7	Untreated	Good adhesion and cell viability
PC12	SPR-220.7	NGF	Neurite outgrowth, weakening of cellular adhesion
hNSC	SU-8	O_2 plasma + PLL + EGF + FGF	Increased cell viability Induced dopaminergic differentiation
hNSC	SU-8	Pillar structures	Improved DA detection and providing mechanical growth for hNSC growth and differentiation.
PC12	SU-8	Pillar structures	Improved DA detection
N2a	SU-8	Microstrips	Directed neurite growth and improved viability after 4 days of cultivation, neuronal differentiation
N2a	SU-8	cAMP	Inducing neuronal cell morphology
Schwann	SU-8	Microstrips	Highly oriented growth and improved viability after 4 days of cultivation

5 Purpose of this work

The aim of this work is to assess and improve the properties of SU-8 derived PyC for the purpose of in vivo electrochemical detection of DA. In the experimental section, basic structural characterization of the material is done using Raman spectroscopy and AFM. In the electrochemical section, the potential window of the material is determined in PBS, H_2SO_4 and cell culture media. Then, the outer sphere redox behaviour is studied using ferrocenemethanol probe. Finally, the electrochemical response of the material to DA and AA is measured. The biological response to neural tissue is studied with mouse NSC cultures. MTT is used to measure cell viability after seeding. Cell differentiation fate is studied with immunofluorescent imaging. Surface treatments, including plasma treatments, coatings, electrochemical and chemical treatments are used in attempt to improve the film adhesion to the substrate, as well as electrical performance and biological response. The overall structure of the experimental section can be seen in the flowchart below (Figure 28).

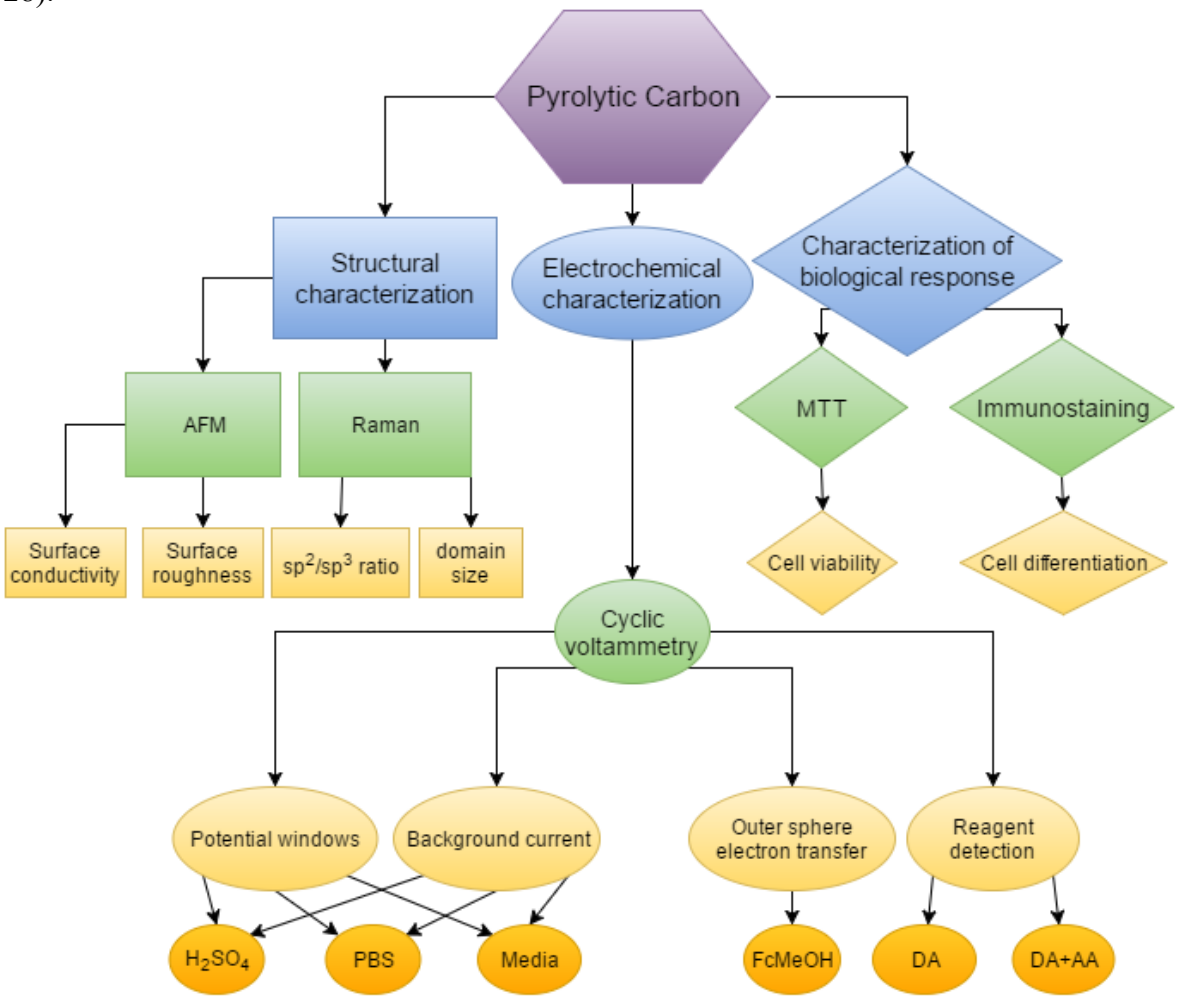

Figure 28. Flowchart of the experimental Section. Characterization of SU-8 derived PyC (purple). Divided into three categories; structural, electrochemical and bio-response characterization (blue). Characterization methods in green, various properties in yellow, and electrochemical reagents and electrolytes in orange.

6 Materials and methods

The experimental section of this thesis work consists electrochemical and biological characterization of SU-8 derived PyC. In the electrochemical section, CV was used to define potential windows, electron transfer properties and DA detection properties of the PyC films. In the biological section mouse NSCs (NeuroE) were seeded on the films, and their viability and differentiation was studied. Prior to these, some important surface characterizations were done with AFM and Raman spectroscopy.

6.1 Electrode preparation

As the adhesion of SU-8 derived PyC films is known to be poor because of the extreme shrinking occurring during the pyrolysation process [23], silicon wafers were treated with either hydrofluoric acid (HF) or O_2 plasma before spin coating the wafers with the resist, in order to improve film adhesion. HF treatment could improve the resistivity by removing the native oxide from the silicon and cleaning the surface. This will result in a hydrophobic surface, to which SU-8 should adhere better. O_2 treatment might improve the adhesion by increasing the surface energy and wettability of the surface through roughening. The HF treatment was done by dipping the wafer in H_2O:HF 10:1 solution for 1 minute. The O_2 plasma treatment was performed with Tepla 400 microwave plasma system, for 1 minute, with 800 sccm oxygen flow and 800 W. Spin coating with SU-8 was done with 9000 rpm for 45 seconds, to result in 10 µm thick layer. A BLE photoresist spinner was utilized.

The spun resist was soft baked on a hot plate at up to 85 °C, cooled down to room temperature (RT), exposed to UV light for 8 seconds (flood exposure), and post-baked on a hot plate at up to 95 °C. After post-baking and cooling in RT, the wafer was diced into 1 cm x 1 cm pieces and washed with distilled water (DI-W). The wafer was dried carefully, first by cleanroom paper, and then at 50 °C for 15 minutes. The dicing was done with a Loadpoint Microace series 3 dicing saw, while the wafer was attached to a plastic ring holder with adhesive bluetape. A 150 µm diamond blade was used with 15 000 rpm in a constant DI-W flow and a feed rate of about 7 mm/s.

Film pyrolysation was done in a tube furnace, at temperatures of 600 °C, 800 °C, 900°C and 1000 °C. Pyrolysation was carried out in continuous nitrogen flow, and the samples were slowly ramped to the final temperature, held there either for 1 or 4 hours, and then cooled down to RT. Cooling down was done slowly in order to avoid film delamination by thermal stresses. Flushing in nitrogen flow was performed three times in >1 bar pressure.

The resulting PyC films had various configurations, from HF or O_2 plasma pretreated at temperatures between 600 °C and 1000 °C, for 1 or 4 hours of pyrolysation time. Additionally some of the samples were post-treated with oxygen plasma before doing the measurements. This was done in order to improve the biocompatibility and possibly the electrochemical performance of the film [9, 51]. The same equipment was used for the O_2 plasma as before, but an oxygen flow of 600 sccm was used instead.

For electrochemical measurements, the samples were fabricated into electrodes (d = 3 mm). They were attached to copper conductors using teflon tape (irpola), with a hole over the PyC film. Conductivity between the silicon and copper was ensured by first roughening the silicon side by scratching mechanically, and then scratching copper on the silicon side of the sample before doing the attachment to the carrier copper slip.

For the cell seeding, the samples were first sterilized with 80% ethanol, dried, and then some of the samples were coated with 15 µg/ml Poly-L-lysine hydrobromide (Sigma-Aldrich P9155) in cell culture water (EMD Millipore, H20CC0501) for 5 minutes and washed with PBS (Biochrom, L1825) three times before seeding. This was done both for viability and differentiation studies.

6.2 **Raman spectrometry and AFM**

Raman spectrum was measured with WITec Alpha 300 RA, using 532 nm laser. Line length of 3 mm, with 50 points in line, 10 accumulations per point and 0.5 second integration time was used. OriginLab data analysis software was used to analyze the results. The Raman curves were fitted with Lorentzian curves.

AFM was performed using Ntegra Aura AFM (NT-MDT). Both surface conductivity (DCP10 or HA_HP_DCP, NT-MDT probe used) and topography were measured. Measurements were done in contact regime, using a tip of about 100 nm curvature radius.

6.3 **Cyclic voltammetry**

CV measurements were carried out with Gamry instruments Reference 600™ potentiostat, with cycling speeds of 10 mV/s, 50 mV/s, 400 mV/s and 500 mV/s. All of the electrolytes and solvents for redox analytes were argonated for 20 minutes beforehand, with the exception of cell culture media. All measurements were made against a standard Ag/AgCl ref. electrode (Radiometer analyticals, XR300), except in media, where a Ag/AgCl pseudo electrode was used. The electrode was fabricated from silver wire, submerging it in 3 mol/l KCl solution (Radiometer Analyticals, C20C310) for 30 min. PBS used in the CV measurements consisted of 8 g/l NaCl (Merck, 1.06404.1000), 0.2 g/l KCl (Merck, 1.04936.0500), 1.44 g/l Na_2HPO_4 (Merck, 1.06586.0500) and 0.24 g/l KH_2PO_4 (Merck, 1.04873) in DI-W, and had a pH of about 7.4. The resistance between the reference electrode and the working electrode (Ru) was measured for most electrode types.

Potential windows were measured in 0.15 M H_2SO_4 (Merck, 1.00731.1011), PBS and Biowest MEM (L0415-500) cell culture media. 0.15 M Ferrocenemethanol (Sigma-Aldrich 335061-5G) in 0.15 M H_2SO_4 (Merck, 1.00731.1011). was used as an outer sphere redox probe in order to characterize the bulk electrode kinetics. DA and AA were measured diluted either in PBS or Media. Dopamine hydrochloride (Sigma-Aldrich, H8502-25G) and L-ascorbic acid (Sigma-Aldrich, A5960-25G) were used. DA was measured in concentrations of 100 nM, 250 nM, 500 nM, 750 nM, 1 µM, 2.5 µM, 5 µM, 10 µM, 25 µM, 50 µM and 100 µM. AA concentration of 1 mM was used.

6.4 **Cell culture**

Mouse neural stem cell line NE-GFP-4C (NeuroE, ATCC®, CRL-2926™) was utilized in all of the biocompatibility studies. The cultivation of the cell line was done according to ATCC® subculture instructions. Biowest MEM (L0415-500) cell culture media was used for cells. The media was supplemented with fetal bovine serum (FBS, Thermo Fisher, 10270-106, final concentration of 10%), L-glutamine (gibco®, 25030-081, final concentration of 2 mM) and penicillin (HyClone™, SV30010, final concentration of 1%). When seeding the cells on the samples, and seeding density of 2-4x10^4 cells/cm^2 was used for the cells during the MTT protocol and this cell density was also maintained in the cell culture during each subculture. A lower seeding density was used in the differentiation studies.

6.5 **Viability**

Colorimetric evaluation of cell viability was done with thiazolyl blue tetrazolium (MTT) protocol 1 to 2 days after seeding the samples with NeuroE cells. BMG LABTECH FLUOstar Optima microplate reader was used to analyse the samples. 0.5 mg/ml MTT (Sigma-Aldrich, M5655-1G) in appropriate complete cell culture media was used to form formazan crystals on viable cells. The MTT was syringe filtered with a 0.2 µm sterile polyethersulfone syringe filter before use (VWR, 514-0073). The samples were transferred to new wells before the addition of the MTT solution. Incubation in MTT was done for 2 to 3 hours. After incubation, the MTT solution was removed, and 0.5 ml 2-propanol VLSI Pluranal® (IPA, Honeywell, 10188910) with 0.04 M HCl (Merck, 109057) was used per sample to dilute the crystals. The dilution was mixed well and moved to new wells for colorimetric analysis. Blank controls were included in the measurements, and 570 nm wavelength was used for the MTT reaction, while 630 nm wavelength was used as a control wavelength. MTT was done on PyC samples with and without PLL coating. ISO 10993-5:2009(E) standard [69] was used to calculate the cell viability as % of a control sample, for each sample type. The MTT protocol was performed always for n = 3 samples for each sample type, and the viability value was calculated as an average of the three samples.

MTT assay results were qualitatively confirmed by F-actin fluorescent dye and imaging of NeuroE cells grown on samples with and without PLL coating. The cells were first fixed with 4% paraformaldehyde (PFA, Alfa Aesar, 30525-89-4) in PBS for 10 minutes. Permeabilization of the cells was then done with 0.5% Triton-X-100 (Merck, 9036-19-5) in PBS for 10 minutes. 5% Phalloidin-568 (Biotium, CF568) in PBS was used to stain the cells for 20 minutes, protected from light. Lastly the cell nuclei were stained and the samples were mounted on glass coverslips using Vectashield mounting medium with DAPI (Mediq, H-1200). The samples were washed three times with PBS was in between each step. Olympus BX51M microscope and Leica DCF420 digital microscope camera were used for the imaging.

6.6 **Cell differentiation**

NSC fate on the PyC samples was studied, using NeuroE mouse NSCs (p7). Two sample types were used: 1 h 900 °C PyC on HF treated Si, with and without O_2 plasma treatment of the pyrolysed surface. The samples were transferred to 24 well plates. Before seeding, the samples were washed with 80% ethanol, and some of the samples were PLL coated. A seeding density of ~ 5000 cells/cm^2 was used.

The cells were allowed to grow on the samples for 24 h. After 24 h, 20 ng/ml bFGF (Sigma-Aldrich, F0291) was applied on a third of the samples, and 20 ng/ml bFGF + 1 ng/ml TSA (Sigma-Aldrich, T8552) were applied on another third. A third of the cells were left untreated. Medium, basic fibroblast growth factor (bFGF) and DF (TSA) were renewed every 2 days. 3 data points were collected: 3, 6 and 9 days after applying the drugs.

Immunofluorescent staining and imaging was performed to evaluate the differentiation pathways of the cells. 1:500 anti-tyrosine hydroxylase antibody (Sigma-Aldrich, AB152) was used as a dopaminergic marker. 1:200 anti-neuron specific enolase antibody (NSE, Thermo Fisher, PA1-46203) was used as a neuronal marker. 1:200 nestin antibody (Thermo Fisher, PA5-11887) was used as a marker for neuronal progenitors. 1:200 rabbit IgG whole molecule control (Thermo Fisher, 31235) was used as a negative control. 1:500 goat anti-Rabbit IgG (H+L), Alexa Fluor® 568 conjugate, was used as the secondary antibody (Thermo Fisher, A-11011). The antibodies were diluted in 0.1% Bovine Serum Albumin (BSA, Biowest, A0296-100) in PBS. The proper functioning of the staining protocol with these concentrations was confirmed beforehand with NeuroE cells grown on glass coverslips.

For staining, the cells were fixed with 4% PFA in PBS for 20 minutes. They were then permeabilized with 0.5% Triton X-100 in PBS for 10 minutes. A dilution of 90% (0.1% BSA in PBS) + 10% Goat normal serum (GS, Sigma-Aldrich, G9023) was used to block the cells for 30 minutes. The cells were then stained with the primary antibodies for 1 h at RT, and likewise with the secondary antibody for 1 h at RT. During the staining, the samples were protected from light. Finally the samples were mounted to glass coverslips using Vectashield mounting medium with DAPI. In between each step, the cells were washed with three times using PBS. Olympus BX51M microscope and Leica DCF420 digital microscope camera were used for the imaging.

7 Results and discussion

The results from the experimental set-ups are presented in this Chapter. First structural characterizations done with AFM and Raman spectroscopy will be presented in Subchapter 7.1. Then, some of the electrochemical properties of PyC will be evaluated in Subchapter 7.2. Finally, cellular viability and differentiation pathways on the material will be assessed in Subchapter 7.3. It should be noted that most of the results in this thesis work are only preliminary and have not been repeated at this time. Because of this, only some general conclusions should be drawn from them, and they should not be considered absolute.

7.1 Structural properties

AFM

Figure 29 shows AFM measurement done on the surface of a 800 °C PyC sample, fabricated on a HF treated Si substrate. Figure 29A shows the topographic image of the surface. The topographical features are mostly just a few nm in size, although at highest, they are over 10 nm in height. RMS roughness value of all data points was calculated to be 9.8 Å. This includes the untypically high feature present in the upper half of 29A. If this feature is disregarded from the rms calculation, a value of 7.9 Å is received. Amato et al. [9], as they showed all features for their SU-8 derived PyC to be below 5 nm, and a RMS roughness 2.1 Å. McEvoy et al. [1] also showed a sub nm feature size. While even the lower value here is almost four times that of Amato et al. [9], the film is still smooth on nanoscale.

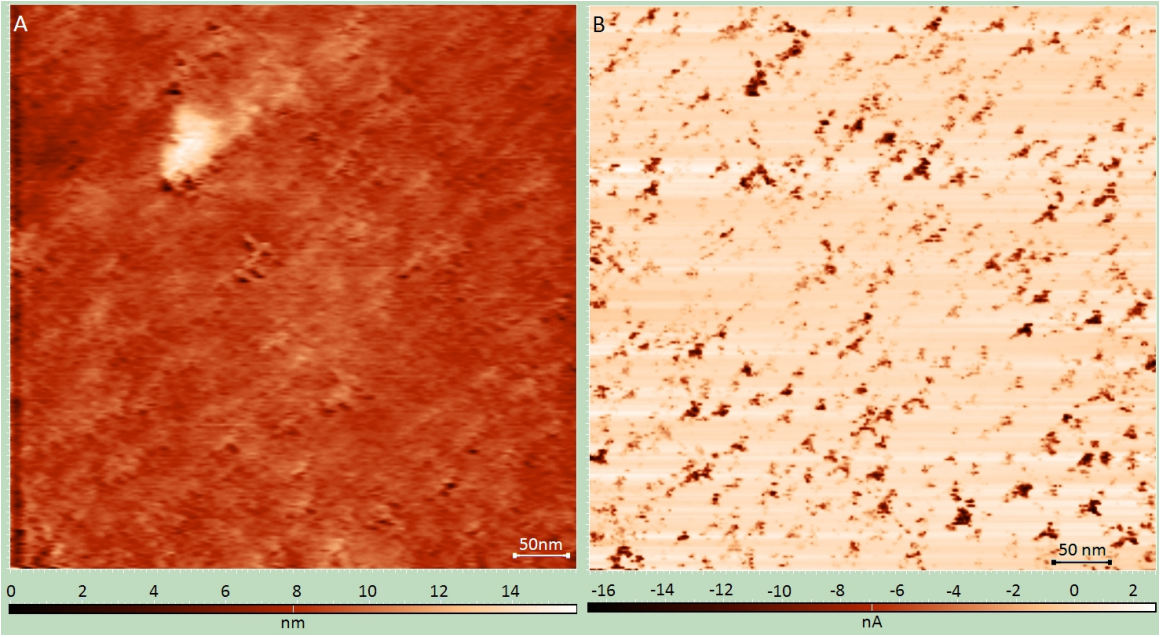

Figure 29. AFM images for A) surface topography and B) surface conductivity of 800 °C PyC on HF Si.

Figure 29B shows the surface conductivity done by AFM. The film is mostly quite evenly conductive, excluding the evenly spaced reverse conductive spots on the surface. These spots seem to somewhat correspond to the topographical lowest features on 29A, and could correspond to pore-like features on the surface. The absolute conductivity values in these locations is much higher than the average conductivity on the smooth area (which is roughly about 1 nA).

Raman

Figure 30 shows a Raman curve of a SU-8 PyC film, baked at 900 °C for 1 hour. The peak ratio I_D/I_G was calculated to be about 3.3, which is extremely high, indicating both a high sp^2 content, and a high degree of disorder. The spectrum is similar to the Raman spectra measured with other PyC materials, presented in Chapter 2. It exhibits a narrow G peak at 1600 cm^{-1}, and a wider and more prominent D band. The 2D can also be seen clearly. Compared to the other PyC Ramans presented, the main difference in this Raman spectrum is the D band, which is much more prominent, and notably wider than the G peak.

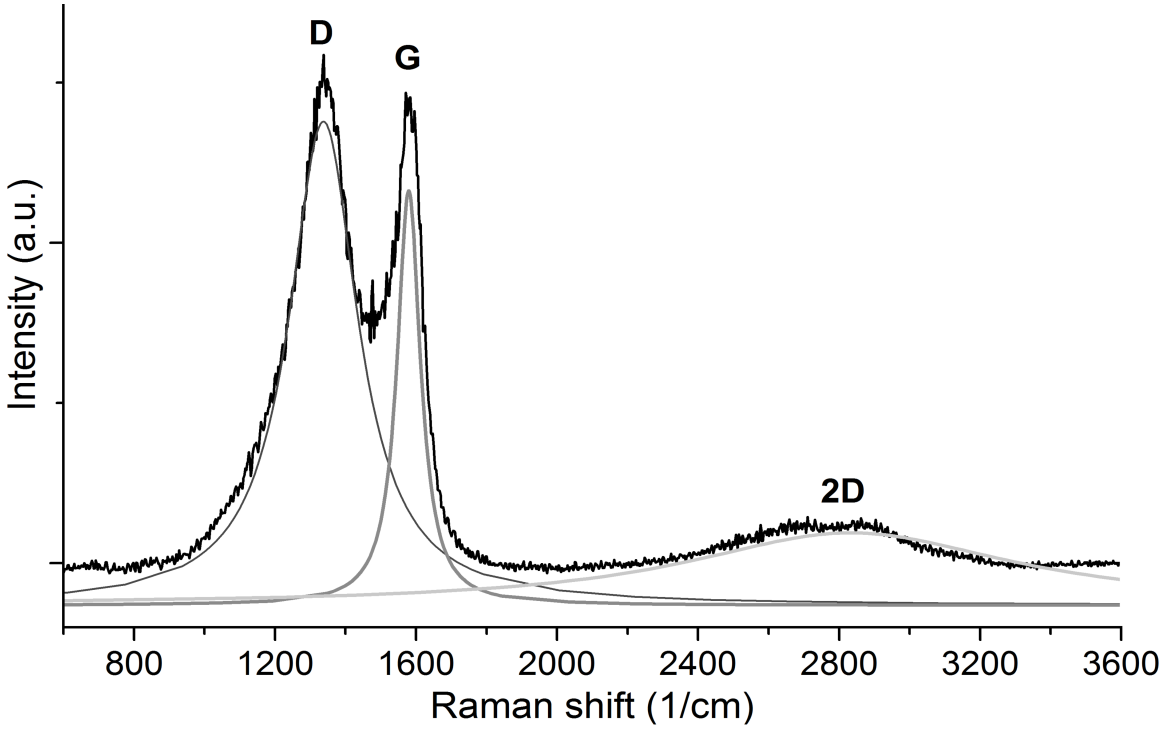

Figure 30. Raman spectrum for a 900 °C 1h PyC film. The curves in the Figure shows lawrencian fittings for D, G and 2D peaks.

The Raman spectrum is indicative of a nanocrystalline graphitic carbon material. The crystallite size L_a was calculated to be about 5.8 nm, using equation 2. According to the model by Ferrari and Robertson, The surface has extremely high content of sp^2 hybridized carbon atoms, with no (or only a little) sp^3 hybridized atoms in between the graphitic crystallites. The film has been fabricated in high temperatures, so there is some uncertainty in estimating the sp^2/sp^3 ratio from the D and G band intensity ratios. More reliable estimations of the ratio could be achieved with XPS, EELS or UV-Raman for example.

7.2 **Electrochemical properties**

In this section, the results from electrochemical measurements are presented. The measurements were performed for a variety of SU-8-based PyC electrodes. The fabrication temperature was maintained for 1 or 4 hours. The temperatures used, were 600 °C, 800 °C and 900 °C. Most of the results in this sections are acquired via 900 °C PyC electrodes, as it was found to be superior in many aspects, as will be demonstrated later in this Subchapter.

1000 °C electrodes were also fabricated, but they delaminated during electrode fabrication and chemical treatments, and thus were not used in the measurements. Other delamination problems also occurred, and they will be mentioned in the relevant sections. To avoid delamination, two fabrication substrates were tested; HF treated silicon and O_2 plasma treated silicon. Between the two, HF treatment resulted in better adhesion of the two, so it was used in most of the experiments.

Anodization at 1.7 V and O_2 plasma treatment of the PyC layer were performed to improve electrode performance [1, 3, 5, 9]. 10 mV/s, 50 mV/s, 400 mV/s and 500 mV/s scanning rates were used. 50 mV/s was the standard speed used. The electrodes used in this work can be divided in 10 types, which are listed in Table 7. Post-fabrication O_2 plasma treatment also resulted in some adhesion problems, but to a manageable extent.

Table 7. Different working electrode types used in the electrochemical measurements.

Electrode type	Fabrication temperature (°C)	Thermal treatment time (h)	Fabrication substrate	Post-deposition treatment
6001hHF	600	1	HF Si	-
6001hO2	600	1	O_2 plasma Si	-
8001hHF	800	1	HF Si	-
8001hO2	800	1	O_2 plasma Si	-
9001hHF	900	1	HF	-
9001hO2	900	1	O_2 plasma Si	
9004hHF	900	4	HF	-
9001hHF+	900	1	HF	O_2 plasma
9004hHF+	900	4	HF	O_2 plasma
9001hHFA	900	1	HF	Anodization

Potential windows measured in sulphuric acid, PBS and cell culture media are presented in Section 7.2.1. In the subsequent Section (7.2.2), the outer sphere redox system performance of PyC is evaluated using FcMeOH. In the final Section (7.2.3) of this Subchapter, the measurements in DA and DA+AA solutions will be presented. Finally the performance of these electrodes for this purpose will be evaluated.

The potential window upper and lower limits were defined at the points in which background current absolute value goes beyond 0.2 µA. This was of course only done, when the background current at the stable part was below this value. There were significant changes, however in the background current with different electrode types and electrolytes.

7.2.1 **Potential windows**

Sulphuric acid

The potential windows in sulphuric acid (H_2SO_4) were first measured for 6001hHF, 6001hO2, 8001hHF and 8001hO2 electrodes (Figure 31), using a cycling speed of 50 mV/s. The widest potential window with the lowest background current was observed with the 6001hO2 electrode. It showed a potential window of 1.8 V, ranging from -0.6 V to 1.2 V against the reference electrode, and a background current of about 7,1 nA/cm^2. The rest of the samples all showed a potential windows from 1.3 V to 1.4 V, and background currents of about 14,1 nA/cm^2. Preparation at 600 °C seems to have widened the potential window in low voltages, while the O_2 treatment of the substrate seems to have done the same in higher voltages.

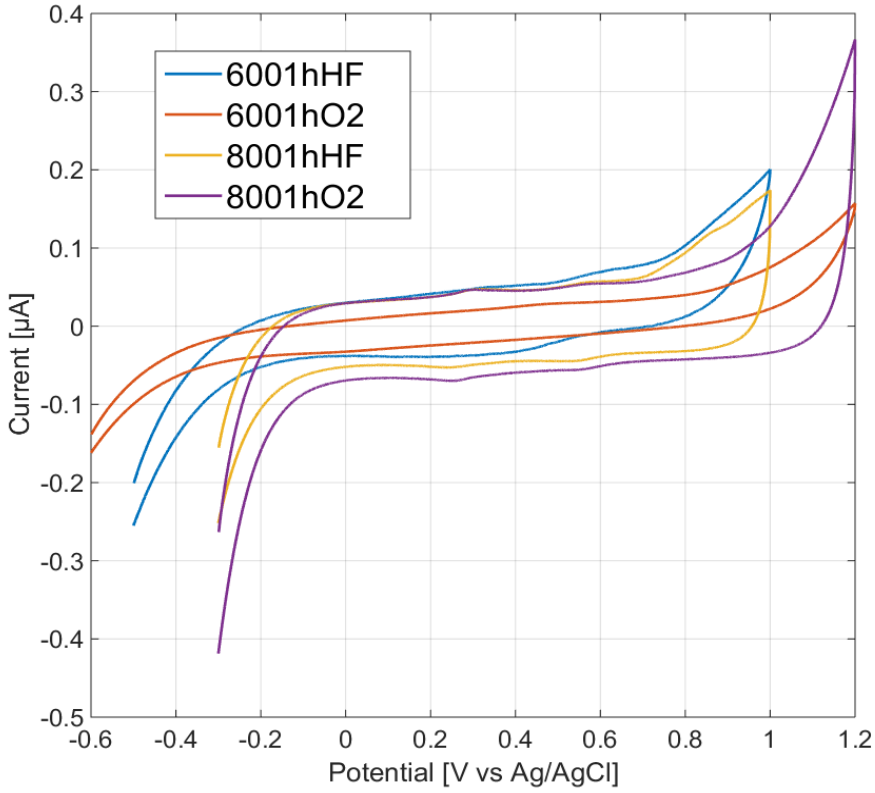

Figure 31. Potential windows of electrode types 6001hHF (blue), 6001hO2 (orange), 8001hHF (yellow) and 8001hO2 (purple) in 0.15 µM H_2SO_4.

All in all, none of the differences between the potential windows are substantial. The rise in temperature from 600 °C to 800 °C has been shown to increase the film conductivity and decrease the roughness [32], and the plasma treatment is also likely to increase the surface roughness. The film fabricated in lower temperatures might also have a higher content of sp^3 hybridization on the surface. It is possible that the overall higher film resistivity keeps the current from rising as fast with the lower fabrication temperature samples. A more thorough characterization of the surfaces would be needed to properly hypothesize about the differences seen here between the O_2 and HF samples.

All of the curves show slight characteristic faradaic peaks. Oxidation peaks for 6001hHF are located at 0.33 V and 0.64 V, for 6001hO2 at 0.45 V, for 8001hHF at 0.3 V, 0.56 V and 0.85 V, and for 8001hO2 at 0.3 V and 0.56 V against the reference electrode. It is somewhat peculiar that the 800 °C samples show a higher amount of these peaks, as surface oxide functionalities (a common cause for such peaks) should decrease with increased fabrication temperature. Ru values were measured to be around 400 Ω for 6001hHF, 2100 Ω for 6001hO2, 40 Ω for 8001hHF, and 500 Ω for 8001hO2 electrode.

900 °C electrodes show a very similar performance in H_2SO_4 compared to those fabricated in lower temperatures. As shown in Figure 32 (red and green lines), these electrodes show similar background currents as those in Figure 31, as well as potential windows of about 1.5 V. There is not much difference in the behaviour of the electrode fabricated for 1 hours in comparison to that fabricated for 4 hours, but the 4h electrode showed improved adhesion to the substrate.

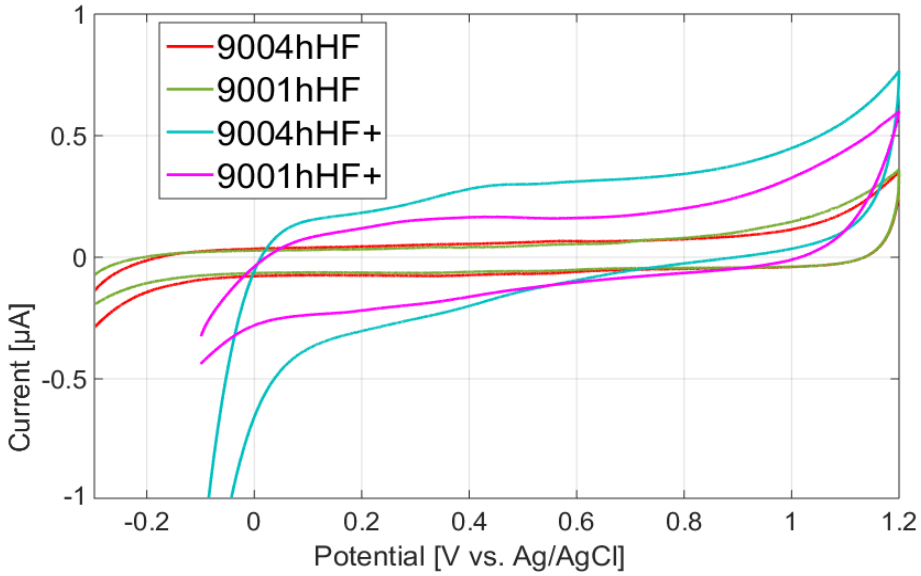

Figure 32. PyC 9001hHF (green), 9004hHF (red), 9001hHF+ (magenta) and 9004hHF+ (cyan) electrodes in 0.15 µM H_2SO_4.

Cyan and magenta lines show the potential windows for 9001hHF+ and 9004hHF+ electrodes respectively. Post-pyrolysation O_2 plasma treatment increases the background current, especially for the 9004hHF+ electrode, and shortens the potential window especially in the low voltages, resulting in a potential window of about 1.2 V for 9004hHF+ and 1.3V fir 9001hHF+.

The curves also show faradaic peaks, albeit they are barely visible in the untreated samples. All of the samples show two oxidation peaks against the reference electrode. The peaks are located at 0.35 V and 0.56 V for the 9001hHF sample, 0.36 V and 0.57 V for the 9004hHF sample, 0.3 V and 0.44 V for the 9001hHF+ sample and 0.44 V and 0.6 V for the 9004hHF+ sample. One of these peaks can likely be attributed to the increase in quinone-like functional groups on the electrode surface, but the origin for the rest requires additional characterization. Ru values below 6000 Ω were measured for all 9001hHF, below 2000 Ω for all 9004hHF, below 7500 Ω for all 9001hHF+, and below 6000 for all 9004hHF+ electrodes.

The effect of cycling speed on the potential windows can be seen in Figure 33. For 9004hHF electrodes, the increase in current is relatively small from 10 mV/s to 50 mV/s increase in speed. It is almost 141.5 nA/cm^2 when increased to 500 mV/s. and shows an oxidation peak at about 0.6 V against the reference electrode. The faradaic peaks also get more dominant with increasing scanning speed.

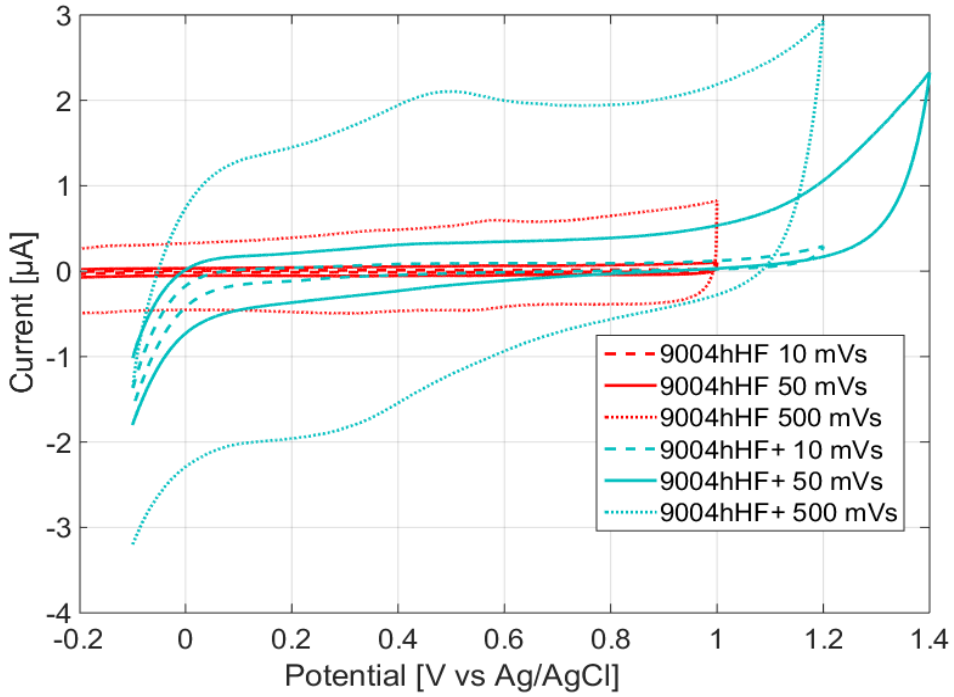

Figure 33. The effect of cycling speed in the H2SO4 potential windows. Cyan curves show 9004hHF+ electrodes, while red curves show 9004hHF electrodes. Dashed curves show potential window with 10 mV/s scanning speed. Dotted curves show potential windows for 500 mV/s speed, and finally solid curves show the potential windows for 50 mV/s speed.

For the 9004hHF+ electrodes, the effect is much larger. The background current triples when increasing the cycling speed from 10 mV/s (dashed line) to 50 mV/s (solid line). It increases to above 424.4 nA/cm^2 when increasing the speed to 500 mV/s. The oxidation and reduction peaks forming around 0.5 V and 0.3 V (against the reference electrode) respectively become clearly visible, although while at lower cycling speeds two peaks could be seen, now only one is visible. The effect of cycling speed was not characterized in any of the previous work done on PyC materials, presented in Chapter 3.

PBS

Figure 34 shows stable potential windows of 0.5 V against the reference electrode for 9001hHF and 9001hO2 electrodes in PBS. Wider potential window could still be used (from about -0.3 V to about 0.7 V), as the current change in both ends of the window are not yet substantial. The two electrode types show extremely similar potential windows with a background current of about 7.1 nA/cm^2 before and 5.7 nA/cm^2 after potential cycling.

The background currents in Figure 34 are extremely low for a carbon material, and alike to those measured previously on various PyC materials (Chapter 3). The 9001hHF electrode seems to be slightly better due to the lower background current. It was also superior in terms of film adhesion, as the 9001hO2 electrode films were prone to delamination. A faradaic oxidation peak is visible for both samples at 0.17 V against the reference electrode before potential cycling.

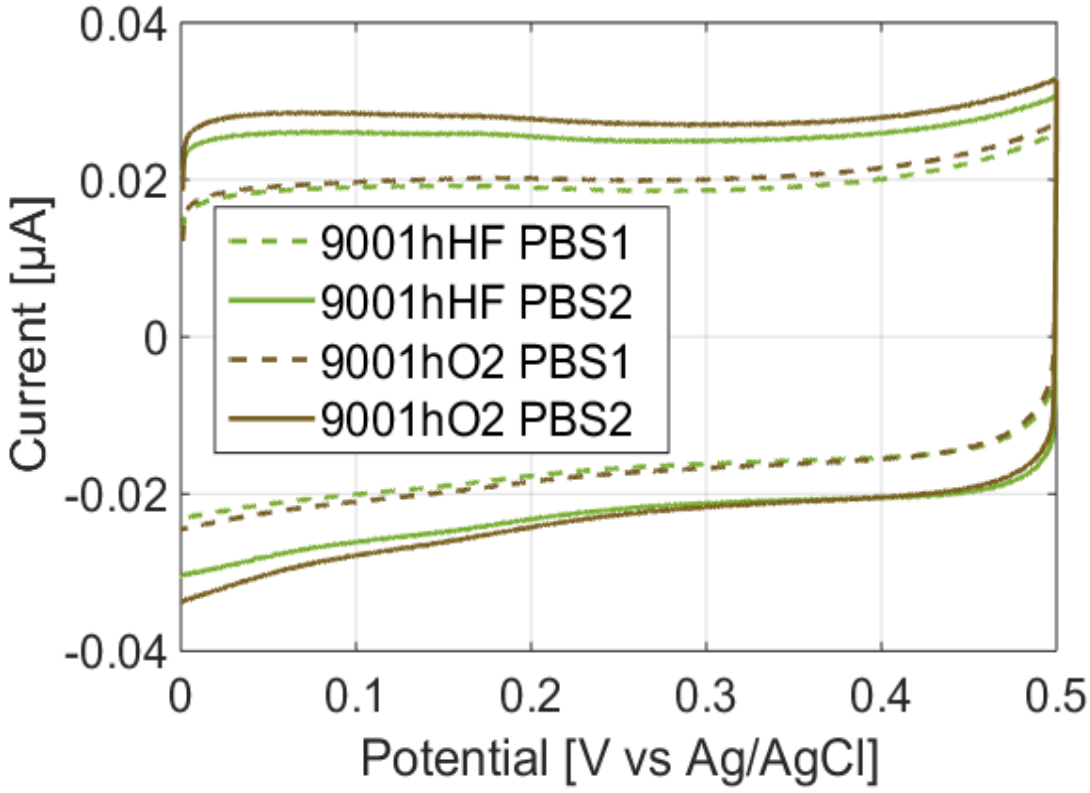

Figure 34. Potential windows of 9001hHF (green) and 9001hO2 (brown) in PBS. Measurements are done before (solid lines) and after (dashed lines) 10 potential cycles.

PBS potential windows for 9004hHF and 9004hHF+ electrodes can be seen in Figure 35. The potential window for the treated electrode is about 0.8 V, ranging from -0.2 V to 0.6 V against the reference electrode. It is much wider for the untreated electrode, as it reaches below -0.3 V and well above 0.6 V. The background current is also much higher (14.1 nA/cm^2-21.2 nA/cm^2) for the 9004hHF+ electrode than for the 9004hHF electrode (~7.1 nA/cm^2).

The effects are alike to those seen in H_2SO_4 (Figure 32). However, in PBS no clear oxidation-reduction pairs become apparent in the 9004hHF+ electrode as they did in sulphuric acid. This would be likely for peaks caused by surface quinones as those become visible in acidic electrolytes. Increasing surface oxygen content has also been suggested to be linked to the visibility of quinone peaks on highly oriented pyrolytic graphite and that effect might be replicated here [28]. The curves show faradaic oxidation peaks at -30 mV and 0.18 V against the reference electrode for 9004hHF+ electrode and 58 mV and 0.31 V for the untreated electrode.

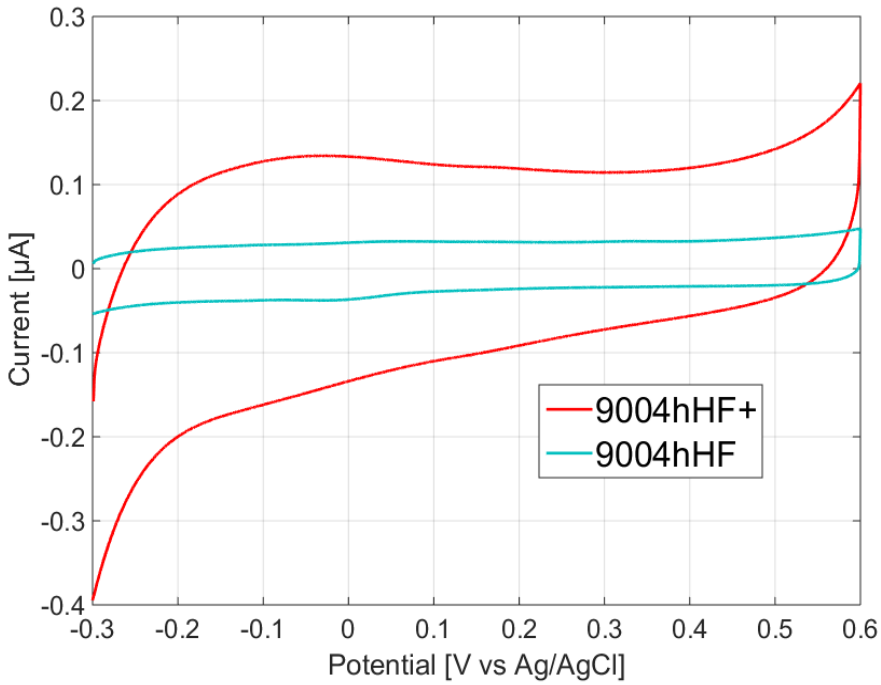

Figure 35. Potential windows for 9004hHF (cyan) and 9004hHF+ (red) in PBS.

Cell culture media

To model the behaviour of the electrodes in a complex environment, the electrochemical response of the electrodes was measured in a cell culture media (Biowest, L0415), which contains essential nutrients for cell growth. These nutrients are as follows; Calcium chloride dihydrate, magnesium sulfate anhydrous, potassium chloride, sodium chloride, sodium phosphate monobasic anhydrous, D-glucose anhydrous, L-arginine monohydrochloride, L-glutamine, L-isoleucine, L-leucine, L-lysine monohydrochloride, L-tyrosine disodium salt dihydrate, sodium bicarbonate and 17 others in quantities from 0.1 mg/l (riboflavin) to 6.8 g/l (sodium chloride).

Figure 36A shows potential windows for 9001hHF and 9004hHF electrodes in media. They range from around -0.1 V to around 0.8 V against the pseudo reference, being in the same range as the potential windows measured in PBS. The background current is also in the same range of about 7.1 nA/cm^2. There is not much difference between the two electrode types.

Figure 36B shows also the 9004hHF+ electrode response in the cell culture media. Unlike the untreated electrodes, faradaic peaks can be seen on the treated electrode and there is no stable potential window. Due to the irregular shapes of these curves, there are likely to be various oxidizing and reducing agents within the media and the sharp oxidation peak shape indicates reactions controlled by adsorption. A dominant oxidation peak is located just below 0.4 V against the pseudo reference electrode.

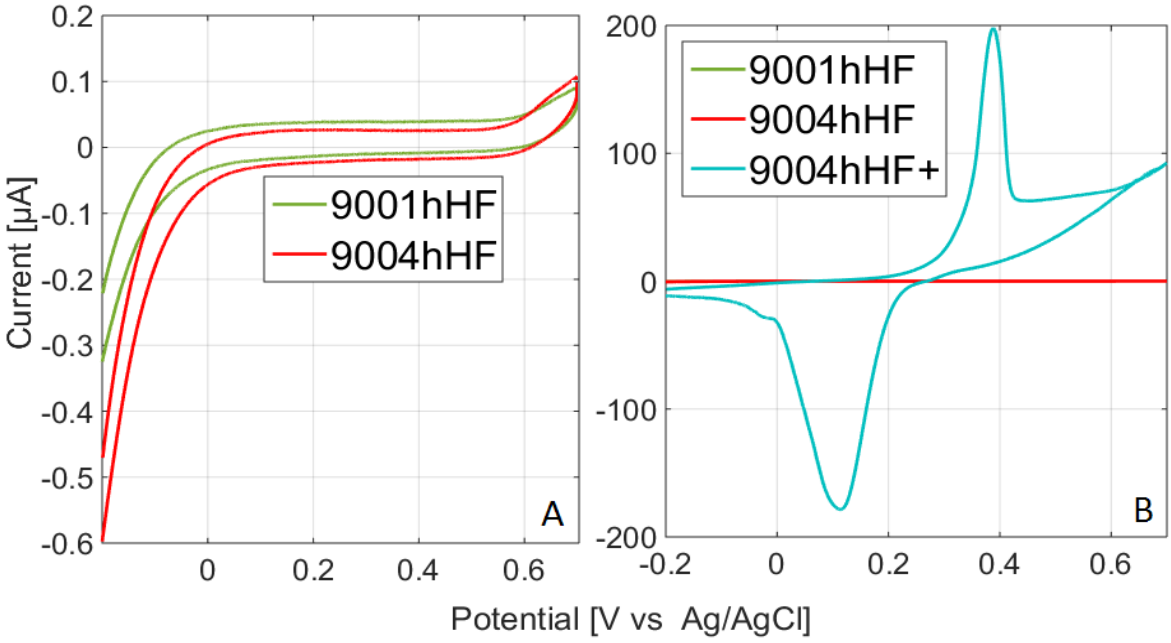

Figure 36. A) 1h (green) and 4h (red) PyC potential windows in cell culture media. B)Potential windows for 9004hHF+ (cyan), 9001hHF (green) and 9004hHF (red) electrodes in cell culture media.

The peaks were not visible in the 9004hHF+ electrode potential window in PBS. This means they are probably not caused by something like oxidation and reduction of quinone groups on the surface. Instead, it might be that the O_2 plasma treatment has increased the number of carboxyl and hydroxyl groups and these groups likely make the surface more reactive with some of the many organic molecules found in the media [40].

Table 8 summarizes the essential properties of the potential windows and background currents described in this Chapter. Potential window widths, background current intensities, approximate calculated values for double layer capacitance C_{dl} and faradaic peak locations are listed. All of the given values have come from results achieved with a scanning speed of 50 mV/s, if not otherwise specified. Equation 3 was used to calculate C_{dl}.

$$C_{dl} = \frac{I_a - I_c}{2 \cdot A \frac{dE}{dt}} \quad , \qquad (3)$$

where $I_a - I_c$ is the background current intensity, A is the electrode area and dE/dt is the cycling speed used.

Some of the electrode types were more prone to delamination than others, and in some cases it prevented electrode fabrication altogether. Films fabricated at 1000 °C and above showed extremely poor adhesion. HF treatment of the silicon before SU-8 coating resulted in better adhesion than O_2 treatment. Post-pyrolysation O_2 treatment also decreased film adhesion, while increased pyrolysation time improved it. Reduced cooling time also resulted in poorly adherent films.

The films showed generally high Ru values, although there was a lot of variation from electrode to electrode. One of the possible reasons for this variance is the kind of silicon substrate used, as that was not constant. Poor electrode contact to the conductor might also result in a high Ru value but additional measures were included in the electrode fabrication to avoid that. It is possible that high Ru values are typical for PyC films, as curve shapes from previous studies are often indicative of them. However, the studies do not usually report the Ru values for their electrodes. Post-pyrolysation oxygen plasma treatment clearly increased the Ru value of the electrodes, usually resulting in more than three times the initial value.

The background currents were generally low, in the scale of 5-15 nA/cm^2 for most electrodes. There was some variance between the electrode types, most notably oxygen plasma treatment significantly increased the background current. The potential windows generally ranged from around -0.3 V to 1 V against the reference electrode. Oxygen plasma treatment shifted the lower end of the potential window to higher voltages. They also showed an unstable potential window in the cell culture media, whereas the untreated electrodes showed a stable potential window.

The electrodes showed an unusually large number of faradaic peaks within the potential windows, although most of these peaks were really small in intensity. In H_2SO_4, most of the electrodes showed two faradaic peaks, at around 0.3 and 0.6 V against the Ag/AgCl reference electrode. These peaks tended to disappear in PBS for most electrodes. Electrodes fabricated in 800 °C show a large faradaic peak at 0.2 V, while this peaks disappears in the 900 °C electrodes. One of the peaks is likely caused by a quinone-like group on the electrode surface, but to confirm their origins, additional studies with XPS is required.

The double layer capacitance was generally low; 0.07 – 0.14 μF/cm^2 for untreated electrodes, and at least double after oxygen plasma treatment. It remained the same with different cycling speeds.

Table 8. Potential windows and background currents for all electrode types, against the Ag/AgCl reference electrode.

Electrode type	Potential windows	Background current I_{bc} and double layer capacitance C_{dl}
6001hHF	**H_2SO_4:** 1.4 V (-0.4 – 1 V)	**H_2SO_4: I_{bc}** = 14.1 nA/cm^2, **C_{dl}** = 0.14 µF/cm^2 **Faradaic oxidation peaks:** 0.33 V, 0.64 V
6001hO2	**H_2SO_4:** 1.8 V (-0.6 – 1.2 V)	**H_2SO_4: I_{bc}** = 7.1 nA/cm^2, **C_{dl}** = 0.07 µF/cm^2 **Faradaic oxidation peaks:** 0.45 V
8001hHF	**H_2SO_4:** 1.3 V (-0.3 – 1 V)	**H_2SO_4: I_{bc}** = 14.1 nA/cm^2, **C_{dl}** = 0.14 µF/cm^2 **Faradaic oxidation peaks:** 0.3 V, 0.56 V, 0.85 V **PBS, Faradaic oxidation peaks:** 0.18 V
8001hO2	**H_2SO_4:** 1.3 V (-0.2 – 1.1 V)	**H_2SO_4: I_{bc}** = 14.1 nA/cm^2, **C_{dl}** = 0.21 µF/cm^2 **Faradaic oxidation peaks:** 0.3 V, 0.56 V **PBS, Faradaic oxidation peaks:** 0.20 V
9001hHF	**H_2SO_4:** 1.5 V (-0.3 – 1.2 V) **PBS:** >0.5 V (0 – 0.5 V) **Media:** 0.8 V (-0.1 – 0.7 V)	**H_2SO_4: I_{bc}** = 14.1 nA/cm^2, **C_{dl}** = 0.14 µF/cm^2 **Faradaic oxidation peaks:** 0.35 V, 0.56 V, 0.72 V **PBS: I_{bc}** = 7.1 nA/cm^2 before 10 cycles, 5.7 nA/cm^2 after. **C_{dl}** = 0.07 µF/cm^2 before and 0.06 µF/cm^2 after 10 cycles. **Faradaic oxidation peaks:** 0.17 V **Media: I_{bc}** = 5.1 nA/cm^2, **C_{dl}** = 0.07 µF/cm^2, no peaks
9001hO2	**PBS:** >0.5 V (0 – 0.5 V)	**PBS: I_{bc}** = 7.1 nA/cm^2 before 10 cycles, 5.7 nA/cm^2 after. **C_{dl}** = 0.07 µF/cm^2 before and , 0.06 µF/cm^2 after 10 cycles. **Faradaic oxidation peaks:** 0.17 V
9004hHF	**H_2SO_4:** 1.5 V (-0.3 – 1.2 V) **PBS:** >0.9 V (-0.3 – 0.6 V) **Media:** 0.75 V (-0.05 – 0.7 V)	**H_2SO_4: I_{bc}** = 14.1 nA/cm^2 **C_{dl}** = 0.14 µF/cm^2 **Faradaic oxidation peaks:** 0.36 V, 0.57 V **Scanning speed effect:** background current increase to 141 nA/cm^2 (**C_{dl}** = 0.14 µF /cm^2), increase in faradaic peak intensities with 500 mV/s **PBS: I_{bc}** = 7.1 nA/cm^2, **C_{dl}** = 0.14 µF/cm^2 **Faradaic oxidation peaks:** 0.058 V, 0.31V **Media: I_{bc}** = 7.1 nA/cm^2, **C_{dl}** = 0.07 µF/cm^2, no peaks
9001hHF+	**H_2SO_4:** 1.3 V (-0.1 – 1.2 V)	**H_2SO_4: I_{bc}** = 28.3 nA/cm^2, **C_{dl}** = 0.28 µF/cm^2 **Faradaic oxidation peaks:** 0.33 V, 0.44 V
9004hHF+	**H_2SO_4:** 1.2 V (0V – 1.2 V) **PBS:** 0.8 V (-0.2 – 0.6 V) **Media:** none, large faradaic peaks	**H_2SO_4: I_{bc}** = 42.4 nA/cm^2, **C_{dl}** = 0.42 µF/cm^2 **Faradaic oxidation peaks:** 0.44V, 0.6 V **Scanning speed effect:** background current increase to ~ 424 nA/cm^2 (**C_{dl}** = 0.42 µF/cm^2), great intensity increase in faradaic peaks, when increased to 500 mV/s **PBS: I_{bc}** = 14.1 – 21.2 nA/cm^2, **C_{dl}** = 0.42 µF/cm^2 **Faradaic oxidation peaks:** -0.03 V, 0.17 V **Media:** unstable window, **C_{dl}** = 14.1µF/cm^2 **Faradaic oxidation peaks:** 0.39 V

7.2.2 **Outer sphere electron transfer**

1 mM FcMeOH solution was used as the outer sphere probe in these measurements. Figure 37 shows the outer sphere behaviour for electrode types 6001hHF, 6001hO2, 8001hHF and 8001hO2. There is a clear difference in the peak separations ΔEp for the two different fabrication temperatures. Type 8001hHF electrode shows the smallest peak separation of 66 mV, with oxidation peak at 0.264 V and reduction peak at 0.198 V against the reference electrode. The peak intensity rate is also about 1, so the reaction is quite reversible. The ΔEp of the 8001hO2 electrode is not much larger. The peak separation for the 6001hHF electrode is 880 mV and for the 6001hO2 electrode it is 1.46 V. The slope of the 6001hO2 electrode seems to be notably more tilted than the rest of the electrodes. This can be attributed to the large Ru value of 2100 Ω which is more than 4 times that of the second largest 500 Ω for 8001hO2. Likewise the 8001hHF peak is the least sloped and it has an Ru value of 40 Ω.

There is likely a much larger level of disorder and a much lower degree of graphitization in the 600 °C electrodes, in comparison to the 800 °C electrodes [26]. This might be the cause for the slower electrode kinetics. From the electrode transfer point of view, the electrode types 8001hHF and 8001hO2 are clearly superior, with 8001hHF having a slight advantage over 8001hO2. Only cycling speed of 50 mV/s was applied on these electrodes, as they were only used for preliminary results in order to find optimal fabrication parameters.

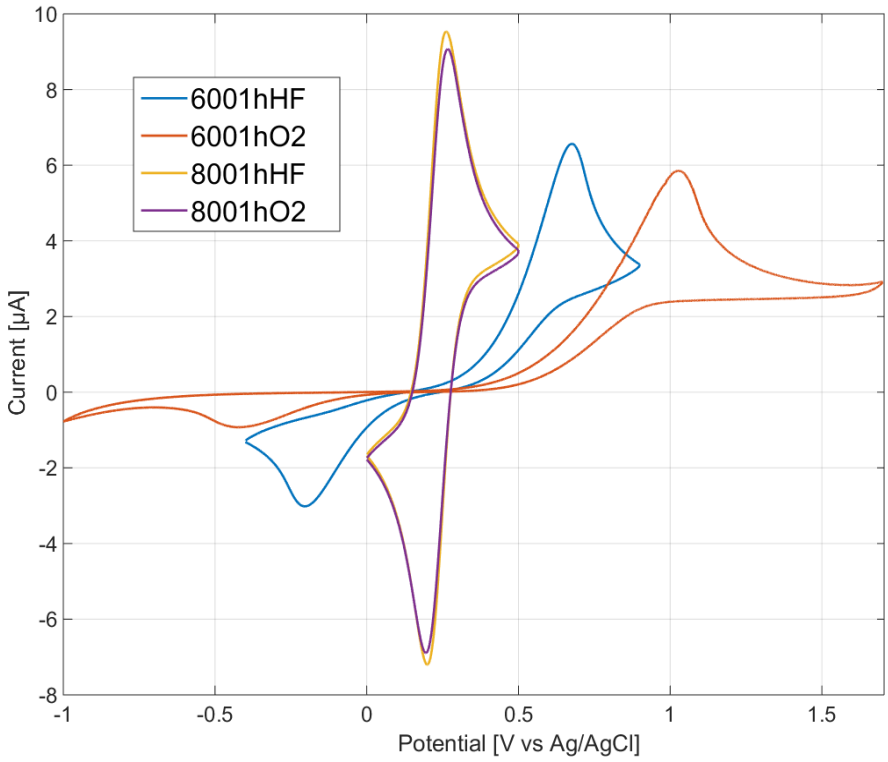

Figure 37. FcMeOH outer sphere electron transfer behaviour of 6001hHF (blue), 6001hO2 (orange), 8001hHF (yellow) and 8001hO2 (purple) electrodes.

Outer sphere probing was also done with 9001hHF, 9004hHF, 9001hHF+ and 9004hHF+ electrodes (Figure 38). Of these, the 9001hHF electrode shows the shortest ΔEp of 73 mV, with the 9004hHF electrode showing an almost identical behaviour. The plasma treated electrodes have much larger ΔEp. The ΔEp for the 9004hHF+ electrode is smaller; 588 mV. ΔEp for the 9001hHF+ electrode is larger than 1 V. For the untreated electrodes, the deformation due to Ru does not seem to be significant, even though they exhibit Ru values of around 2000 Ω. The plasma treated electrodes show significant tilting, which is to be expected, as they had extreme Ru values between 5000 and 7500 Ω.

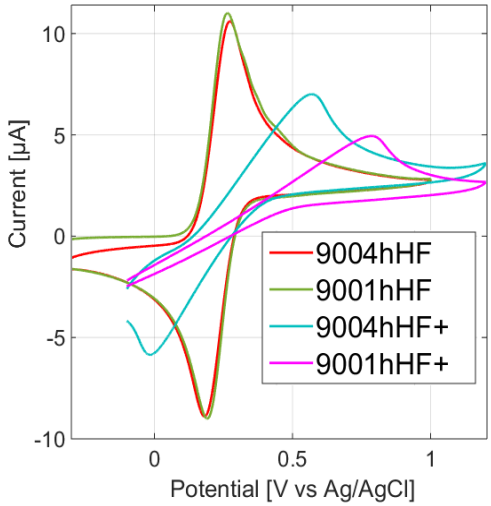

Figure 38. 9001hHF (green), 9004hHF (red), 9001hHF+ (magenta) and 9004hHF+ (cyan) in FcMeOH.

The plasma treatments slow down the electron transfer and reduced the oxidation peak intensity, especially for the 9001hHF+ electrode. This result is strikingly different than those achieved by previous studies with methane-based PyC (Figure 18) [3, 51]. It is quite clear that both fabrication temperature and post-fabrication oxygen plasma treatment have significant effect on the intrinsic electrochemical properties of the resulting PyC carbon film. The change of surface structure with increasing fabrication temperature is obvious enough, as a higher level of graphitization can be expected. It is also obvious that oxygen plasma treatment affects not only the surface functionalities of the PyC films, but also the surface structure itself, increasing film resistivity and disrupting electron transfer.

The effect of cycling speed on 9004hHF+ electrodes can be seen in Figure 39A and the effect on 9004hHF electrodes can be seen in Figure 39B. In both cases the increase in the cycling speed also increases the peak separation. When increasing the scanning speed from 50 mV/s to 500 mV/s, the location of the oxidation peak shifts from about 0.48 V to 1.03 V against the reference electrode on the 9004hHF+ electrode, while the oxidation peak of the 9004hHF electrode shifts from 0.27 V to 0.32 V. The curves in Figure 39 A are extremely sloped, which could be caused by the extremely high Ru value.

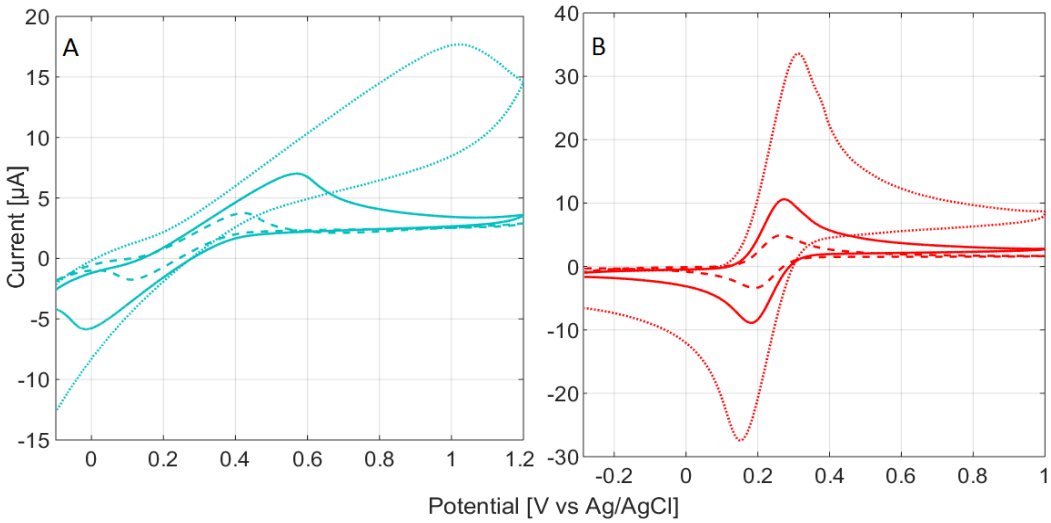

Figure 39. FcMeOH responses for: A) 9004hHF+ electrode, B) 9004hHF electrode. Cycling speeds: 10 mV/s (dashed), 50 mV/s (solid), 500 mV/s (dotted).

The electron transfer rate is much more sensitive to a change in the scanning speed with O_2 plasma treated electrodes. This was to be expected, as increasing cycling speed has more effect on more irreversible reactions [42]. This might be attributed to a blocking effect caused by the surface oxides, but the role of the ohmic drop should also be considered. [28]

7.2.3 **Dopamine detection**

In this section, electrode sensitivity towards DA will be evaluated in PBS for 800 °C and 900 °C PyC electrodes and in cell culture media for 900 °C PyC electrodes. Then, the selectivity of the 900 °C electrodes between AA and DA will be evaluated and the effects of anodization and O_2 plasma treatment are discussed.

In PBS

Figure 40A shows the response of a 8001hHF electrode to DA and Figure 40B shows the respective response of a 8001hO2 electrode. It should be mentioned that a faradaic peak appears for these electrodes, even though no such peak was visible in the PBS potential window measured for 900 °C electrodes, nor in the H_2SO_4 potential windows for these electrodes. This peak is possibly caused by a quinone on the electrode surface, although a more thorough surface analysis would be required to confirm this. The quinone peak pair also seems to be at the same location as the DA peak, possibly with a slightly faster electron transfer. ΔE_p for both electrodes is about 70 mV. This indicates that the quinone serves as a mediator for the electron transfer in lower fabrication temperature PyC films, but is maybe evaporated at higher fabrication temperatures, as it could not be seen in their potential windows.

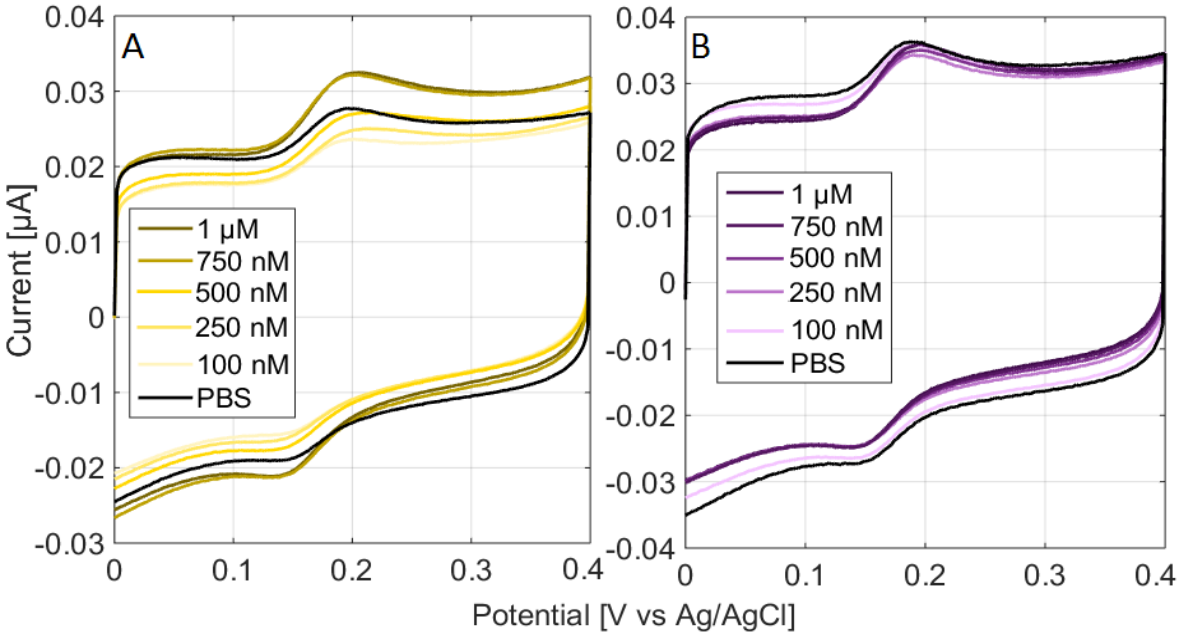

Figure 40. PBS only can be seen in black for both of the figures. A) 8001hHF (yellow) in DA concentrations from 100 nM (lightest) to 1µM (darkest) in PBS. B) 8001hO2 (purple) in DA concentrations from 100 nM (lightest) to 1µM (darkest) in PBS.

With both electrode types, the background current decreases immediately after the addition of DA, likely because DA consumes whatever oxygen might be left in the solution. In the 8001hO2 electrode, the current peak never exceeds the PBS curve even at DA concentrations of 1 µM. The 8001hHF electrode only exceeds it in 750 nM. Both because of the disturbing quinone peak and the current drop with DA addition, it would be difficult to use these electrodes in DA concentration estimation. Both of the electrodes show a nonlinear behaviour with increasing DA concentration. The overall peak shapes are more shoulder-like than clear peaks, as the potential drop after the peak is small compared to the peak height.

The films fabricated at 900 °C perform clearly better in this respect. This is evident from Figures 41 and 42, showing the responses of electrode types 9001hHF and 9001hO2 respectively. In these Figures, the grey curves shows the response in PBS before adding DA and black curves shows the response in PBS after the DA measurements. The drop in background current is about 1.4 nA/cm^2. In contrast to 8001hHF and 8001hO2 electrodes, there is no visible quinone peak in the PBS curves.

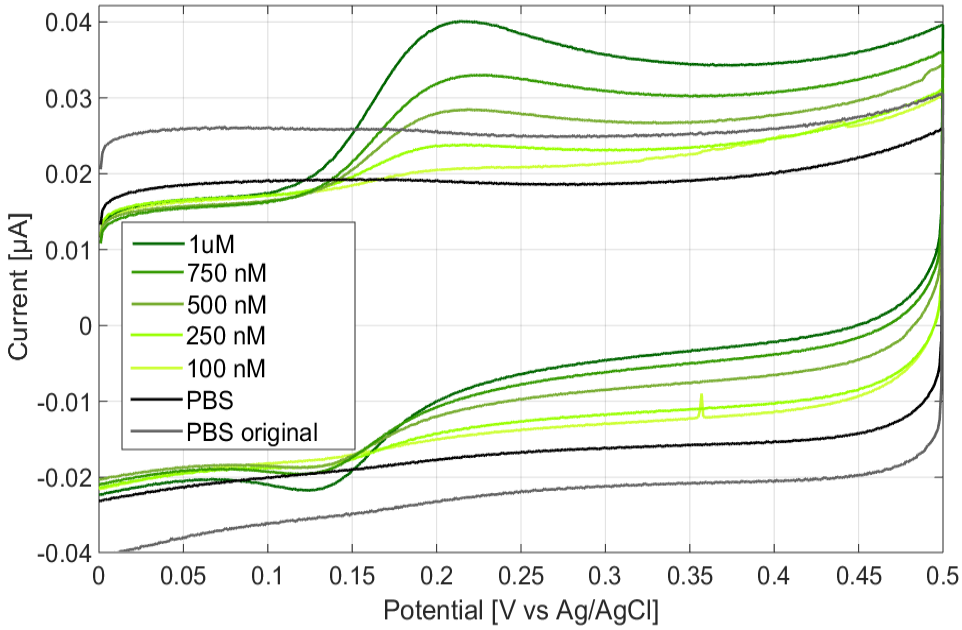

Figure 41. 9001hHF behaviour in DA concentrations from 100 nM (lightest) to 1µM (darkest) in PBS (grey = PBS before adding DA and black = PBS after DA measurement).

With both electrode types 9001hHF and 9001hO2, the concentrations from 500 nM and above can be detected above the initial PBS curve. The 9001hHF electrode is able to detect slightly lower concentrations and exhibits more defined peak shapes, albeit the potential drop after the peaks is still slight at best. All of the concentrations measured exceed the lower PBS curve and could potentially be detected with these electrodes. As for the reduction peaks, they are barely visible below 750 nM solution and never reach the intensity of the larger PBS potential window.

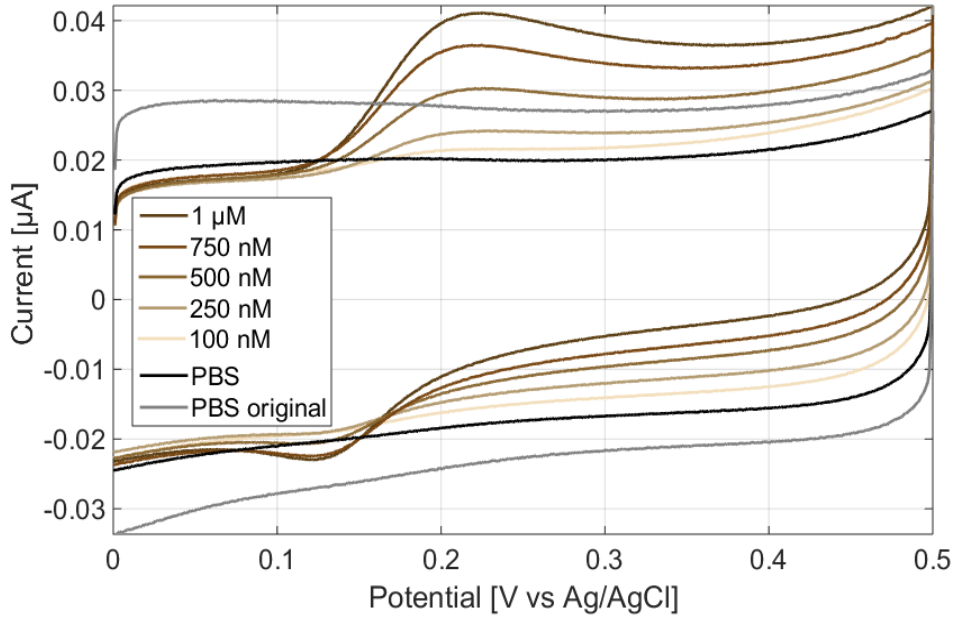

Figure 42. 9001hO2 behaviour in DA concentrations from 100 nM (lightest) to 1µM (darkest) in PBS (grey = PBS before adding DA. Black = PBS after DA measurement).

As is evident from Figure 43, both 9001hHF and 9001hO2 show rather linear increase in I_{po} with increasing DA concentration. This was not the case previously with 8001hHF and 8001hO2 samples (Figure 40). This is partially the reason why 900 °C samples were chosen to be used in most of the measurements. ΔE_p for both electrodes is about 90 mV. This is larger than that of the 800 °C and might be at least partially due to the disappearance of the quinone peak.

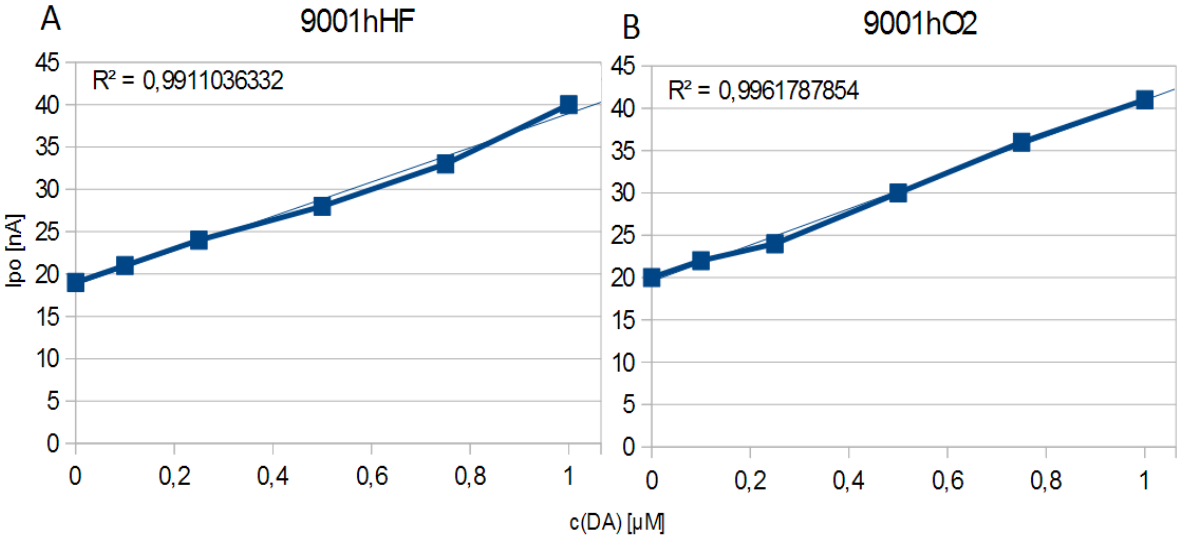

Figure 43. I_{po} as a function of DA concentration for A) 9001hHF and B) 9001hO2

In Cell culture media

The ability of PyC to detect DA was studied in cell culture media, using electrode types 9001hHF, 9004hHF and 9004hHF+. As shown previously in Section 7.2.1, the potential window for these electrodes ranges from -0.1 V to 0.7 V against the pseudo reference in cell culture media.

Figure 44 shows the voltammograms for A) 9001hHF electrode and B) 9004hHF electrode in culture media containing DA. In both cases, the oxidation-reduction peaks are located at the edges of the potential window and the peak separation is rather large. The peak separation is so high, the culture media clearly causes DA oxidation-reduction reaction to be limited by electrode kinetics. This might be due to some kind of blocking effect caused by a component of the media, which might have been adsorbed on the electrode surface, thus hindering DA adsorption.

An additional redox peak can be also seen around 0.3 V against the pseudo reference. This peak is not visible in the potential windows shown in 7.2.1. It is likely a reduction peak of an analyte oxidizing above 0.7 V. Because this peak was not visible in the PBS potential window even with scanning up to 1.2 V, it is possibly a component of the cell culture media.

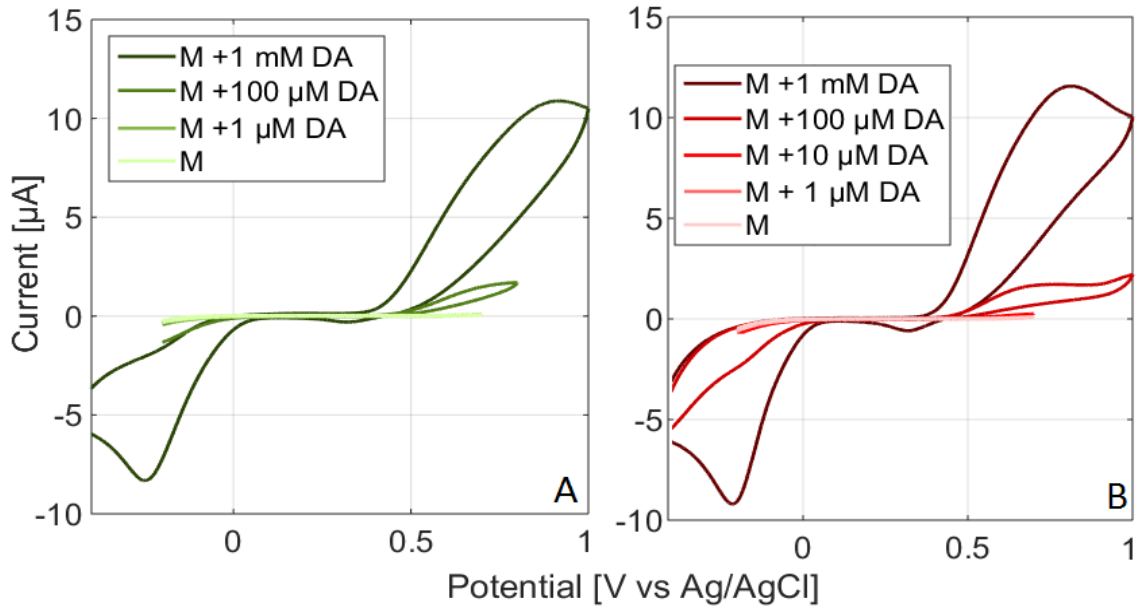

Figure 44. Voltammograms of A) 9001hHF and B) 9004hHF electrodes. Measured in cell culture media (lightest curves), and DA concentrations up to 1mM (increasing darkness).

The effect of lower concentrations for 9004hHF electrode can be seen in Figure 45. There is an increase in current intensity at the edges of the potential window, with an increase to the DA concentration. However, is clear that the DA peaks are located at the edge of the potential window, which might make the detection of low DA concentrations extremely difficult. There is no sign of the additional redox peak that is visible in Figure 44, which seems to affirm that it results from an analyte oxidizing above 0.7 V.

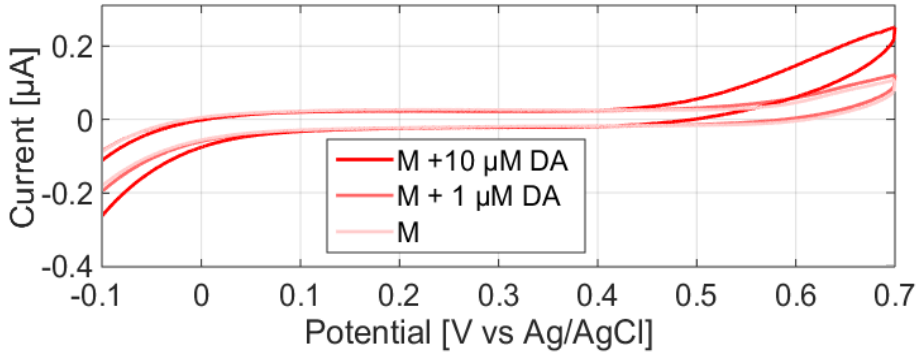

Figure 45. Type 9004hHF electrode in cell culture media (lightest red), and DA concentrations of 1µM (middle red) and 10µM. (darkest red

Figure 46 shows the voltammogram of a 9004hHF+ electrode in cell culture media containing DA. As shown in 7.2.1, the 9004hHF+ electrode in media only showed an oxidation peak at around 0.39 V and a reduction peak at about 0.12 V against the reference electrode. The DA oxidation-reduction peaks seem to be located close to these peaks, as they grow in intensity with increasing DA concentration, suggesting a reaction mediated the surface. Compared to the untreated electrodes, this results in a much faster electrode kinetics. However, the interfering peak also makes the quantitative DA detection much more difficult.

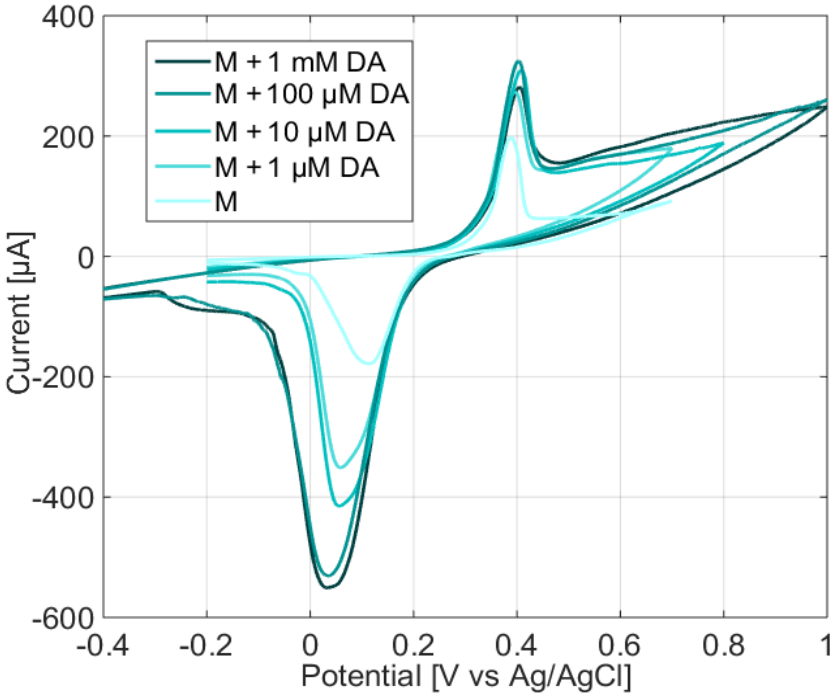

Figure 46. 9004hHF+ electrode in solutions from Media (lightest) to 1mM DA (darkest).

Measuring DA concentrations with PyC is obviously problematic in cell culture media and other complex solutions. This is due to multiple factors such as the relatively narrow potential window, slow electron transfer for DA and numerous possible interfering agents.

Selectivity between DA and AA

As they are, there does not seem to be any peak separation between AA and DA on plain PyC films, even in high DA concentrations. This is evident from Figure 47, which shows 9001hHF (A) and 9004hHF (B) electrodes in 1 mM DA + 1 mM AA PBS solution.

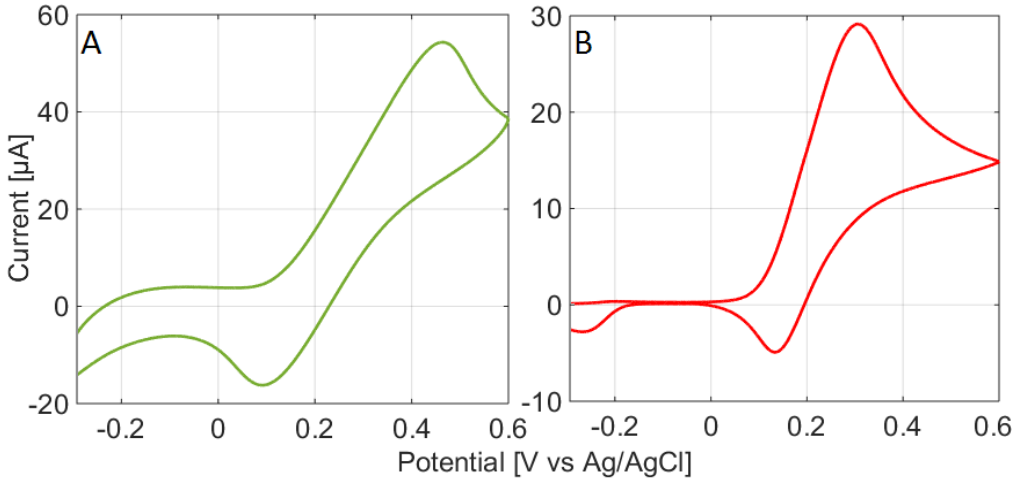

Figure 47. Voltammograms for A) 9001hHF and B) 9004hHF electrodes in 1 mM DA + 1 mM AA solution in PBS.

Cycling speed can be used to define DA concentration in the basis of the reduction peak. As explained in Chapter 3, AA oxidation is an irreversible reaction, so it has no reduction peak. With slow cycling speeds, DA will also have a significantly reduced reduction peak, as DAQ has time to react further. However, at high cycling speeds, there is less time for this, thus enabling the measurement of a greater DA reduction peak.

This is evident from Figure 48, where a 9001hHF electrode has been used to measure the change in potential in 100 µM AA and in 100 µM DA + 100 µM AA with speeds of 50 mV/s and 500 mV/s. With 50 mV/s the DA reduction peak is barely visible, while with the cycling speed of 500 mV/s it is over 2 µA in intensity. The curve with AA only does not naturally show a reduction peak at all.

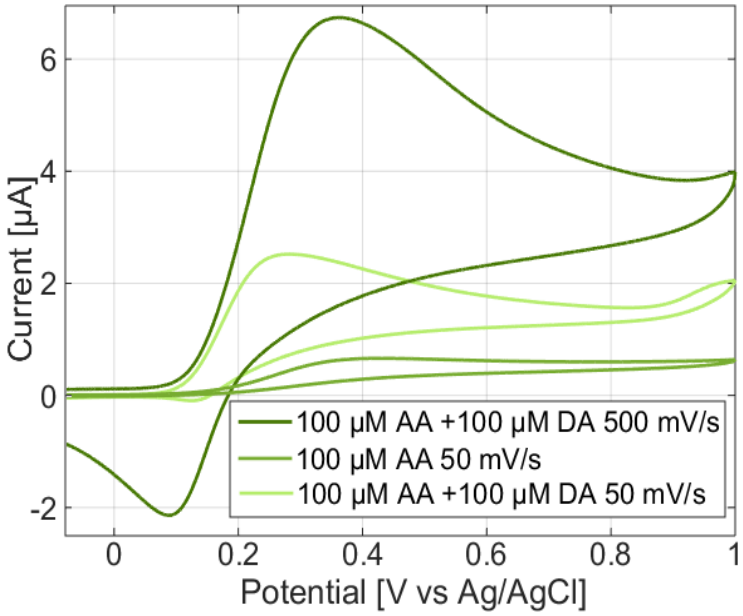

Figure 48. Voltammogram for a 9001hHF electrode in 100 µM AA (medium green) and 100 µM AA + 100 µM DA (light and dark green) with the cycling speeds of 50 mV/s (light and medium green) and 500 mV/s (dark green).

The AA peak is located at around 0.34 V against the Ag/AgCl reference, while the AA + DA peak on the same electrode is located at 0.25 V and the DA peak was located around 0.22 mV (Figure 41). Here, the location of the DA peak is little above 0.3 V, so the combined peak is naturally located in between the two. The location of the peaks is curious, as the DA peak is typically located at higher potentials than the AA peak for carbon materials. For example, Figure 22 showed the AA peak below 0.22 V and the DA peak close to 0.40 V against a Ag/AgCl reference. The effect persists later for untreated electrodes but the peak positions seem to switch with oxygen plasma treatment and anodization, as will be shown next.

O_2 plasma treatment was applied on 9001hHF and 9004hHF electrodes, to create electrode types 9001hHF+ and 9004hHF+ respectively. 9001hHF+ electrodes had a tendency to delaminate during electrode fabrication. One of the aims of this treatment was to enhance DA interaction with the surface and possibly aid in separating the peaks of AA and DA. Figure 49 shows the response of 9004hHF and 9004hHF+ electrodes in PBS, 1 mM AA and 1 mM AA + 100 µM DA. A much sharper contrast and an upwards shift can be detected on the 9004hHF+ electrode with the addition of DA, along with a well-defined peak. A shift downwards is seen on the 9004hHF electrode. The O_2 plasma treatment seems to be shifting the DA peak towards higher potentials, yet there is no peak separation to be seen. An AA shoulder can be detected on the left slope of the purple curve.

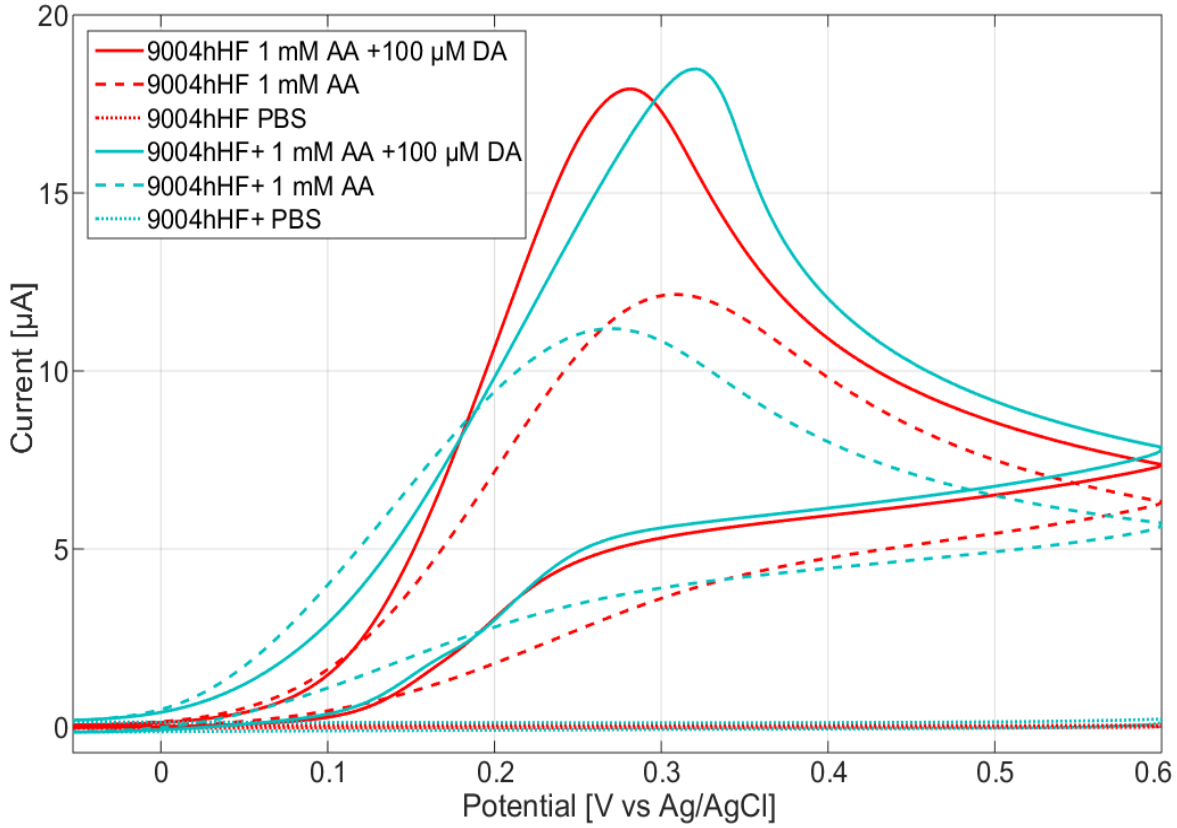

Figure 49. 9004hHF (red), and 9004hHF+ (cyan) electrodes in PBS (dotted), 1 mM AA (dashed) and 1 mM AA + 100 µM DA (solid).

Decreasing the cycling speed to 10 mV/s is useful in 9004hHF+ electrodes, as can be seen in Figure 50. What is a shoulder in 50 mV/s is almost a separate peak in 10 mV/s. Increasing the cycling speed to 500 mV/s on the other hand shifts the oxidation peak well beyond 0.6 V against the reference electrode. In a 9004hHF electrode no such improvement in selectivity can be seen with the lower cycling speed. The oxidation peak is also maintained well within the potential window in the higher speed. The sloped curves seem like they would be indicative of large IR drop. The 9004hHF electrode had an Ru value of about 1600 Ω, while the 9001hHF (Figure 48) had an Ru value of about 1200 Ω and the 9004hHF+ electrode had an Ru value of about 5500 Ω. This is in agreement with the sloping seen in the figures.

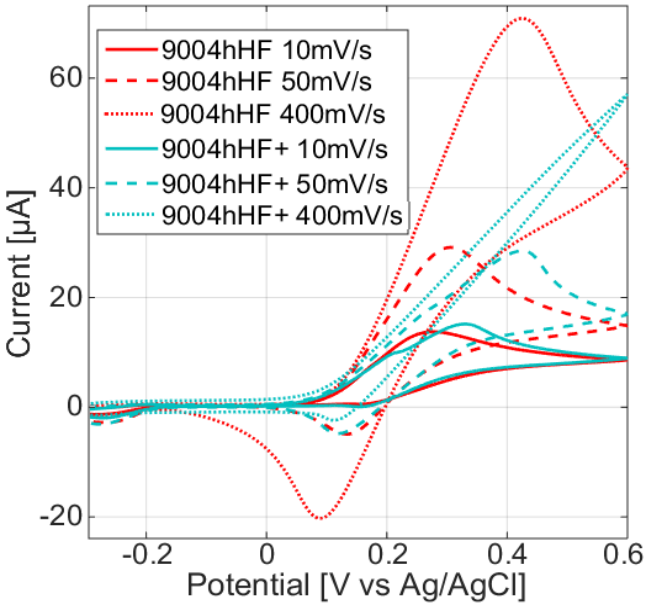

Figure 50. 9004hHF+ electrode (cyan), and 9004hHF electrode (red) in 1 mM DA + 1 mM AA in PBS. Cycling speeds 10 mV/s (solid), 50 mV/s (dashed) and 400 mV/s (dotted) used.

While the lower cycling speed was useful in detecting the high DA concentration of 1 mM (Figure 50), the effect is lost at lower concentrations. Figure 51 shows a 9004hHF+ electrode in different DA concentrations in cycling speed of 10 mV/s. With the addition of DA, the curve becomes more defined and shifts upwards. Alas, no peak separation is detected with 10 µM DA nor 100 µM DA, and these concentrations are still well below the values in vivo. Even slower scanning could be used but this significantly increases the time it takes to make a scan. With too much increase in the scanning time, any benefits of using CV would be lost.

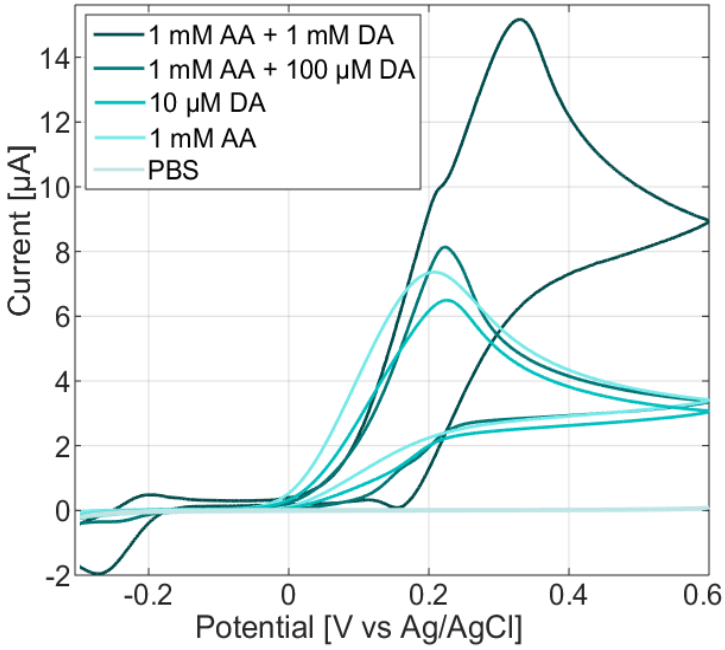

Figure 51. 9004hHF+ electrode in PBS (lightest), 1 mM AA (second lightest), and from 10 µM DA (middle) to 1 mM DA (dark cyan). Scanning speed of 10 mV/s used for all curves.

In previous studies of PyC, anodization had been suggested to aid in the selective detection of DA in the presence of AA (Chapter 3). Anodization for 1 minute in 1.7 V was applied in attempt to induce similar effect in a 9001hHF electrode, resulting in a 9001hHFA electrode. Figure 52A shows a 9001hHFA electrode in AA and various DA + AA concentrations. Figure 52B shows the same concentrations for a 9001hHF electrode.

Figure 52A shows the AA peak at a little below 0.3 V against the reference electrode. With increasing DA, an upwards shift of the peak can be seen. The shape of the peak shows the AA peak as a shoulder of the DA peak in higher DA concentrations. The DA reduction peaks shift are well-defined in high DA concentrations. The low concentrations might be better visible with a higher cycling speed.

In contrast, Figure 52B shows the AA peak in potential past 0.7 V. A shift downwards can be seen with increasing DA concentration. No peak separation is visible and the definition of the DA reduction peak is not as well-defined and can only be seen in the highest concentration. The shape of the anodized electrode curve seems to indicate again a high Ru value and IR drop, but the Ru value was not measured before the experiment.

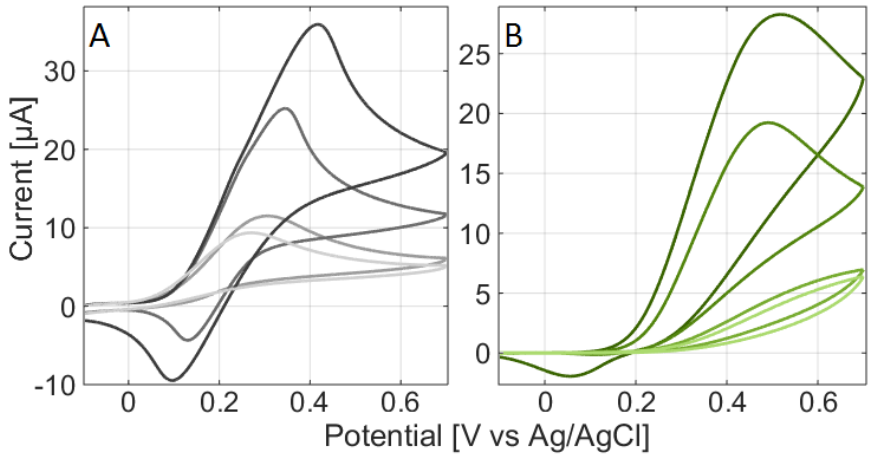

Figure 52. A) Type 9001hHFA electrode, and B) Type 9001hHF electrode in 1 mM AA (lightest), and in 1 mM AA + DA concentrations 10 µM, 1 mM and >1 mM. (darker line for higher concentration).

Table 9 summarizes the responses to ferrocenemethanol, DA and AA for all electrode types. Peak separations and peak intensities are given for the outer sphere redox pair. Peak separation, linearity and detection limit are given for DA when available. For DA+AA electrolytes, the findings regarding selectivity are described briefly.

Curiously, the ΔE_p values measured for FcMeOH and DA for untreated 800 °C and 900 °C PyC samples are notably smaller than similar values found in literature, as presented in Subchapter 3.2. For outer sphere redox groups, the difference is understandable, as none of the studies utilized FcMeOH as their outer sphere redox probe (but in stead $Fe(CN)_6^{3-/4-}$, which is not really an outer sphere probe to begin with). The outer sphere probe showed reversible reactions for untreated electrodes fabricated at 800 °C and 900 °C. The oxidation peak was located around 270 mV against the reference electrode for these materials. Lower fabrication temperatures and post-pyrolysation O_2 plasma treatment resulted in irreversible reactions, and shifted the oxidation peak to around 600 mV or above.

It is clear that higher fabrication temperature affects the electrochemical structure of the surface, but these results clearly indicate, that O_2 plasma treatment also drastically modifies the surface structure, and affects the intrinsic electrochemical properties of the material. Additional research should be done on the specific ways the structure is changed. The effect is very different to the previously detected effect of O_2 plasma treatment on outer sphere behaviour for acetylene-based PyC [51]. That study showed no increase in peak separation, and an increased peak definition. There might be significant differences in the plasma treatment parameters. Another explanation is that acetylene-based PyC is in some other way significantly different from SU-8 based PyC, even if they do share many structural similarities.

As for the inner sphere reactions, the behaviour of DA and effects of anodization and O_2 plasma treatment, seem to be almost the opposite to the effects in literature. Many of the studies reported a sluggish behaviour of the $Fe(CN)_6^{3-/4-}$ probe or DA on an as deposited PyC that improved upon film O_2 plasma treatment (or anodization) [1, 3, 9, 51]. In this study, both anodization and O_2 plasma treatment increase DA peak separation. The DA peak typically appears at around 200 mV in PBS for untreated electrodes (at the same location as the faradaic background peak for the 800 °C electrodes). The 900 °C electrodes showed a promising linear dependence between DA concentration and peak intensity, and sensitivity in the range of hundreds of nM. In cell culture media, the dopamine reaction is extremely slow for the untreated electrodes and faster but disturbed by high faradaic background peaks for the O_2 plasma treated electrodes.

Perhaps the most curious phenomenon was detected on the location of DA and AA peaks on the electrodes. For untreated electrodes the DA oxidation peak appeared at around 200 mV, while the AA oxidation peak appeared at 300 – 400 mV for the untreated electrodes. In other words, the DA peak appeared at a lower potential than the AA peak, even though the order is usually reverse for carbon materials. With O_2 plasma treatment and anodization, the DA peak shifted to above 300 mV, while the AA peak appeared at about 270 mV, so these treatments reversed the peak order.

No clear selectivity between the DA and AA peaks could be detected in any of the samples for realistic analyte concentrations. Shoulder peak was induced by slow scanning speed, anodization and oxygen plasma treatment with high DA concentration, and rather well defined DA reduction peaks were detected with fast scanning speeds, so there is at least some potential for selective DA detection with this material.

All in all, both O_2 plasma treatment and anodization seem to have some positive effect on the selective detection of DA in the presence of AA. They both cause a similar upwards shift of the DA peak. In addition anodization results in better defined oxidation and reduction peaks. The effect of cycling speed on the behaviour of the anodized electrode is unfortunately yet to be determined. Additionally, both plasma treatment and anodization effects on the detection of DA without the presence of AA are yet to be determined. However, at this point it seems like both of the treatments have more adverse than beneficial effects on the electrochemical behaviour of the electrodes.

Table 9. Outer sphere redox probe and DA + AA responses for all electrode types against the Ag/AgCl reference electrode. E_{po} = Oxidation peak potential.

Electrode type	Outer sphere response	DA and AA response
6001hHF	**ΔE_p:** 880 mV, **E_{po}** = 670 mV **I_{po} :** 0.9 µA/cm^2, **I_{pr} :** 0.6 µA/cm^2	
6001hO2	**ΔE_p:** 1.46 V, **E_{po}** = 1.02 V **I_{po} :** 0.8 µA/cm^2, **I_{pr} :** 0.4 µA/cm^2	
8001hHF	**ΔE_p :** 66 mV, **E_{po}** = 260 mV **I_{po} :** 1.4 µA/cm^2, **I_{pr} :** 1.4 µA/cm^2	**In PBS + DA:** **ΔE_p:** 70 mV, **E_{po}** = 190 mV **Linearity:** no **Detection limit:** >500 nM
8001hO2	**ΔE_p:** 70 mV, **E_{po}** = 270 mV **I_{po} :** 1.4 µA/cm^2, **I_{pr} :** 1.4 µA/cm^2	**In PBS + DA:** **ΔE_p:** 70 mV, **E_{po}** = 200 mV **Linearity:** no **Detection limit:** > 1 µM
9001hHF	**ΔE_p:** 73 mV, **E_{po}** = 260 mV **I_{po} :** 1.4 µA/cm^2, **I_{pr} :** 1.4 µA/cm^2	**In PBS + DA:** **ΔE_p:** 90 mV, **E_{po}** = 210 mV **Linearity:** yes **Detection limit:** >250 nM **In media + DA:** **ΔE_p:** 1.16 V, **E_{po}** = 910 mV **In PBS + DA + AA:** **E_{po}** = 510 mV, **E_{poAA}** = 350mV
9001hO2		**In PBS + DA:** **ΔE_p:** 90 mV, **E_{po}** = 220 mV **Linearity:** yes **Detection limit:** >250 nM
9004hHF	**ΔE_p:** 74 mV, **E_{po}** = 280 mV **I_{po} :** 1.4 µA/cm^2, **I_{pr} :** 1.4 µA/cm^2 **Scanning speed effect:** Slight increase in peak separation	**In media + DA:** **ΔE_p:** 1.02 V, **E_{po}** = 310 mV **In PBS + DA + AA:** **E_{po}** = 280 mV, **E_{poAA}** = 310 mV
9001hHF+	**ΔE_p:** > 1 V, **E_{po}** = 790 mV **I_{po} :** -, **I_{pr} :** -	
9004hHF+	**ΔE_p:** 588 mV, **E_{po}** = 570 mV **I_{po} :** 1.1 µA/cm^2, **I_{pr} :** 1.0 µA/cm^2 **Scanning speed effect:** Extreme increase in peak separation	**In media + DA:** **ΔE_p:** 0.37 V, **E_{po}** = 400 mV **In PBS + DA +AA:** **E_{po}** = 320 mV, **E_{poAA}** = 270mV
9001hHFA		**In PBS + DA + AA:** **E_{po}** = 420 mV, **E_{poAA}** = 270mV

7.3 **Biocompatibility**

In this Subchapter, results for NSC MTT viability measurements (7.3.1) and a differentiation pathway study (7.3.2) will be presented. The effects of PLL coating, fabrication time and surface oxygen plasma treatment on cell viability will be evaluated and the viability will be compared to ta-C (S1 in graphs) carbon. The effects of PLL coating, oxygen plasma treatment, GF and GF + DF on cell differentiation pathway will be discussed and ways to improve the differentiation in the future will be considered.

7.3.1 **Neural stem cell viability**

The MTT protocol was repeated twice for 900 °C PyC films, fabricated on HF and O_2 plasma treated Si substrates. The results of these measurements can be seen in Figure 53. The results are consistent in both of the measurements, showing increased viability on the HF samples in comparison to the O_2 samples and on the PLL samples in comparison to the uncoated samples respectively. It would seem PLL coating increases viability, possibly due to increased cellular adhesion. It is hard to say why the HF substrate shows improved viability compared to the O_2 treated surfaces, as the surface properties of the O_2 samples were not characterized. PyC films did show poorer adhesion on the O_2 treated silicon, which might at least be part of the issue. However, no clear delamination was seen on the samples during the MTT measurements.

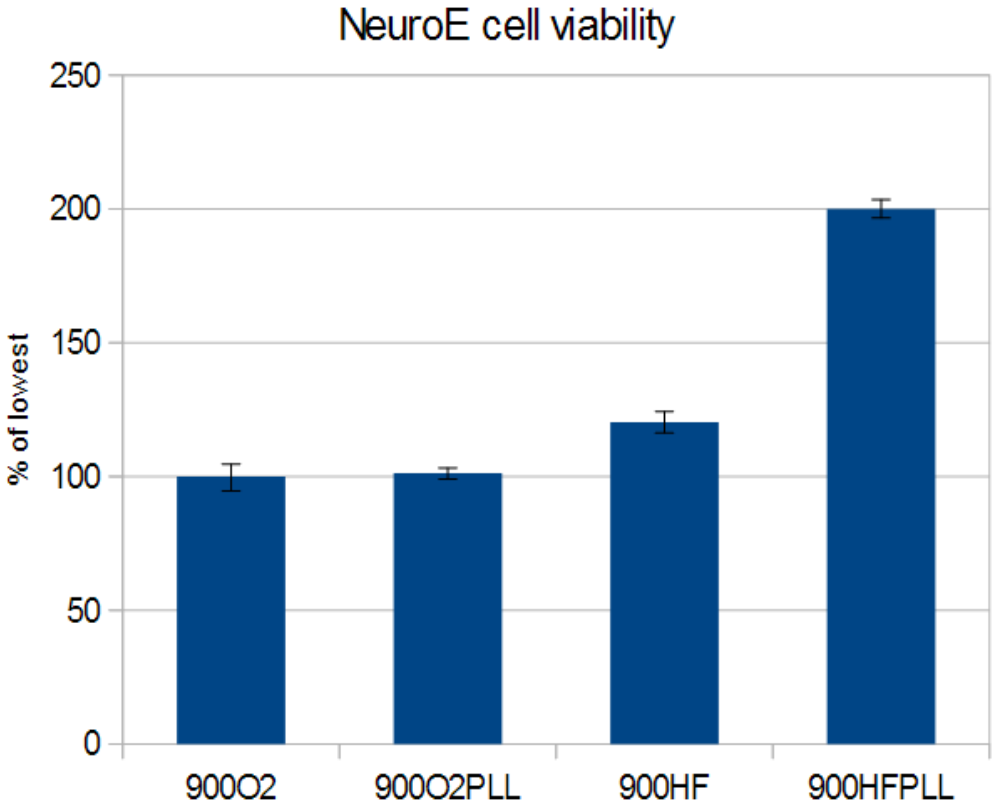

Figure 53. NSC viability (MTT) results on 900 °C PyC samples fabricated on O_2 and HF treated Silicon, with and without PLL coating. The viability is given as a % of the lowest viability sample, as an average of three samples.

Viability was also assessed on 1 and 4 hour PyC samples with and without post-pyrolysation oxygen plasma treatment and again with and without PLL coating. To get a reference from another nanocarbon material, ta-C samples were also included in the MTT protocol. The results are shown in Figure 54. In these results, nothing conclusive can be said about the effects of fabrication time nor PLL coating on the cellular viability. More repetitions of the protocol should be done on that accord. However, one clear trend can be seen in the results; the post-pyrolysation oxygen plasma treatment clearly improves the cell viability like it was supposed to. This could be due to an improved cell adhesion to the substrates, as the plasma treatment increases the surface energy and wettability. The results are in line with previous findings [9].

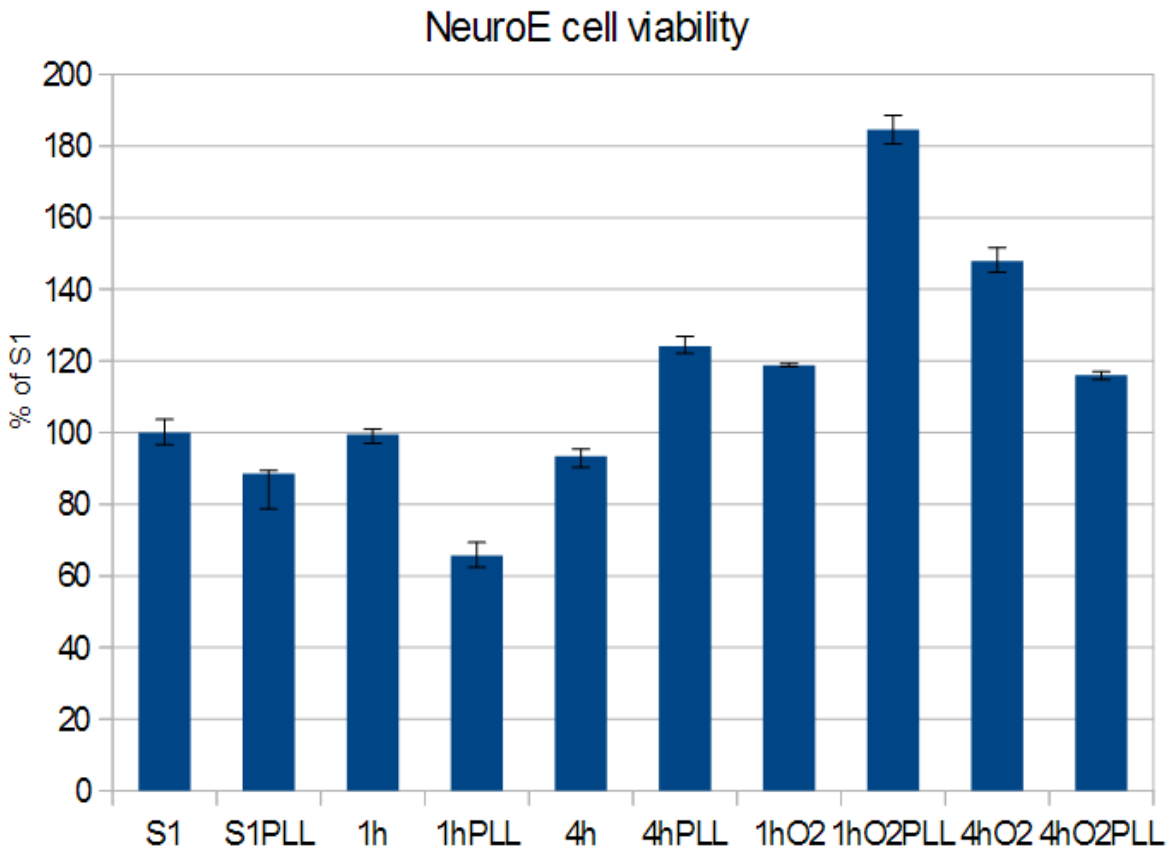

Figure 54. Viability of NeuroE cells on 1 h and 4 h 900 °C HF PyC materials with and without plasma treatment and PLL coating, as well as ta-C (S1) with and without PLL coating. Viability for all samples is given as % of the S1 sample.

7.3.2 **Neural stem cell differentiation**

The attempts to induce dopaminergic differentiation of mouse NSCs on SU-8 derived PyC were unsuccessful on all sample types. Neither treatment with 20 ng/ml bFGF nor treatment with 20 ng/ml bFGF + 1 ng/ml TSA resulted in increase of neuron specific NSE marker, no dopaminergic neuron specific TH marker. All of the samples only showed specific staining of neuronal progenitor marker nestin. PLL coating and oxygen plasma treatment were also ineffective.

Cellular differentiation pathway was studied for 9 days, with data points on days 3, 6 and 9. The cells kept proliferating during the whole period, also indicating that no differentiation of the cells occur. On day 9, all of the samples were packed with nestin positive cells. An example of the trend can be seen in Figure 55.

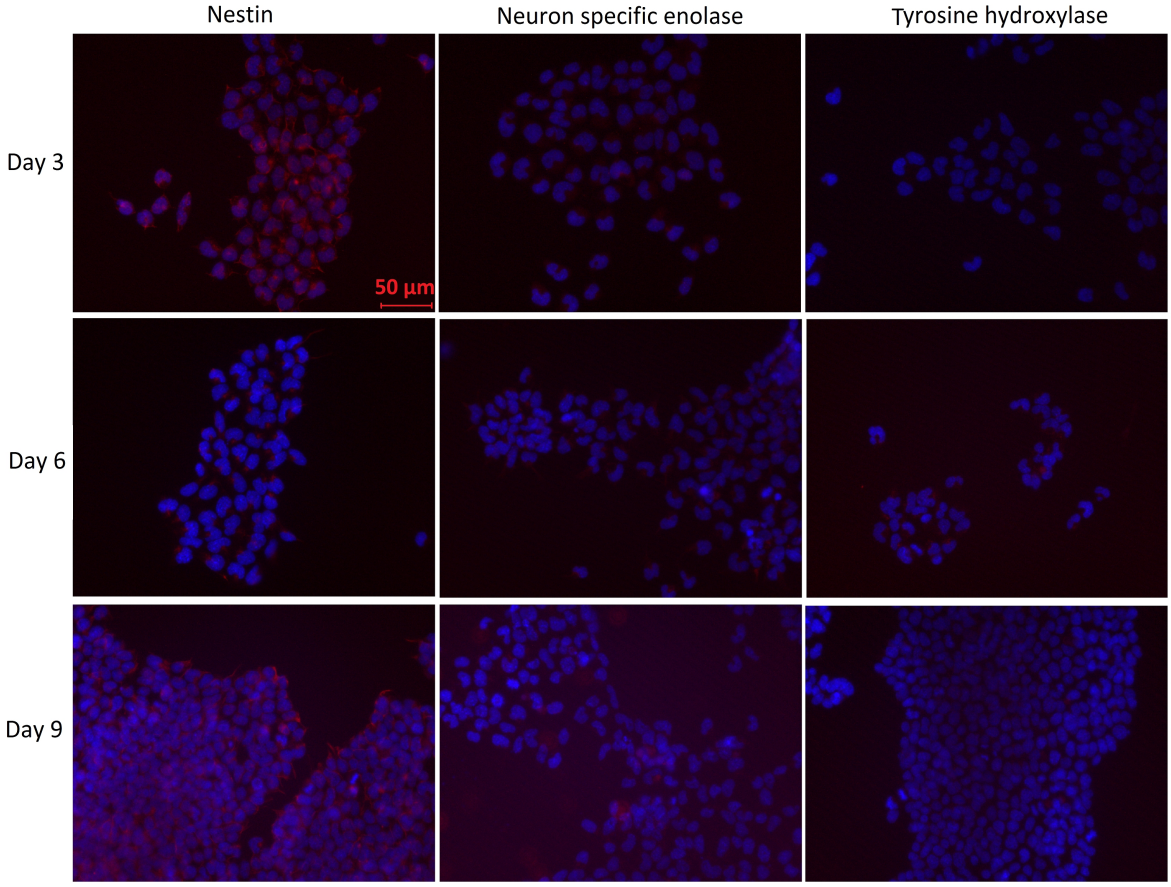

Figure 55. NeuroE cells grown on PLL coated 9001hHF PyC for 3, 6 and 9 days. Samples show specific staining of nestin. The cells have proliferated extensively over 9 days.

The results are very different from those documented previously [9]. However different GF and DF treatments were used in this study. It is possible that neuronal differentiation would be induced by using the same GF.

8 Conclusions

In this work, various structural, electrochemical and biocompatibility characterizations were made of SU-8 derived PyC films of various configurations. An attempt was made to evaluate the material in a context of PyC materials and of carbon nanomaterials in general. The previous studies done on relevant materials have not by large been systematic. They have also been more qualitative than quantitative in nature. For the reasons above, systematic and quantitative approach was taken when designing and conducting the experiments and reporting their results. Key findings from the results (described in full detail in Chapter 7) will be summarized here and suggestions for possible future work will be made.

The structural characterizations confirmed that SU-8 derived PyC films pyrolysed at 800 °C have low surface roughness (rms average < 1 nm). While this is extremely smooth as far as carbon films go in general, lower roughness values have been reported for PyC in previous occasions [9]. As 900 °C have been demonstrated to exhibit smoother surfaces [26], additional AFM characterization of appropriate samples would be desirable. 800 °C PyC film was also found to be rather conductive, exhibiting a resistivity of about $1.6 \pm 0.3 \times 10^{-4}\ \Omega\ m^2$.

Raman spectroscopy of a 900 °C PyC film was found to be much alike to other PyC films found in literature. It shows well-defined D and G peaks, with I_D/I_G peak ratio of about 3.3, indicative of high sp^2 content and small crystallite size. The crystallite size L_a was calculated to be about 5.8 nm. However, as the film is fabricated in high temperatures, these approximations may not be accurate. Additional characterization of the surface bonding should be done with UV-Raman, XPS or EELS for example, while additional characterization of the surface in general should be done with SEM. SU-8 PyC films are prone to delamination, so care should be taken when preparing samples for structural studies.

Electrochemically, PyC was found to exhibit relatively fast outer sphere electrode kinetics for untreated electrodes fabricated at 800 – 900 °C, with 800 °C PyC performing the fastest. This was in general in line with previous findings, although none of the previous studies on PyC utilized FcMeOH as the outer sphere probe. However, the results this study also contradicted previous findings [9, 51], as the electrode kinetics for FcMeOH were found to be fastest for the PyC film as fabricated, while post-pyrolysation oxygen plasma treatment resulted in slower kinetics and reduced peak current. Potential windows were found to range from 1.2 V to 1.8 V against the Ag/AgCl reference electrode in H_2SO_4 and from 0.5 V to 1 V in PBS. The respective background currents were about 300 nA at highest for all electrodes. These properties were replicated in cell culture media for untreated samples.

Films fabricated at 900 °C were found to be the most appropriate for DA sensing, as they showed an improved sensitivity over 800 °C PyC, a linear increase as a function of increasing DA concentration, while also maintaining a decent film adhesion during electrode fabrication. DA sensitivity of at least 500 nM was confirmed with cycling speed of 50 mV/s. Still, additional studies should be performed to find the lower limit for DA detection on PyC, as this has not been previously attempted in literature either.

The preliminary studies on DA measurement in cell culture media showed that DA oxidation is slow in the complex fluid, and peaks are located at the edges of the potential window. They were luckily still detectable. Post-pyrolysation oxygen plasma treatment, on the other hand, caused faster DA oxidation-reduction reaction, but also adsorption of interfering analytes. Additional measurements in media should be performed to better define and confirm these results.

No sufficient peak separation between AA and DA peaks was achieved in realistic reagent concentrations, but the materials showed potential for peak separation at high DA concentrations and fast cycling speeds. Curiously, the AA peaks were located at a higher potentials than the DA peaks for the untreated electrodes. This is highly unusual for carbon nanomaterials. Post-pyrolysation oxygen plasma treatment and anodization both reversed the peak order.

PyC was found to exhibit decent cell viability. The viability was improved on samples fabricated on HF treated Si and especially on post-pyrolysation oxygen plasma treated films. The effects of PLL coating and film fabrication time on viability were inconclusive. At least PLL coating is not required for good cellular viability, like it usually is when using NSCs. Non oxygen plasma treated, uncoated PyC exhibited viability in the scale of ta-C.

Differentiation of NSCs into neurons or dopaminergic neurons was unsuccessful, even with PLL coating, oxygen plasma treatment, bFGF and TSA stimulation. All of the different treatments with every combination behaved more or less identically on 900 °C PyC, as the cells were only stained positively with nestin, which is a marker for undifferentiated neural progenitors. Even after 9 days of time, no change could be seen. The cells also continued proliferation as usual, so after 9 days, all of the samples were covered in cells. For future work, attempting a different chemical stimulation is suggested. Additionally utilizing topographical cues to differentiate cells might help. Fortunately, because it is a photoresist, SU-8 is an ideal material to fabricate them. If dopaminergic differentiation of NSCs is at some point achieved on the material, additional studies by PCR and electrochemical measurement should be performed to confirm the presence of functional dopaminergic neurons.

The results presented in this thesis work are mostly preliminary. Overall there is still a lot of work to be done before PyC could be considered a feasible material for DA detection in vivo. There is both a lot of room and a lot of potential for improvement. While PyC is known for its good hemocompatibility, and it is not harmful to NSCs per sē, it still does not seem to support neuronal differentiation of NSCs in itself. Most of the other problems defined in the introduction of this work also still remain, including achieving peak separation of AA and DA and characterizing the material sensitivity towards DA in more complicated fluids. As opposed to the findings in previous studies, anodization and oxygen plasma treatment of the pyrolysed film might not be as advantageous from the electrochemical point of view as previously suggested, even if the plasma treatment clearly improves cellular viability on the material.

All in all, the results of this thesis work are promising. SU-8 derived PyC shows some unique and interesting electrochemical properties. The electrochemical behaviour seems to be consistent and predictable. A good film adhesion was achieved, and reversible DA oxidation was detected in reasonably low concentrations, with linear dependence in respect to the concentration. A potential for DA and AA peak separation is also apparent; not only are the peaks are located at different potentials, but their relative positions also seem to be tunable to some extent. The films show consistently wide potential windows, low background current, low double layer capacitance, and fast outer sphere electron transfer. While the material exhibits a surprisingly large amount of faradaic background peaks, their intensity is for untreated 900 °C films so low, it does not hinder DA measurement. There is also a lot of room for development, as this is a novel material, that can be easily fabricated into very complex structures, that can potentially be used to improve both the electrochemical and biocompatibility properties of the material.

9 References

[1] McEvoy, Niall, et al. "Synthesis and analysis of thin conducting pyrolytic carbon films." Carbon 50.3 (2012): 1216-1226.

[2] Singh, Amit, et al. "Pyrolysis of negative photoresists to fabricate carbon structures for microelectromechanical systems and electrochemical applications." *Journal of the electrochemical society* 149.3 (2002): E78-E83.

[3] Hadi, M., et al. "Electrochemical characterization of a pyrolytic carbon film electrode and the effect of anodization." Electroanalysis 18.8 (2006): 787-792.

[4] Hadi, Mojtaba, Ahmad Rouhollahi, and Mohammad Yousefi. "Nanocrystalline graphite-like pyrolytic carbon film electrode for electrochemical sensing of hydrazine." Sensors and Actuators B: Chemical 160.1 (2011): 121-128.

[5] Hadi, Mojtaba, and Ahmad Rouhollahi. "Simultaneous electrochemical sensing of ascorbic acid, dopamine and uric acid at anodized nanocrystalline graphite-like pyrolytic carbon film electrode." Analytica chimica acta 721 (2012): 55-60.

[6] Wu, Zhangxiong, et al. "Ordered mesoporous graphitized pyrolytic carbon materials: synthesis, graphitization, and electrochemical properties." Journal of Materials Chemistry 22.18 (2012): 8835-8845.

[7] Lux, Simon Franz, et al. "Electrochemical reactivity of pyrolytic carbon film electrodes in organic carbonate electrolytes." Electrochemistry Communications 46 (2014): 5-8.

[8] Hadi, M. "Electrochemical determination of guaifenesin in a pharmaceutical formulation and human urine based on an anodized nanocrystalline graphite-like pyrolytic carbon film electrode." Analytical Methods 7.20 (2015): 8778-8785.

[9] Amato, Letizia, et al. "pyrolysed 3D-Carbon Scaffolds Induce Spontaneous Differentiation of Human Neural Stem Cells and Facilitate Real-Time Dopamine Detection."*Advanced Functional Materials* 24.44 (2014): 7042-7052.

[10] Palomäki, Tommi, et al. "Electrochemical reactions of catechol, methylcatechol and dopamine at tetrahedral amorphous carbon (ta-C) thin film electrodes." *Diamond and Related Materials* 59 (2015): 30-39.

[11] Zhou, Hong, et al. "Photoresist derived carbon for growth and differentiation of neuronal cells."*International Journal of Molecular Sciences* 8.8 (2007): 884-893.

[12] Mitra, Jaba, et al. "Patterned growth and differentiation of neural cells on polymer derived carbon substrates with micro/nano structures in vitro."*Carbon*65 (2013): 140-155.

[13] Zhang, Huixing, Eddie López-Honorato, and Ping Xiao. "Fluidized bed chemical vapor deposition of pyrolytic carbon-III. Relationship between microstructure and mechanical properties." Carbon 91 (2015): 346-357.

[14] Hoshikawa, Yasuto, et al. "Remarkable enhancement of pyrolytic carbon deposition on ordered mesoporous silicas by their trimethylsilylation." Carbon 67 (2014): 156-167.

[15] Li, Wei, et al. "Effect of heat treatment on the microstructure of C/C composites with different high textured pyrolytic carbon contents."*Carbon* 82 (2015): 609.

[16] De Volder, Michael FL, et al. "Hierarchical carbon nanowire microarchitectures made by plasma-assisted pyrolysis of photoresist."*Acs Nano* 5.8 (2011): 6593-6600.

[17] Sharma, Chandra S., Ashutosh Sharma, and Marc Madou. "Multiscale carbon structures fabricated by direct micropatterning of electrospun mats of SU-8 photoresist nanofibers."*Langmuir* 26.4 (2010): 2218-2222.

[18] Steach, Jeremy K., Jonathan E. Clark, and Susan V. Olesik. "Optimization of electrospinning an SU-8 negative photoresist to create patterned carbon nanofibers and nanobeads." *Journal of applied polymer science* 118.1 (2010): 405-412

[19] Goto, A., et al. "Structure of pyrolytic carbon from polyacetylene." *Carbon* 39.13 (2001): 2082-2086.

[20] Sikanen, Tiina, et al. "Characterization of SU-8 for electrokinetic microfluidic applications." *Lab on a Chip* 5.8 (2005): 888-896.

[21] Shirakawa, Hideki. "The discovery of polyacetylene film: the dawning of an era of conducting polymers (Nobel lecture)." *Angewandte Chemie International Edition* 40.14 (2001): 2574-2580.

[22] Dong, G. L., and K. J. Hüttinger. "Consideration of reaction mechanisms leading to pyrolytic carbon of different textures." *Carbon* 40.14 (2002): 2515-2528.

[23] Heo, J. I., et al. "Carbon interdigitated array nanoelectrodes for electrochemical applications."*Journal of the Electrochemical Society* 158.3 (2011): J76-J80.

[24] De Volder, Michael FL, et al. "Hierarchical carbon nanowire microarchitectures made by plasma-assisted pyrolysis of photoresist." *ACS nano* 5.8 (2011): 6593-6600.

[25] Du, Rongbing, et al. "Fabrication and characterization of graphitic carbon nanostructures with controllable size, shape, and position." *Small* 5.10 (2009): 1162-1168.

[26] Lee, Jung A., et al. "Fabrication and characterization of freestanding 3D carbon microstructures using multi-exposures and resist pyrolysis." *Journal of Micromechanics and Microengineering* 18.3 (2008): 035012.

[27] Qian, Lichuan, and W. Mark Saltzman. "Improving the expansion and neuronal differentiation of mesenchymal stem cells through culture surface modification." *Biomaterials* 25.7 (2004): 1331-1337.

[28] Zoski, Cynthia G., ed. *Handbook of electrochemistry*. Elsevier, 2006.

[29] Chu, Paul K., and Liuhe Li. "Characterization of amorphous and nanocrystalline carbon films." *Materials Chemistry and Physics* 96.2 (2006): 253-277.

[30] Ferrari, Andrea Carlo, and John Robertson. "Raman spectroscopy of amorphous, nanostructured, diamond–like carbon, and nanodiamond."*Philosophical Transactions of the Royal Society of London A: Mathematical, Physical and Engineering Sciences* 362.1824 (2004): 2477-2512.

[31] Ferrari, Andrea C., and Jf Robertson. "Interpretation of Raman spectra of disordered and amorphous carbon." *Physical review B* 61.20 (2000): 14095.

[32] Cancado, L. G., et al. "General equation for the determination of the crystallite size La of nanographite by Raman spectroscopy." *Applied Physics Letters* 88.16 (2006): 163106-163106.

[33] Robertson, J. "Diamond-like amorphous carbon." *Materials Science and Engineering: R: Reports* 37.4 (2002): 129-281.

[34] Ooi, Newton, Asit Rairkar, and James B. Adams. "Density functional study of graphite bulk and surface properties." *Carbon* 44.2 (2006): 231-242.

[35] Radovic, Ljubisa R. "Active sites in graphene and the mechanism of CO2 formation in carbon oxidation." *Journal of the American Chemical Society* 131.47 (2009): 17166-17175.

[36] Tang, Longhua, et al. "Preparation, structure, and electrochemical properties of reduced graphene sheet films." *Advanced Functional Materials* 19.17 (2009): 2782-2789.

[37] Shao, Yuyan, et al. "Graphene based electrochemical sensors and biosensors: a review." *Electroanalysis* 22.10 (2010): 1027-1036.

[38] Pujadó, Mercè Pacios. *Carbon nanotubes as platforms for biosensors with electrochemical and electronic transduction*. Springer Science & Business Media, 2012.

[39] Denisenko, A., A. Aleksov, and E. Kohn. "pH sensing by surface-doped diamond and effect of the diamond surface termination." *Diamond and related materials* 10.3 (2001): 667-672.

[40] McCreery, Richard L. "Advanced carbon electrode materials for molecular electrochemistry." *Chem. Rev* 108.7 (2008): 2646-2687.

[41] Chen, Piehong, Mark A. Fryling, and Richard L. McCreery. "Electron transfer kinetics at modified carbon electrode surfaces: the role of specific surface sites." *Analytical Chemistry* 67.18 (1995): 3115-3122.

[42] Allen, J. Bard, and R. Faulkner Larry. "Electrochemical methods: fundamentals and applications." *Department of Chemistry and Biochemistry University of Texas at Austin, John Wiley & Sons, Inc* (2001): 156-176.

[43] Lai, Stanley, et al. "Definitive Evidence for Fast Electron Transfer at Pristine Basal Plane Graphite from High-Resolution Electrochemical Imaging."*Angewandte Chemie International Edition* 51.22 (2012): 5405-5408.

[44] Liu Y. et al. “Carbon nanorods derived from natural based nanocrystalline cellulose for highly efficient capacitive deionization.” *Journal of Materials Chemistry* 3.9 (2014): 20966-20972.

[45] Chen, Da, Longhua Tang, and Jinghong Li. "Graphene-based materials in electrochemistry." *Chemical Society Reviews* 39.8 (2010): 3157-3180.

[46] Menegazzo, Nicola, et al. "Compositional and electrochemical characterization of noble metal-diamondlike carbon nanocomposite thin films." *Langmuir* 23.12 (2007): 6812-6818.

[47] Lounasvuori, Mailis M., et al. "Electrochemical characterisation of graphene nanoflakes with functionalised edges." *Faraday discussions* 172 (2014): 293-310.

[48] Oda, Atsumu, et al. "Fluorinated Nanocarbon Film Electrode Capable of Signal Amplification for Lipopolysaccharide Detection." Electrochimica Acta 197 (2016): 152-158.

[49] Li, Yunlong, et al. "Electrochemical quartz crystal microbalance study on growth and property of the polymer deposit at gold electrodes during oxidation of dopamine in aqueous solutions." *Thin Solid Films* 497.1 (2006): 270-278.

[50] Roberts, James G., et al. "Specific oxygen-containing functional groups on the carbon surface underlie an enhanced sensitivity to dopamine at electrochemically pretreated carbon fiber microelectrodes." *Langmuir* 26.11 (2010): 9116-9122.

[51] Keeley, Gareth P., et al. "Thin film pyrolytic carbon electrodes: A new class of carbon electrode for electroanalytical sensing applications." *Electrochemistry Communications* 12.8 (2010): 1034-1036.

[52] Zeng, Hongjun, et al. "Ultrananocrystalline diamond integration with pyrolytic carbon components of mechanical heart valves."*Diamond and related materials* 61 (2016): 97-101.

[53] Mosmann, Tim. "Rapid colorimetric assay for cellular growth and survival: application to proliferation and cytotoxicity assays." *Journal of immunological methods* 65.1-2 (1983): 55-63.

[54] Olynik, Brendan, and Mojgan Rastegar. "The genetic and epigenetic journey of embryonic stem cells into mature neural cells." *Frontiers in genetics* 3 (2012): 81.

[55] Rydel, Russell E., and Lloyd A. Greene. "Acidic and basic fibroblast growth factors promote stable neurite outgrowth and neuronal differentiation in cultures of PC12 cells." *The Journal of neuroscience* 7.11 (1987): 3639-3653.

[56] Greene, Lloyd A. "Nerve growth factor prevents the death and stimulates the neuronal differentiation of clonal PC12 pheochromocytoma cells in serum-free medium." *The Journal of cell biology* 78.3 (1978): 747-755.

[57] Storch, Alexander, et al. "Long-term proliferation and dopaminergic differentiation of human mesencephalic neural precursor cells." *Experimental neurology* 170.2 (2001): 317-325.

[58] Balasubramaniyan, V., et al. "Effects of histone deacetylation inhibition on neuronal differentiation of embryonic mouse neural stem cells." *Neuroscience*143.4 (2006): 939-951.

[59] Satoh, T., et al. "Induction of neuronal differentiation in PC12 cells by B-cell stimulatory factor 2/interleukin 6." *Molecular and cellular biology* 8.8 (1988): 3546-3549.

[60] Bourque, Marie-Josée, and Louis-Eric Trudeau. "GDNF enhances the synaptic efficacy of dopaminergic neurons in culture." *European Journal of Neuroscience* 12.9 (2000): 3172-3180.

[61] Rolletschek, Alexandra, et al. "Differentiation of embryonic stem cell-derived dopaminergic neurons is enhanced by survival-promoting factors." *Mechanisms of development* 105.1 (2001): 93-104.

[62] Béduer, Amélie, et al. "Engineering of adult human neural stem cells differentiation through surface micropatterning." *Biomaterials* 33.2 (2012): 504-514.

[63] Cai, Lei, et al. "Photocured biodegradable polymer substrates of varying stiffness and microgroove dimensions for promoting nerve cell guidance and differentiation." *Langmuir* 28.34 (2012): 12557-12568.

[64] McNamara, Laura E., et al. "Nanotopographical control of stem cell differentiation." *Journal of tissue engineering* 1.1 (2010): 120623.

[65] Jain, Shilpee, Ashutosh Sharma, and Bikramjit Basu. "Vertical electric field stimulated neural cell functionality on porous amorphous carbon electrodes."*Biomaterials* 34.37 (2013): 9252-9263.

[66] Uemura, Makoto, et al. "Matrigel supports survival and neuronal differentiation of grafted embryonic stem cell-derived neural precursor cells." *Journal of neuroscience research* 88.3 (2010): 542-551.

[67] Jan, Edward, and Nicholas A. Kotov. "Successful differentiation of mouse neural stem cells on layer-by-layer assembled single-walled carbon nanotube composite." *Nano Letters* 7.5 (2007): 1123-1128.

[68] Ryu, Seungmi, and Byung-Soo Kim. "Culture of neural cells and stem cells on graphene."*Tissue Engineering and Regenerative Medicine* 10.2 (2013): 39-46.

[69] Scelza, M. Z., et al. "A multiparametric assay to compare the cytotoxicity of endodontic sealers with primary human osteoblasts." *International Endodontic Journal* 45.1 (2012): 12-18.